NASA CONTRACTOR REPORT

NASA CR

NASA CR-760

ADDITIONAL STUDY AND FURTHER DEVELOPMENT OF THE TRACER-SPARK TECHNIQUE FOR FLOW-VELOCITY MEASUREMENTS

A Study of the Structure of Spark Columns for Velocity Measurement in a Hypersonic Stream

by James B. Kyser

Prepared by
DEPARTMENT OF AERONAUTICS AND ASTRONAUTICS
STANFORD UNIVERSITY
Stanford, Calif.
for

NATIONAL AERONAUTICS AND SPACE ADMINISTRATION • WASHINGTON, D. C. • MAY 1967

NASA CR-760

ADDITIONAL STUDY AND FURTHER DEVELOPMENT OF THE TRACER-SPARK TECHNIQUE FOR FLOW-VELOCITY MEASUREMENTS

A Study of the Structure of Spark Columns for Velocity Measurement in a Hypersonic Stream

By James B. Kyser

Prepared under Contract No. NsG-620 by
DEPARTMENT OF AERONAUTICS AND ASTRONAUTICS
STANFORD UNIVERSITY
Stanford, Calif.

for

NATIONAL AERONAUTICS AND SPACE ADMINISTRATION

For sale by the Clearinghouse for Federal Scientific and Technical Information
Springfield, Virginia 22151 – CFSTI price $3.00

ABSTRACT

In recent years, a number of methods of measuring flow velocity in a wind-tunnel stream have been developed. Many of these methods depend on the "tagging" of some part of the stream by a spark discharge. The present study of the structure of a spark column was undertaken to achieve a better understanding of the conditions under which these techniques can be used and the measuring accuracy that can be expected.

The experimental part of the study consisted of 1) time-resolved measurements of spark current, temperature, and intensity profile made in a static test chamber over a range of spark energies and ambient static pressures, with nitrogen as the test gas, and 2) measurements of flow velocity in a hypersonic stream made under controlled conditions. During both phases the effects of a magnetic field parallel to the spark axis were investigated.

The spark process was also studied analytically on the basis of published data from electron-drift experiments conducted in nitrogen. The measured time-resolved spark current is used as an input in the analysis, and it is shown that good agreement between measured and computed rates of change of temperature is obtained when the computed intensity profile is matched to the measured intensity profile. The analysis also shows that the spark heating will not necessarily limit the accuracy of measurement, but the rapid recombination of ions and electrons, characteristic of nitrogen plasmas, can impose a serious limit to the accuracy of any technique relying on the detection of the residual ionization in

a spark-heated column. As a consequence, a method of detecting the spark-heated column that does not depend on ionization might be a desirable part of a velocity-measuring system. Several such possibilities are discussed briefly, the measuring accuracy attainable with each is evaluated, and methods of improving accuracy are suggested.

ACKNOWLEDGMENTS

The author wishes to express his gratitude to his advisor, Professor Walter G. Vincenti, for his encouragement and many hours of valuable discussion during the course of this study. He also wishes to thank Dr. Charles E. Treanor of Cornell Aeronautical Laboratory for his suggestions for improving the manuscript, Messrs. W. T. Astleford and J. M. Kallis of Stanford University for their assistance with the computer programming, and Messrs. V. Matzkevitch and K. Willeke of Stanford University for their assistance during the experiments.

The work presented here was supported by the National Aeronautics and Space Administration under Grant NsG-620. Some of the results were obtained during a test program supported under Contract NaS-2-3303 by the National Aeronautics and Space Administration.

TABLE OF CONTENTS

LIST OF ILLUSTRATIONS

List of Illustrations (Continued)

LIST OF SYMBOLS

A	Angstrom units (10^{-8} cm)
B	a measure of the molecular rotational energy, cm^{-1}
c	velocity of light, cm/sec
D	distance from mid-plane to electrode tip, diffusion coefficient
E	energy per unit volume
E/p	electric field strength per unit pressure, v/cm/mm Hg
e	energy per molecule
h	Planck's constant
I	intensity, current
J	rotational quantum number, current density
k	Boltzmann's constant
l	mean free path, cm
M	molecular mass
m	electron mass
N_e	electron number density, cm^{-3}
N_m	molecule number density, cm^{-3}
N_u	number density of upper-excited-state molecules, cm^{-3}
n_c	electron-molecule collision rate, cm^{-3} sec^{-1}
n_i	ionizing collision rate, cm^{-3} sec^{-1}
n_r	recombination collision rate, cm^{-3} sec^{-1}
n_t	transition rate, cm^{-3} sec^{-1}
n_x	excitation collision rate, cm^{-3} sec^{-1}
Q	heat added or work done
q_e	electron charge
r	radius, cm
S	line strength
T	temperature, ^{o}K
t	time
v	velocity, cm/sec
$\bar{v}$	average velocity, cm/sec

W	electron drift velocity, cm/sec
X	cross section, 10^{-16} cm^2
α	volume recombination coefficient, cm^3/electron-sec
ϵ	mean electron energy, ev
η	mean energy transfer per collision
θ_V	characteristic temperature for vibration
λ	wavelength
λ_D	Debye length, cm
ν	wave number, cm^{-1}
ν'	frequency, cycles per second
τ_e	excited state lifetime
τ_m	time between molecular collisions
τ_R	rotational relaxation time
τ_s	spark duration

Subscripts

c	due to collisions
D	due to dissociative recombination collision
e	electron
J	refers to rotational quantum number
m	molecule
N	number of Angstrom units
o	band origin, initial value,
P,Q,R	refer to P, Q, R branches
R	rotational
r	due to relaxation
T	translational
V	vibrational
v	vibrational state

Superscripts

'	upper state
"	lower state
*	value corresponding to equilibrium

1. INTRODUCTION

The measurement of stream properties in a hypersonic wind tunnel is a difficult problem that has occupied numerous investigators for a period of years. Although the techniques for obtaining stagnation-point properties such as pressure and heat-transfer rate are well understood, there is a great deal of uncertainty concerning the measurement of stream properties in the undisturbed stream. Karamcheti et al. (1962) have shown the importance of an accurate knowledge of stream velocity by considering the effect on the evaluation of other quantities caused by an erroneous computation of velocity. They have also shown that the stream velocity cannot necessarily be obtained from measurements made in the tunnel reservoir and at the stagnation point of a probe in the test section.

Numerous methods have been used for measuring flow velocity in hypersonic tunnels. These include studying the convection of a spark-generated blast wave (Karamcheti et al., 1962), and more recently, measuring the convection of the spark-heated column itself in the following ways: Kyser (1964) struck a second spark through the column, relying on residual ionization in the column to provide a preferential path. Cunningham and Dicks (1964) used microwaves, with residual ionization in the column attenuating a microwave signal transmitted across the stream. Fuller (1965) used photomultipliers, the residual emission of radiation several microseconds after the spark was extinguished giving the detectable signal.

These three techniques depend on the spark-heated column being convected in exactly the same manner as the undisturbed stream and hence are subject to some question. Rudinger (1964) has pointed out that the spark-heated column follows the gas velocity precisely only if the velocity is constant, and that in an extreme case, the column velocity can exceed the gas velocity by as much as 60% if the gas is accelerated by a moving shock wave. Cunningham and Dicks (1964) noted that their technique gave invalid velocity measurements when an excessive amount of energy was used to generate the spark. Also, it is apparent that thermal expansion, electron diffusion,and electron-ion recombination can severely reduce the measuring accuracy obtainable with any technique that relies on the measurement of the location of the spark-heated column at some later time.

The present study of the structure of a spark-heated column of gas in a hypersonic stream was undertaken to help clear up these uncertainties and thus provide a basis for estimating the accuracy of velocity measurements that depend on the convection of a spark-heated column of gas. The behavior of the spark-heated column can be thought of as being governed by two separate processes: 1) the spark process and 2) the decaying-plasma process. The first of these lends itself to study by optical methods because of the high intensity of radiation emitted; the second does not. Other methods of measurement considered were judged to have poor time or space resolution and were not used in this study. The primary difference between the spark process and the decaying-plasma process is in the presence of an electric field in the former. The electric field is the mechanism that keeps electrons at their high energy

levels during the spark, while afterwards electron energy is controlled by the mechanics of the exchange of energy with the gas molecules. However, since the two processes are dominated by electron-molecule energy exchange and electron-ion recombination, a single set of equations can be used to study both processes and some confidence in the computed behavior of the decaying plasma can be realized if the computed behavior of the spark is similar to its observed behavior. In view of the factors discussed above, the spark process was studied experimentally and analytically, and the decaying-plasma process was studied analytically, only.

The experimental study of the spark process consisted of the measurement of luminous-intensity profile and spark temperature. All measurements were made in a static-test chamber at conditions similar to those encountered during operation of the Stanford spark-heated hypersonic tunnel. The analysis primarily consisted of the computation of electron mean energy and density, and was based on the assumption that the spark duration was so short that the gas in the spark column was not appreciably affected by the spark. This permitted published data from electron-drift experiments to be used to describe the electron behavior. When the radial variation of computed electric field strength was adjusted to obtain agreement between measured luminous-intensity profiles and those calculated on the basis of the computed electron mean energy and density, good agreement was obtained between measured and computed rates of change of temperature.

The decaying-plasma process in the spark-heated column was studied analytically with the use of the equations developed for the study of the spark process. The results were used to estimate the accuracy with which velocity could be measured if the spark-heated column were detected

by one of several different detection techniques. It is shown that spark heating and ion diffusion will not necessarily limit measuring accuracy, but that electron-ion recombination can be a serious limit to the accuracy of any measurement relying on residual ionization in the spark-heated column. At the density levels considered in this study, it is possible to improve measuring accuracy by using a magnetic field to confine the spark or by adjusting the electrode gap.

Finally, examples of experiments in a hypersonic stream are presented. In these experiments a spark-heated column was detected by 1) residual luminous-intensity measurements and 2) photography of a second spark struck through the column. Measuring accuracy inferred from each example is consistent with the estimated values.

2. EXPERIMENTAL PROGRAM

The experimental study of the spark process was conducted in a static-test chamber rather than in the hypersonic stream of the wind tunnel because of the large number of measurements required and the difficulty of controlling and repeating stream conditions in successive tests. A large number of the static measurements were made with a spark strength of 0.5 joules and a pressure of 1.0 mm Hg, since these conditions most closely duplicated wind-tunnel test conditions in the Stanford spark-heated hypersonic tunnel. It was not practical to match stream temperature (50°K), so all static testing was done at room temperature (295°K).

The static-test chamber is shown in Figure 1. It was attached to the vacuum tank of the spark-heated hypersonic tunnel so that the vacuum system and pressure gauges could be used in the static tests. The large pumping capacity of the tunnel vacuum system made it possible to flush the test chamber continuously with bottled nitrogen to keep the test gas pure. A sectional view of the static-test chamber is shown in Figure 2. The lens was normally focused on the electrode axis at the mid-plane, but could be adjusted to focus on a specified point on the mid-plane off of the axis.

In earlier studies of the utility of using sparks for flow-velocity measurement, it was found that a magnetic field oriented parallel to the spark axis could cause a significant reduction in the diameter of the

spark. Therefore, two coils were attached to the static-chamber wall as shown in Figures 1 and 2 so that the effect of a magnetic field on the spark process could be studied. The coils were accurately aligned, with their common axis containing the electrode axis. Power was obtained from a bank of twelve 12-volt aircraft batteries connected in series.

The circuit used to generate sparks for the static tests is the same as that used in previous work (Kyser, (1964)) and is shown in Figure 3. Spark energy was varied by changing the size of the storage capacitor. When the smallest capacitor was used, the capacitance of the transmission cable was found to alter the discharge characteristics because of its contribution to the inductance-capacitance product of the circuit. To alleviate this, the transmission cable was made as short as possible by placing the spark-generating circuit adjacent to the static-test chamber. The location of the circuit is shown in Figure 1(a), where the covered chassis on which the circuit is mounted is located immediately to the right of the static-test chamber.

In order that results would be as general as possible, static tests were conducted over a wide range of conditions. Spark strength was varied from 0.05 to 5.0 joules, magnetic field strength from 0 to 655 gauss, and pressure from 0.1 to 10 mm Hg. Spark voltage and electrode gap were held constant respectively at 10 KV and 12.7 cm (5 inches) for all tests. The measurements made in the static-test chamber can be divided into three categories: spark current, spark temperature and spark-intensity profile. Extensive quantitive current measurements were not made since it was found that the current followed the light output closely. Extensive measurements of spark temperature and intensity

profile were made, particularly in the case of the 0.5-joule spark at 1.0 mm pressure. Spark temperature was measured by examining the rotational structure of a selected band in the spark spectrum. Intensity profile was measured photographically or by scanning the spark with a focused optical system and photomultiplier tube. Details of the techniques are given in the following chapters.

3. MEASUREMENT OF SPARK TEMPERATURE

As the starting point in the experimental study of the structure of the spark column, the spark temperature was measured. These measurements were made to assist in the understanding of the basic spark processes and to give the initial temperature of the decaying plasma in the spark-heated column, permitting the thermal expansion of the column to be studied. Because of the sub-microsecond spark duration encountered in the work, it was necessary to resort to spectrographic measuring techniques incorporating photomultiplier tubes to obtain the required speed of response. All measurements were made at the mid-plane of the spark in the static-test chamber shown in Figures 1 and 2.

Nitrogen was selected as the test gas because it is used in the Stanford spark-heated tunnel to avoid oxidation of the tunnel components and consequent contamination of the flow. Typical spectrographic plates of the nitrogen-spark spectrum are shown in Figure 4. The plate in Figure 4(a) shows the spectrum of the spark without a magnetic field; Figure 4(b) shows the spectrum of the spark with a 655-gauss magnetic field applied parallel to the spark axis. The upper, middle, and lower spectra in Figure 4(a) correspond to 125, 25, and 5 sparks. In Figure 4(b) these correspond to 25, 5, and 1 spark. From the plates it can be seen that the most prominent feature of the spectrum is a series of regularly spaced bands, called the second-positive band system. The band system

results from a single electronic transition, called the $C^3\pi \rightarrow B^3\pi$ transition in the terminology of spectroscopy. The B and C have no physical significance, but the superscript 3 indicates that the molecular states are triplet states; the π indicates that the quantum number of the electronic orbital angular momentum (Λ) along the inter-nuclear axis has a value of one.

Another band system, called the first-positive system, is known to exist in the spark spectrum. It is not found in the plates in Figure 30, because it is of low intensity and the film used was insufficiently sensitive in the infrared where the band system occurs.

Each band within the second-positive system results from a particular vibrational transition taking place simultaneously with the electronic transition, and close examination of each band would show that it is composed of a large number of lines rather than a continuum. Each line represents a particular rotational transition taking place simultaneously with the electronic and vibrational transitions. These lines can be grouped into branches called the R, Q, and P branches, corresponding to a change in rotational quantum number of -1, 0, and +1, respectively. Other values for the change in rotational quantum number are forbidden. Since the intensity of each line is primarily a function of the number of molecules undergoing the corresponding transition, the rotational temperature can be found from the measured intensity distribution within a specified band if it is assumed that the molecules have a Boltzmann distribution of rotational energy.

3.1. Computed Band-Intensity Distribution

Before temperature can be obtained from the measured band-intensity distribution, it is necessary to compute the intensity distribution from molecular constants for a range of rotational temperatures, and this will be done in this section. The derivation of the equations governing emission of radiation by a molecular transition is well covered by Herzberg (1950) or in references cited by him, so it will not be repeated here.

The frequency and wavelength of radiation from an electronic transition undergone by a single molecule are related to the energy difference between the two states in the transition through Bohr's frequency condition

$$E = h\nu' = \frac{hc}{\lambda}$$

where E is the energy of the emitted radiation, equal to the energy difference between the upper and lower states,

h is Planck's constant,

ν' is the frequency of the radiation,

c is the velocity of light, and

λ is the wavelength of the radiation.

As a result of the size of the numbers involved, it is more convenient to work with wave number rather than frequency, where wave number is defined as

$$\nu = \frac{\nu'}{c} = \frac{1}{\lambda} .$$

Equations for the wave number of the lines in the three branches are given by Herzberg as equations (IV-32) through (IV-34) and are as follows:

$$\text{R branch:} \quad \nu = \nu_o + 2B'_v + (3B'_v - B''_v)J + (B'_v - B''_v)\, J^2$$

$$\text{Q branch:} \quad \nu = \nu_o + (B'_v - B''_v)J + (B'_v - B''_v)\, J^2$$

$$\text{P branch:} \quad \nu = \nu_o - (B'_v - B''_v)J + (B'_v - B''_v)\, J^2$$

where ν_o is the wave number of the band origin,

B_v is a measure of the molecular energy and is proportional to the reciprocal of the moment of inertia of the molecule in the vibrational state v (B'_v, upper state of the transition; B''_v, lower state of the transition), and

J is the rotational quantum number of the lower state of the transition.

The three equations will be more useful for emission measurements if rewritten in terms of the upper-state rotational quantum number. This can be accomplished by the following substitutions:

R branch: $J = J' - 1$

Q branch: $J = J'$

P branch: $J = J' + 1$.

After some algebraic manipulation, the final result is

$$\text{R branch:} \quad \nu = \nu_o + 2B_v' (J'+1) + (B_v' - B_v'') J' (J'+1) \qquad (1a)$$

$$\text{Q branch:} \quad \nu = \nu_o + (B_v' - B_v'') J' + (B_v' - B_v'') J'^2 \qquad (1b)$$

$$\text{P branch:} \quad \nu = \nu_o - (B_v' + B_v'') (J'+1) + (B_v' - B_v'') (J'+1)^2 . \qquad (1c)$$

The terms B_v' and B_v'' are evaluated with the aid of equation (III-114) of Herzberg:

$$B_v = B_e - \alpha_e(v + 1/2)$$

where B_e is the value of B_v when the molecule is at equilibrium nuclear separation, and

$\alpha_e(v + 1/2)$ is the correction for increase in average nuclear separation resulting from anharmonic vibration.

It is now necessary to select a particular band and thus fix the vibrational quantum numbers of the upper and lower states in the transition. Referring back to Figure 4, we see that the strongest bands have band heads at about 3370A, 3580A, and 3800A. In the work of Nicholls (1964) these are seen to correspond to the (0, 0) ($v' = 0$, $v'' = 0$) band

at 3371.3A, the (0,1) band at 3576.9A, and the (0,2) band at 3804.9A. The (0,2) band was selected for the temperature measurements because of the better sensitivity of available photomultiplier tubes to the longer-wavelength radiation. For the (0,2) band, the above equation gives

$$B'_v = B'_e - (1/2)\,\alpha'_e$$

$$B''_v = B''_e - (5/2)\,\alpha''_e \,.$$

From Table 39 of Herzberg, we obtain

$$B'_v = 1.8259 - (1/2)(0.0197) = 1.8161, \text{ cm}^{-1} \qquad [C^3\pi \text{ state}]$$

$$B''_v = 1.6380 - (5/2)(0.0184) = 1.5920, \text{ cm}^{-1} \,. \qquad [B^3\pi \text{ state}]$$

With these values, equations (1) can be rewritten in terms of wave number as

$$\text{R branch:} \quad \nu = \nu_o + 3.6518\,(J'+1) + 0.2241\,J'\,(J'+1), \text{cm}^{-1} \qquad (2a)$$

$$\text{Q branch:} \quad \nu = \nu_o + 0.2241\,J'\,(J'+1), \text{ cm}^{-1} \qquad (2b)$$

$$\text{P branch:} \quad \nu = \nu_o - 3.4081\,(J'+1) + 0.2241\,(J'+1)^2, \text{cm}^{-1}. \qquad (2c)$$

At this point it should be noted that ν_o is not the wave number corresponding to the band head at 3804.9A, which has a value of 26,282 cm^{-1}, but is the wave number of the band origin, i.e., the wave number of the

$J' = 0$, $J = 0$ transition. The band head is formed by the P branch doubling back on itself. The difference in wave number between the band origin and the band head can be found by differentiating equation (2c) and solving for the value of J' that makes the derivative equal to zero. Thus we obtain

$$\frac{d\nu}{dJ'} = -3.4081 + .4482\ (J'+1) = 0$$

from which we have $J' = 6$ or 7 since only integral numbers are permitted. Therefore, we obtain

$$\nu_{\text{band head}} = \nu_o - (3.4081)\ (7) + (.2241)\ (7)^2, \quad \text{cm}^{-1},$$

or

$$\nu_o = 26{,}295 \ \text{cm}^{-1}\ .$$

If this substitution is made, equations (2) can be written as

$$\text{R branch:} \quad \nu = 26{,}295 + 3.6518\ (J'+1) + 0.2241\ J'\ (J'+1), \ \text{cm}^{-1} \tag{3a}$$

$$\text{Q branch:} \quad \nu = 26{,}295 + 0.2241\ J'\ (J'+1), \quad \text{cm}^{-1} \tag{3b}$$

$$\text{P branch:} \quad \nu = 26{,}295 - 3.4081\ (J'+1) + 0.2241\ (J'+1)^2, \ \text{cm}^{-1} \tag{3c}$$

As wavelength may be measured more easily than wave number, equations (3) are more useful if put in terms of the wavelength λ by taking the reciprocal of each side. This is readily done with the help of the

binomial theorem, as shown in the following for the R-branch equation:

$$\lambda = \frac{1}{\nu} = \frac{1}{26{,}295} \left\{1 + \left[\frac{3.6518}{26{,}295}\,(J'+1) + \frac{0.2241}{26{,}295}\,(J')(J'+1)\right]\right\}^{-1}$$

$$= \frac{1}{26{,}295}\left\{1 - \left[\frac{3.6518}{26{,}295}\,(J'+1) + \frac{0.2241}{26{,}295}\,(J')(J'+1)\right] + \cdots\right\}$$

$$= \left[3803.0 - 0.528\,(J'+1) - 0.0324\,(J')(J'+1)\right] \times 10^{-8}, \quad cm$$

or

$$\lambda_N = 3803.0 - 0.528\,(J'_{RN}+1) - 0.0324\,J'_{RN}\,(J'_{RN}+1), \quad A. \qquad (4a)$$

Similarly for the Q branch we have

$$\lambda_N = 3803.0 - 0.0324\,J'_{QN}\,(J'_{QN}+1), \qquad A, \qquad (4b)$$

and for the P branch

$$\lambda_N = 3803.0 + 0.493\,(J'_{PN}+1) - 0.0324\,(J'_{PN}+1)^2, \quad A, \qquad (4c)$$

where J'_{RN}, J'_{QN}, and J'_{PN} are the upper-state rotational quantum numbers corresponding to emitted radiation of wavelength λ_N.

At this point the line spacing within the band can be examined. It is readily seen that each branch has lines spaced as close as one-half an Angstrom unit at low rotational quantum numbers, and the P branch has a line spacing of one Angstrom unit at a rotational quantum number of 30.

In reality the line spacing is much closer than indicated by equations (4). This results from triplet splitting which is due to interaction of the electron spin vector with the electron orbital-momentum vector. As a result, each line is split into three lines with an average wavelength given by equations (4). Owing to the close line spacing, the task of isolating, identifying, and measuring the intensity of a single line appears formidable. Therefore, for these studies the line structure of the band is assumed to be a continuum. The intensity of the continuum at a particular wavelength is determined by the following factors: 1) the number of lines per unit wavelength in each branch at the given wavelength, 2) the line strengths in each band at the given wavelength, 3) the number of molecules with rotational quantum numbers corresponding to transitions that give rise to lines at the given wavelength. It can be reasoned on physical grounds that each branch will contribute to the intensity of the continuum an amount proportional to the product of the three factors enumerated above. This implies that the energy of the radiation emitted by each molecule undergoing the specified electronic-vibrational-rotational transition is the same regardless of the rotational levels involved. It also implies that the probability that the upper-state molecule undergoes a transition is not a function of rotational quantum number. Strictly speaking, neither is correct since both radiant energy and transition probability are functions of the wavelength of emitted radiation. Since the bands under consideration are narrow, however, a good approximation can be obtained with these two assumptions. The calculation of these three factors and the resulting continuum intensity distribution will be covered in the following paragraphs.

The number of lines per unit wavelength, or line spacing, in each branch is found by the following procedure:

1) For a given wavelength λ_N, solve equations (4) for J'_{RN}, J'_{QN}, J'_{PN}. Because of the assumed continuum distribution, non-integral values of J' can be allowed.

2) Calculate λ_R, λ_Q, and λ_P for $J'_R = J'_{RN} + 1$, $J'_Q = J'_{QN} + 1$, and $J'_P = J'_{PN} + 1$.

3) Obtain the line spacing for the three branches from

$$\Delta\lambda_{RN} = \lambda_N - \lambda_R \tag{5a}$$

$$\Delta\lambda_{QN} = \lambda_N - \lambda_Q \tag{5b}$$

$$\Delta\lambda_{PN} = \lambda_N - \lambda_P \,. \tag{5c}$$

This procedure will not be valid in the space between the band origin and the band head because there the P branch has two values of J'_{PN} corresponding to each λ_N. Since this space represents a range of less than 2 Angstrom units in width, the restriction is of little consequence.

Both upper and lower states in the transition are π states ($\Delta\Lambda = 0$), so the line strengths are given by equations (IV-81) of Herzberg. These are

$$\text{R branch:} \quad S_{JR} = \frac{(J'+1)\,(J'-1)}{J'} \tag{6a}$$

$$\text{Q branch:} \quad S_{JQ} = \frac{(2J'+1)}{J'(J'+1)} \tag{6b}$$

$$\text{P branch:} \quad S_{JP} = \frac{(J'+2)\ J'}{J'+1} \tag{6c}$$

If the three line strengths for a given J' are added, the sum will be the level's statistical weight $(2J'+1)$. If a molecule undergoes a transition, the probability that the transition will be an R-branch transition, a Q-branch transition, or a P-branch transition is $S_{JR}/(2J'+1)$, $S_{JQ}/(2J'+1)$, or $S_{JP}/(2J'+1)$, respectively.

The number of molecules with a given rotational quantum number is found with the aid of equation (III-167) of Herzberg:

$$N_J = N \frac{hcB}{kT} (2J+1) \exp\left[- \frac{BJ(J+1)\ hc}{kT} \right] \tag{7}$$

where N is the total number of molecules,

B is B_v used earlier to evaluate line position,

k is Boltzmann's constant, and

T is the absolute temperature.

For a given sample of gas at a specified temperature, equation (7) can be rewritten as

$$N_J = K_1 (2J'+1) \exp\left[- \frac{B_v' J'(J'+1)\ hc}{kT} \right]$$

$$= K_1 (2J'+1) \exp\left[- \frac{2.607\ J'\ (J'+1)}{T} \right]$$

where the constant K_1 is the same for all rotational quantum numbers and the prime notation refers to the upper state, as noted earlier.

Combining these factors, we can write the continuum intensity at any wavelength λ as

$$I_N = I_{RN} + I_{QN} + I_{PN} \tag{8}$$

where

$$I_{RN} = K_2 \frac{S_{RN}}{\Delta\lambda_{RN}} \exp\left[- \frac{2.607\ J'_{RN}\ (J'_{RN}+1)}{T} \right]$$

$$I_{QN} = K_2 \frac{S_{QN}}{\Delta\lambda_{QN}} \exp\left[- \frac{2.607\ J'_{QN}\ (J'_{QN}+1)}{T} \right]$$

$$I_{PN} = K_2 \frac{S_{PN}}{\Delta\lambda_{PN}} \exp\left[- \frac{2.607\ J'_{PN}\ (J'_{PN}+1)}{T} \right]$$

and

K_2 is a constant for a given sample of gas at specified temperature, and is a function of band intensity corresponding to a line spacing of unity,

S_{RN}, S_{QN} and S_{PN} are given by equations (6a), (6b) and (6c),

$\Delta\lambda_{RN}$, $\Delta\lambda_{QN}$ and $\Delta\lambda_{PN}$ are given by equations (5a), (5b) and (5c),

J_{RN}, J_{QN} and J_{PN} are the solutions to equations (4a), (4b) and (4c) for a specified wavelength λ_N, and

T is the specified rotational temperature.

On the basis of equation (8), values of I_N were calculated for values of λ_N from 3802 to 3755 Angstrom units, the head of the next band. These values, normalized with respect to the intensity of 3795 Angstrom units, are shown in Figure 5 for selected rotational temperatures between 200°K and 2000°K. The reasons for adopting this normalization procedure will be discussed in the following section.

3.2. Experimental Method

The spark spectrum was analyzed with a Hilger medium-quartz spectrograph with a focal length of 0.6 meters and a Jarrell Ash half-meter grating spectrometer. The two instruments complemented each other in the following manner: the spectrograph permitted intensity-versus-wavelength data to be obtained over a given time interval; the spectrometer permitted intensity-versus-time data to be obtained over a given wavelength interval. Because of the low light levels, it was necessary to have a time interval of at least the duration of the spark when the spectrograph was used to collect data. As discussed in the previous section, it was necessary to have a wavelength interval greater than the rotational line spacing when the spectrometer was used.

Spectrographic plates of a 0.5-joule spark at 1.0 mm pressure are shown in Figure 4. The upper three spectra correspond to sparks without a magnetic field. The lower three spectra correspond to sparks with a 655-gauss magnetic field. Data obtained in this manner permit the entire

spectrum to be examined. The experimental arrangement used to obtain spectrographic data is shown in Figure 6. The collimating lens was adjusted so that the spark image was formed on the spectrograph slit. Since this lens was glass it filter out virtually all radiation with wavelengths shorter than 3000 Angstrom units.

The apparatus used to obtain data with the spectrometer is also shown in Figure 6. The spectrometer was removed as far as possible from the spark to reduce the effects on the data of radio-frequency radiation from the spark. Collimating and condensing lenses were used to achieve a maximum light-gathering efficiency, and the geometry of the optical path provided a good selectivity of light from the spark. The optical components were adjusted with the aid of a neon bulb inserted in place of the spark column by focusing the image of the center of the bulb on the spectrometer entrance slit.

A Dumont 6292 photomultiplier tube was used to measure the light intensity at the exit slit of the spectrometer. A diagram of the circuit used with the tube is shown in Figure 7. To minimize noise pickup, all leads were kept as short as possible, the entire circuit was encased in a brass tube, and a mu-metal shield was placed around the photomultiplier tube. The output resistance was kept small (1000 Ohms) to insure a satisfactory response time.

Data were recorded on a Tektronix type-551 oscilloscope in conjunction with a type-53/54B preamplifier. The preamplifier had an input capacitance of 47 pf, and the coaxial data cable had a distributed capacitance of about 34 pf. Therefore, the resistance-capacitance product of

the photomultiplier output circuit was 0.08 microseconds, which is approximately the magnitude of the molecular upper-state lifetime.

The linear range of the photomultiplier circuit was evaluated by inserting calibrated neutral-density filters in the optical path and observing the effect on the output. With this procedure, it was found necessary to limit photomultiplier output to 60 millivolts, or an anode current of 60 microamps, to achieve linear response.

The spark was oriented along a horizontal line so that it was at right angles to the spectrometer entrance slit. Preliminary experiments showed that if the spark was oriented parallel to the slit, large random variations in intensity would occur, indicating a spatial instability of the spark. These variations were greatly reduced by orienting the spark at right angles to the slit and opening the entrance and exit slits to their maximum height and width.

The use of large slit widths made it necessary to modify the computed intensity distributions of Figure 5 to account for the instrument-profile effects, that is, to account for the fact that the photomultiplier tube was measuring the intensity of radiation over a wide range of wavelengths rather than at a single wavelength. Instrument profile was measured by setting the spectrometer entrance and exit slit width and height to the values used in the experiments and scanning the 6328-Angstrom line from a helium-neon laser. The results, plotted as relative intensity versus wavelength, are shown in Figure 8. The instrument response is triangular because the widths of the entrance and exit slits are equal. Since the laser line has virtually zero line width, no correction for line profile was required. The instrument profile shown in Figure 8 was applied at a wavelength of 3805 Angstrom units without

correction for the change in wavelength, since the change in dispersion with wavelength is relatively small.

The band-intensity distribution data were corrected for instrument-profile effects by assuming that the relative instrument response was as shown by the solid line in Figure 8, which is as follows:

100% at $\lambda = \lambda_{set}$,

74% at $\lambda = \lambda_{set} \pm 2$ Angstrom units,

39% at $\lambda = \lambda_{set} \pm 4$ Angstrom units,

0% at $\lambda = \lambda_{set} \pm 6$ Angstrom units.

Intensity distributions corrected in this manner are shown in Figure 9 for temperatures between 200°K and 2000°K. As it can be seen from a comparison of Figure 5 and Figure 9, the correction makes very little difference in the intensity distribution.

A preliminary survey of the intensity distribution across the entire band was made for a 1.0-joule spark at 1.0 mm pressure. These data, which will be discussed in more detail later, are plotted in Figure 9 and show that the measured intensity distribution for a wide range of wavelengths lies close to the 400°K line. This implies that the gas in the spark has a Boltzmann distribution of rotational kinetic energy and therefore the rotational temperature can be found by measuring the band intensity at any two wavelengths. For the case under discussion, 3795 Angstrom units appears to be convenient value for one of these wavelengths because the computed intensities can not be considered reliable

at wavelengths much closer to the band origin. With this in mind, the corrected band intensitites at 3775 Angstrom units and 3785 Angstrom units have been divided by the corrected intensity at 3795 Angstrom units and plotted versus temperature in Figure 10. For the present study, the 3785-Angstrom unit curve is the more desirable because of its steeper slope in the temperature range from 300°K to 400°K.

Spark temperatures were obtained by recording the time-resolved band intensities at 3795 and 3785 Angstrom units. Figure 10 was then used to convert the ratio of intensitites to temperature. The band intensities at the two different wavelengths could not be measured simultaneously, so it was necessary to utilize a different spark for each measurement. A continuum radiation, presumed due to transitions involving free electrons, was found to exist in the spark spectrum. The intensity of the continuum did not vary with wavelength, so it was measured by setting the spectrometer at 3815 Angstrom units, which is 10 Angstrom units beyond the band head. As a result, each spark-temperature measurement required three sparks, one with the spectrometer set at 3815 Angstrom units, one at 3795 Angstrom units, and one at 3785 Angstrom units. A second photomultiplier tube with a circuit similar to that of Figure 7 was used to ascertain that the spark luminosity was the same for each spark.

The data shown in Figure 9 were obtained in a slightly different manner; the peak continuum intensity was subtracted from the peak intensity at each wavelength. The resulting intensity distribution, therefore, corresponds roughly to the midpoint of the spark duration, 0.35 to 0.45 microseconds. As can be seen in Figure 11, the indicated

temperature of 400°K is in rough agreement with the 0.5 joule-spark temperature measurements taken during this period.

3.3. Experimental Results

On the basis of the procedures just described, the spark temperature was measured for the following conditions:

spark energy: 0.05, 0.5, 5.0 joules

magnetic field: 0, 225, 445, 655 gauss

pressure: 0.1, 0.33, 1.0 , 3.0, 10 mm Hg.

All tests were conducted in the static test chamber, and the chamber was flushed with nitrogen between sparks to insure that the test gas did not become contaminated. Typical oscillograms obtained with each of the spark energies are shown in Figure 11. The upper set of three traces in each case is the spectrometer output; the lower trace is the superimposed monitor output from each of the three sparks. The data traces correspond, from top to bottom, to 3815, 3795 and 3785 Angstrom units. The horizontal and vertical scales are noted in the figure. The slight ripple in the data traces is due to radio-frequency radiation from the spark.

Time-resolved temperatures at the spark centerline, obtained from oscillograms similar to those of Figure 11, are shown in Figure 12 for a number of sets of 0.5-joule sparks at 1.0 mm pressure without a magnetic

field and with a 655 gauss field. In each case the static temperature is initially somewhat higher than the ambient temperature of 295°K. Some increase in temperature during the course of the spark can be noticed since the final temperatures are generally higher than the initial values. The rates of increase are not measurable in this form, however, because of the scatter introduced by the noise discussed earlier.

The lines in Figure 12 were obtained by curve-fitting, by the least squares technique, an equation of the form

$$T = T_o + \frac{dT}{dt} t \ , \qquad (9)$$

where T is the temperature in degrees Kelvin, and

t is the time in microseconds from the initiation of the sparks,

to each set of data. The resulting equations are

$$T = 354 + 18.4\ t, \qquad °K$$

for the spark without a magnetic field, and

$$T = 340.5 + 93\ t, \qquad °K$$

for the spark with a 655-gauss field. The mean-squared deviations for the two cases are 23°K and 29°K.

As will be discussed in Chapter 7, the actual heating process did not have a constant increase of temperature with time, but in view of the data scatter a more elaborate temperature-time relationship is not justified. Nevertheless, the two fitted curves are more consistent with each other in the time range between 0.15 microseconds and 0.65 microseconds than indicated by the mean-squared deviations. At 0.15 microseconds the temperatures differ by only 3 degrees, which is well within the accuracy of measurement, and the temperature-time slope for the spark with a 655-gauss magnetic field is five times as great as the slope for the spark without a magnetic field. This ratio is close to the inverse of the ratio of spark cross-sectional areas, implying that the rate at which energy is added to the gas by the spark is not affected by the magnetic field. From this discussion it appears that the temperature-time relationships established by curve fitting are sufficiently precise to be of use in further analysis of the spark process. The result of using a large number of data points has been to cancel most of the effects of the noise-induced scatter.

An alternative method of eliminating noise effects is to integrate the data signal over a number of noise cycles. This approach, which yields average values, was used to show the effects of pressure, magnetic-field strength, and spark energy on spark temperature. Average temperatures were obtained by finding the area between the 3785-Angstrom and 3815-Angstrom traces and the area between the 3795-Angstrom and 3815-Angstrom traces. The ratio of these two areas was then converted to temperature by means of Figure 10. The average spark temperatures obtained by this method are shown in Figure 13 for the three spark

energies studied. Each datum point represents a separate measurement. The data are best interpreted physically as the temperature of the spark at its midpoint or point of maximum intensity. The validity of this interpretation can be seen from a comparison of the curve-fit temperatures at 0.4 microseconds in Figure 12 with the average temperatures in Figure 13 for the corresponding conditions. For the 0.5-joule spark at 1.0 mm pressure without a magnetic field these values are 361°K in Figure 12 and 366°K in Figure 13; for the 0.5-joule spark at 1.0 mm pressure with a 655-gauss magnitude field the values are 378°K and 385°K. Standard deviations computed on the basis of the average temperature measurements shown in Figure 13 for the two cases are 10°K and 4°K, respectively. Because of the greater number of measurements involved, the 10°K value is more representative of the measuring accuracy attained during the experiments.

For each spark energy the data show a clear trend of increasing average temperature with increasing pressure. The average temperature is seen to increase with increasing magnetic field strength for the 0.5- and 5.0-joule sparks but not for the 0.05-joule sparks. Also, the average temperature increases as spark energy is increased from 0.5 to 5.0 joules, but decreases when the spark energy is increased from 0.05 to 0.5 joules. No physical reason for this anomolous behavior is known, so it is attributed to data scatter since the magnitudes involved are only slightly greater than the standard deviation discussed above.

4. MEASUREMENT OF SPARK-INTENSITY PROFILES

As a second step in the experimental study of the spark process, spark-intensity profiles were measured. These data were used to establish the electric-field shape, which was essential to the analysis of the spark process. If such an analysis is not available, however, further information about the spark process can be obtained by assuming that the integrated-intensity profile is identical to the current profile. The justification for this assumption is that the field strength varies relatively little across the spark, hence the electron temperature and mobility are almost uniform. As a consequence, both current and spark intensity are proportional to electron density and therefore proportional to each other.

Intensity profile was measured in two ways: 1) directly with a focused optical system and 2) indirectly by recording the image of the spark on film and reading the film density with a microphotometer. The direct measurement has the disadvantage that a separate spark is required for each measurement at each value of radius. Time-resolved intensity profiles are obtained, however. The photographic method permits a complete intensity profile to be obtained from a single spark but does not give time-resolved data. It has the further disadvantage that data must be corrected for nonlinearity of the film response before intensity profiles can be obtained.

All measurements of intensity profile were made in the static chamber shown in Figure 1. Spark energy and magnetic field strength were varied as in the spark-temperature tests, but fewer pressure levels were used. Except for the data-recording instrumentation, the test procedure was the same as discussed in the previous chapter. The apparatus used for the direct measurement of spark-intensity profile is identical to that shown in Figure 6 except that the spectrometer was removed and the spark image was focused directly on the photomultiplier assembly. An optical filter was inserted in the optical path to eliminate all radiation except the second-positive band system. An orifice plate with a 0.028-inch-diameter orifice was placed at the focal point of the condensing lens to increase the resolution of the system. Since the image was enlarged three times by the two lenses, the effective field of view was about 0.010 inches in diameter.

Time-resolved intensity profiles of the 0.5-joule spark at 1.0 mm pressure without a magnetic field and with a 655-gauss field are shown in Figure 14. The large amount of scatter is probably due to a variation in centerline location between successive sparks rather than to an intensity variation, since total spark luminosity was monitored and found to be relatively constant. The data in Figure 14 show that the spark with a zero-gauss magnetic field is diffuse during its early stage and tends to become more confined as time progresses. The spark with a 655-gauss magnetic field does not exhibit this behavior, indicating that the externally applied magnetic field is an important confining influence in the early phase of the spark.

Intensities integrated over the total spark duration are shown in Figure 15. These curves would be equivalent to those obtained from photographic data corrected for film nonlinearity, if such a correction were applied. The data shown in Figures 14 and 15 will be used to establish the electric-field shape from which the radial variation of electron energy and density can be computed.

Photographs of the spark were made with either a Fairchild type-F-296 oscilloscope camera attached to the spark chamber or a 4 × 5 inch Graflex camera mounted on a tripod. Polaroid type-46-L film was used in the oscilloscope camera; Eastman Commercial film and Tri-X film were used in the Graflex camera. The type-46-L film was found to be the most satisfactory, in spite of a nonuniformity in background opacity, because of its lower exposure threshold and consequent better overall linearity. The results of the photographic measurements are presented in Figure 16 in terms of mean spark radius (found as described below). All radii were normalized with respect to the radius of the 0.5-joule spark at 1.0 mm pressure and without a magnetic field. With the data in this form, the effects of changes in magnetic field strength, spark energy, and static pressure can be seen easily.

The data-reduction procedure used to obtain Figure 16 was as follows: The film of each spark was read with the microphotometer, and the area under the intensity-distance record was obtained. The mean radius (defined as one-half this area divided by the peak intensity) was then normalized by dividing by the mean radius of the 0.5-joule spark at 1.0 mm pressure and without a magnetic field. For this data-reduction procedure to be valid, the intensity-distance plots for all sparks must have similar shape and peak intensity.

A comparison of the microphotometer profiles of the intensities of the spark images shows that the first part of this requirement is met. Four of these profiles are reproduced in Figure 17, normalized so that each has a peak intensity of unity. An inspection reveals the intensity distribution to be a modified Gaussian Curve, similar in shape for all profiles. As the magnetic field is decreased the curves are stretched along the distance axis but otherwise remain unchanged except for some distortion in the region of very low intensity ratios. The second part of the requirement was met by holding the maximum exposure level constant, which was possible for all sparks except the 0.05-joule spark without a magnetic field. Thus, if the photographed intensity profiles were to be corrected, a given intensity ratio in each profile would be multiplied by the same correction factor. Although the profiles would be distorted by such a correction, the curves would remain similar in shape since they were originally similar. The normalized radii, then, would be unaffected by these corrections.

Because of the scatter and lack of repeatability apparent in Figure 16, further analysis of the data, such as correction of the profiles for film nonlinearity, was not made. In the form of normalized radius, as in Figure 16, a clear trend of decreasing radius for increasing pressure is shown for all sparks without a magnetic field. No clear trend is exhibited for increasing spark energy, however.

5. ANALYSIS OF THE SPARK PROCESS

The effects of electron-ion recombination and ion diffusion on the behavior of a spark-heated column of gas can not, at this point, be evaluated from the measurements discussed in the previous chapters. Both are dependent on electron density and (to a smaller degree) on electron energy, so these quantities must be obtained before recombination and diffusion effects can be studied. The large expected variation of electron density with both radius and time appears to preclude measurement by microwave or Langmuir-probe techniques. Consequently, the approach adopted was to compute electron density and mean energy. The intensity measurements were used to obtain electric-field shape, and the measured temperatures were compared with computed values to provide a check of the validity of the calculations.

5.1. Electron-Behavior Measurements

The spark process cannot be described in detail unless the behavior of electrons in an electric field in the presence of nitrogen molecules is known. This subject has been studied by a large number of investigators over the past fifty years. In all these studies, while measurements

were being made electric field strength was held steady and current density was kept sufficiently small to avoid any heating of the gas. Data obtained by some of these investigators, namely Townsend and Bailey (1921), Neilsen (1936), Crompton and Sutton (1952), and Anderson (1964), have been used in the present study of the spark process. Before "steady-state" electron-drift data can be used in a process such as a high-current spark with a sub-microsecond duration, it must be shown that the spark is a steady-state process as far as the electron energy is concerned and that the gas in the spark column is not seriously affected by the spark. If this can not be done, the task of computing the spark process will become extremely complex.

One test that can be used to show whether the spark can be considered steady-state is an examination of the number of collisions experienced by an average electron during the spark duration. An approximate value of 4,000 collisions is obtained by use of the values $\bar{v} = 10^8$ cm/sec for average velocity, $\ell_e = 0.02$ cm for mean free path, (corresponding to an electric field strength of about 30 v/cm/mm Hg and a static pressure of 1.0 mm Hg), and 0.8 microsecond for spark duration. If this number of collisions per electron occurs during the spark duration, then each electron will undergo 100 collisions in a time interval equal to $2\frac{1}{2}\%$ of the spark duration. Certainly, this would be sufficient for the electrons to equilibrate if the change in conditions during the time interval were not a large one. Only at the very beginning and end of the spark period is there an appreciable change during such a time interval.

A second consideration in the use of electron-drift data for analysis of the spark process is the temperature and ionization level of the

gas in the spark column. If the gas is significantly heated or ionized by the spark, the electron-molecule collision processes will differ from those in the electron-drift experiments, and such data will not be applicable. As can be seen in Figure 12, a rotational temperature rise of only 11°K was recorded during the 0.5-microsecond period that the temperature of the 0.5-joule spark without magnetic field was measured, neglecting for the present the initial jump from the ambient temperature of 295°K. For this particular case, it appears that the rotational and translational temperatures of the gas are not appreciably affected, as far as the electron-molecule collision processes are concerned. Similarly, a close examination of the spectrographic plates shown in Figure 4 reveals that virtually all of the radiation is due to the neutral molecule. Therefore, the ionization level can be expected to be small. Some question does exist regarding the change in vibrational temperature during the spark and whether it will affect the electron-molecule collision process, however. For the present, it will be assumed that the change in vibrational temperature does not affect the electron-molecule collision process. The validity of these assumptions will be seen from the results, once the heating and ionization processes have been studied in detail.

Measured values of electron mobility W, mean energy loss per collision η, mean electron energy ϵ, and mean free path ℓ_e as functions of electric field strength E/p are shown in Figure 18. The solid lines shown in Figure 18 are the values actually used in the present study. The electron mobility measurements of Townsend and Bailey (1921) do not agree with those of Neilsen (1936) and Anderson (1964). The Townsend-Bailey data have been disregarded, therefore, in favor of

more recent data where improved measuring techniques were available. Fractional energy transfer is deduced from electron-mobility measurements so the lack of reliability in the mobility measurements of Townsend and Bailey will therefore reappear in fractional energy transfer. The corrected Townsend-Bailey values have been obtained by recomputing this parameter with the electron mobility measured by Neilsen or Anderson. The mean-energy measurements of Townsend and Bailey agree well with those of Crompton and Sutton, but the mean-free-path measurements do not. As in the case of the fractional energy transfer, the Townsend-Bailey mean-free-path data have been corrected by use of more recent electron-mobility data. In all cases, in the region where the Townsend-Bailey data overlap other data, the latter are favored.

Ionization cross sections and excitation cross sections for the second-positive band system are shown in Figure 19. These data are as given by Massey and Burhop (1952) and Longstroth (1934), respectively, except that the excitation cross sections have been put in dimensional form by means of the assumption that the maximum value of the excitation cross section is equal to the maximum value of the ionization cross section. This assumption allows a rough estimate to be made of the total number of molecules excited, so that it can be seen if there is appreciable depopulation of the ground state through the excitation process. The physical basis for this assumption is that an ionizing collision and an exciting collision both involve the loss of an electron by the molecule, and therefore are similar. In an exciting collision the incoming electron is captured; in an ionizing collision it is not.

The final quantity needed in the analysis of the spark process is the volume recombination coefficient α, which is defined by the following relation:

$$\frac{dN_e}{dt} = - \alpha N_e^2, \tag{10}$$

where N_e is the electron density. The relationship has this form because, as shown by Bailecke and Dougal (1958), the two-body dissociative recombination collision is the most important of the many recombination processes that occur.

Measurements of α at various electron temperatures have been reported by a number of investigators. Bialecke and Dougal report values of 6.7×10^{-6} cm^3/electron-sec at 92°K and 8.5×10^{-7} cm^3/electron-sec at 300°K. Faire and Champion (1959) report a value of 4.0×10^{-7} cm^3/electron-sec at 400°K, and Sayers (1956) reports a value of 1.1×10^{-7} cm^3/electron-sec at 3200°K. A theoretical analysis by Bates (1950) shows that α should vary as $1/\sqrt{T_e}$. For purposes of the present work, the value of α used was that reported by Faire and Champion corrected for temperature according to Bates' analysis. This gives

$$\alpha = 8 \times 10^{-6}/\sqrt{T_e}$$

$$= 0.9 \times 10^{-7}/\sqrt{\epsilon}, \qquad \text{cm}^3\text{/electron-sec} \tag{11}$$

where T_e is the electron temperature is degrees Kelvin, and

ϵ is the average electron energy in electron volts.

This formula gives values slightly larger than reported by Sayers and slightly smaller than reported by Bailecke and Dougal. In a sense, therefore, it represents an average of the values discussed above.

5.2. Significance of Electron-Drift Measurements

Of the measurements of electron characteristics shown in Figure 18, the most difficult to explain is the behavior of the mean energy loss per collision η. According to simple kinetic theory, the average fractional energy transferred during a single elastic electron-molecule collision is

$$\eta = 2m/M$$

where m is the mass of the electron, and
M is the mass of the molecule.

For an elastic collision between an electron and a nitrogen molecule, this gives

$$\eta = 0.39 \times 10^{-4}, \tag{12}$$

which follows from the assumption of conservation of energy and momentum during the collision and takes into account only energy transferred to

translational kinetic energy. Measurements of energy transfer presented in Figure 18 show that the actual energy transfer is an order of magnitude higher than the value given by this relation, even at electron-excitation levels well below the vibrational threshold.

Gerjuoy and Stein (1955) attribute this discrepancy to rotational excitation and show theoretically that, as a consequence of rotational excitation, the actual energy loss will be an order of magnitude greater than given by equation (12). More recently, Sampson and Mjolsness (1965) have shown theoretically that energy transfer due to rotational excitation is close to the values shown in Figure 18 for low electron-excitation levels. From this discussion it appears that the fractional energy loss per collision shown in Figure 18 for low values of electric field strength must represent the fraction of the kinetic energy of an electron that is transferred to a molecule as rotational and translation excitation. If $\eta = 3.11 \times 10^{-4}$, the value corresponding to a field strength of 0.1 volt/cm/mm Hg, is assumed representative of all low-field-strength values, of η, and the kinetic-theory value of 0.39×10^{-4} from equation (12) is taken as the fractional energy transfer to translational excitation, the remainder of 2.72×10^{-4} will be the fractional energy transfer to rotational excitation.

At higher values of field strength, the fractional energy transfer is higher than predicted by Gerjuoy and Stein (1955) or Sampson and Mjolsness (1965) because of vibrational and electronic excitation. Haas (1957) and Shulz (1959) have shown the rapid increase in fractional energy transfer at electron energies near one electron volt (and electric field strength of one volt/cm/mm Hg) to be due to an electron-attachment

collision in which the negative ion N_2^- is formed. The ion has a short lifetime, and when the extra electron is rejected, a large part of the binding energy is transferred to vibrational excitation. Haas reports the collision cross section for this phenomenon to be sharply peaked at 2.3 electron volts, with a magnitude of about 15% of the elastic-scattering cross section. Outside the energy range from 1.5 to 5 electron volts it is virtually zero. Electronic excitation does not become significant until the average electron energy is increased to about 10 electron volts, so it does not have much effect on η except at the highest field strengths shown in Figure 18.

A significant amount of electron energy is transferred to vibrational excitation during the spark. Little of this energy will be converted to translational or rotational energy during the time of interest, however, because of the long relaxation time associated with vibration. Hurle (1964) shows that the electron temperature in an expanding nitrogen plasma will tend to equilibrate with the molecular vibrational temperature. The vibrational energy acquired during the spark process can be expected, therefore, to have some effect on the decaying plasma in the spark-heated column.

Much less energy is transferred to ionization or electronic excitation, but according to Bialecke and Dougal (1958) about one-third of the ionization energy is transferred to translational or rotational excitation through a dissociative recombination reaction. This energy must, therefore, be taken into account in any study of the heating process. The recombination of an electron and a molecular ion releases 15.58 electron volts of ionization energy; only 9.76 electron volts are

required to dissociate the molecule into two neutral atoms and the remaining 5.82 electron volts are converted into molecular translational and rotational kinetic energy as the result of collisions between the two atoms and the surrounding molecules. The energy transferred to electronic excitation is, for the most part, lost through radiation and has little effect on the molecular heating process.

5.3. Computation Procedure

The primary objective of the computation procedure is the calculation of electron density and mean energy so that effects of electron-ion recombination and ion diffusion in the spark-heated column can be evaluated. In this section these values will be calculated. To check the validity of the calculations, spark intensity and temperature will also be computed and will be compared with measured values. If necessary, modifications to the equations will be made to get agreement between measured and computed spark intensity and temperature. As a final step, the spark process will be described as completely as possible so that several methods of detecting the spark-heated column can be evaluated.

The computation procedure rests fundamentally on the assumption that the gas in the spark column is little affected by the spark, as far as the mechanics of electron-molecule collisions are concerned. This assumption is valid only when the spark duration is sufficiently short or the current is sufficiently low. Its validity in the cases under study will be examined in Chapter 7.

As discussed previously, the spark current is known as a function of time from intensity measurements or from a computation based on the spark-circuit characteristics and can be used as the primary input parameter. The spark current is equal to the radial integral of current density, which is controlled by the electric field strength (or equivalently, the electron energy) and the electron density. The electron density is equal to the integrated difference between the ionization-collision rate and the recombination-collision rate, each of which is controlled by the electron energy and the electron density.

This discussion suggests a method of solving for electron density and mean energy if the spark current is known. That is, the two relationships described can be used to find the two unknown quantities. Unfortunately, the radial variation of electric field strength, which is not known, will influence the results.

The intensity of the spark can be computed on the basis of an assumed radial variation of electric field strength by integrating the difference between the electronic excitation rate and de-excitation rate. The intensity profile can then be compared with measured values, if available, and the assumed radial variation of field strength adjusted to give the measured intensity profile. In this manner the correct radial variation of field strength can be found.

Once the above has been accomplished the energy balance between 1) the work done on the electrons by the electric field and 2) the rate at which energy is transferred to the surrounding molecules can be examined in detail. This will allow the energy transferred to each molecular degree of freedom to be computed.

Details of the computation procedure outlined above are given in the following paragraphs.

Electron Density and Mean Energy - Kyser (1964) considered the spark circuit to be a series resistive-inductive-capacitive network and computed the spark current on the basis of the circuit characterisitics, exclusive of the spark gap. Measurements of current made during the present study show this procedure to be valid. Spark current was shown to follow intensity very closely, and intensity can be seen in Figure 11 to have a damped-sinusodial shape as does the computed current-time curve given by Kyser. The relationship between spark current and intensity is discussed further in Chapter 8.

The spark can thus be thought of as accomodating the current specified by the other elements in the circuit. From this line of reasoning it can be surmised that a change in electric field strength within the spark is the mechanism that maintains the spark current at the values prescribed by the other circuit components. The relationship between current density and electric field strength is governed by the density of free electrons, as shown by the equation

$$J(t) = W[E(t)/p]\, N_e(t)\, q_e, \quad \text{amps/cm}^2, \tag{13}$$

where $J(t)$ is the spark-current density,

$W[E(t)/p]$ is the electron mobility (from Figure 18),

$N_e(t)$ is the free-electron number density, and

q_e is the electron charge (1.602×10^{-19} coulomb).

Both the electron mobility and the number of free electrons will vary across the spark cross section, so the equation for current will be an integral relationship, integrated across the cross section. If the spark is assumed to be axially symmetric, we have

$$I(t) = 2\pi q_e \int_0^\infty W[E(r,t)/p]\, N_e(r,t)\, r\,dr, \quad \text{amps}, \tag{14}$$

where $I(t)$ is the spark current, and

r is the distance from the spark centerline.

Equation (14) cannot be evaluated at a specific time t until $W[E(r,t)/p]$ and $N_e(r,t)$ are known. Since W is a function of electric field strength only, and electric field strength is a function of radius and time, the radial variation of W can be found at a specified time if an appropriate radial variation for electric field strength can be obtained. If the two electrode tips are assumed to be infinitesimal points of differing potential, the radial variation of the electric field strength at the mid-plane is given by classical electrostatics as

$$E(r,t)/p = E(0,t)/p \left[\frac{1}{1 + (\frac{r}{D})^2}\right]^{3/2}, \tag{15}$$

where $E(0,t)/p$ is the field strength at the centerline, and

D is the distance from the mid-plane to either electrode tip.

With the equation in this form, either the exponents $3/2$ or 2, or the value of D can be changed to account empirically for the fact that the

electrodes have a finite size and the field is not static, and for the effects of the applied magnetic field. A change in the exponent 3/2 was used because of ease of computation.

The value of $E(0,t)/p$ is related in turn to the number density of free electrons $N_e(r,t)$ and therefore cannot be found without further computation.

The electron number density is controlled by two factors: the number of ionizing collisions and the number of recombining collisions. The rate of ionizing collisions is a function of the mean electron energy and the ionization cross section given in Figure 19 and can be written as

$$n_i(r,t) = N_m \int_0^\infty (N_e)_E \, v_E \, X_E \, dE, \qquad cm^{-3} \, sec^{-1} \tag{16}$$

where $n_i(r,t)$ is the number of ionizing collisions per unit volume per unit time,

N_m is the molecular number density,

$(N_e)_E$ is the number of electrons per unit volume with energy between E and $E + dE$,

v_E is the electron velocity corresponding to energy E, and

X_E is the ionization cross section of electrons with energy E.

The dependence on radius and time of terms in the right-hand side of this and subsequent equations is not noted because of the number of terms involved. Where convenient, it will still be noted on the left-hand side, however.

If the electrons are assumed to have a Maxwellian velocity distribution, equation (16) can be rewritten as

$$n_i(r,t) = 1.23 \times 10^8 N_e N_m \epsilon^{-3/2} \int_0^\infty X_E E \exp\left[-\frac{3}{2}\frac{E}{\epsilon}\right] dE, \quad \text{cm}^{-3}\ \text{sec}^{-1} \qquad (17)$$

where ϵ is the average electron energy.

Ionization cross sections for use in solving this equation are shown in Figure 19. The solid line shown in the figure corresponds to the curve fit

$$0 \text{ ev} \leq E \leq 18.2 \text{ ev}: \quad X_E E = 0$$

$$18.2 \text{ ev} \leq E \leq 29 \text{ ev}: \quad X_E E = 2.38\,(E - 18.2) \times 10^{-16} \text{ cm}^2$$

$$29 \text{ ev} \leq E: \quad X_E E = 4.12\,(E - 23) \times 10^{-16} \text{ cm}^2$$

which was selected for ease of integration.

When these values are substituted into equation (17) and the integration performed between the limits of zero and infinity the following result is obtained:

$$n_i(r,t) = 1.30 \times 10^{-8} N_e N_m \sqrt{\epsilon} \left(\exp\left[-\frac{27.3}{\epsilon}\right] + 0.76 \exp\left[-\frac{43.5}{\epsilon}\right]\right), \quad \text{cm}^{-3}\ \text{sec}^{-1}. \qquad (18)$$

The number of recombining collisions per unit volume per unit time $n_r(r,t)$ can be evaluated as follows with the use of the volume recombination coefficient α defined in equations (10) and (11):

$$n_r(r,t) = \alpha N_e^2 = \frac{0.9 \times 10^{-7}}{\sqrt{\epsilon}} N_e^2 , \qquad \text{cm}^{-3}\ \text{sec}^{-1}. \tag{19}$$

The net rate of change of electron density is given by

$$\frac{dN_e(r,t)}{dt} = n_i - n_r, \qquad \text{cm}^{-3}\ \text{sec}^{-1}. \tag{20}$$

The electron density at some time t is equal to the integral of this equation. It can be rewritten in terms of electron density and mean energy as follows:

$$\frac{dN_e(r,t)}{dt} \tag{21}$$

$$= 1.30 \times 10^{-8} N_e N_m \sqrt{\epsilon} \left(\exp\left[- \frac{27.3}{\epsilon} \right] + 0.76 \exp\left[- \frac{43.5}{\epsilon} \right] \right) - 0.9 \times 10^{-7} \frac{1}{\sqrt{\epsilon}} N_e^2 .$$

At this point we have the two equations, equations (14) and (21) for the two unknown quantities $N_e(r,t)$ and $\epsilon(r,t)$. Although $\epsilon(r,t)$ does not appear explicitly in equation (14), W and ϵ are functions of $E(r,t)/p$ and so a relationship between the two can be established from Figures 18(a) and 18(c). Since equation (21) is nonlinear it is more readily integrated on a step-by-step basis by Euler's method. For a sufficiently small time interval, the integral of equation (21) can then be rewritten as

$$N_e(r,\delta t) = N_e(r,0) + \frac{dN_e(r,0)}{dt}\,\delta t \qquad (22)$$

where $N_e(r,0)$ and $N_e(r,\delta t)$ refer to electron density evaluated before and after the time interval δt.

Even though $N_e(r,\delta t)$ can be found if $N_e(r,0)$ and $\epsilon(r,0)$ are specified, $\epsilon(r,\delta t)$ cannot be found without further numerical manipulation. Equation (14) cannot be integrated because $W[E(r,t)/p]$ is not known as an analytic function of radius, so it is necessary to resort to an iteration scheme to find the solution to equations (14) and (22). The essential steps are listed below.

1) Start with the given quantities: $N_e(r,0)$, $\epsilon(r,0)$, $I(\delta t)$.
2) Calculate $\frac{dN_e(r,0)}{dt}$ from equation (21).
3) Calculate $N_e(r,\delta t)$ from equation (22) for a suitably small value of δt.
4) Guess $E(0,\delta t)/p$ and find $E(r,\delta t)/p$ from equation (15).
5) Find $I(\delta t)$ from equation (14) and Figure 18(a) by performing the radial integration numerically using Simpson's rule.
6) Compare $I(\delta t)$ found in step 5) with the given value of $I(\delta t)$, and repeat 4) and 5) until agreement is obtained.
7) With final values of $E(r,\delta t)/p$, find $\epsilon(r,\delta t)$ as a function of radius from Figure 18(c).
8) Proceed to next time interval.

The process can be repeated as many times as necessary to give $N_e(r,t)$ and $\epsilon(r,t)$ for every value of radius and time during the entire spark duration. Once these two parameters are known, current density can be computed from equation (13) and Figure 18(a).

It is apparent that arbitrary values of $N_e(r,t)$ and $\epsilon(r,t)$ will have to be used at the start of the computation. In the present study it was found that the initial values of $N_e(r,t)$ had little effect on the final results as long as they were three orders of magnitude below the final values. It was possible to make a good approximation of the initial value of $\epsilon(r,t)$ by using the value corresponding to the gap-breakdown voltage.

Intensity Profile - As the entire process above rests heavily on the assumed radial variation in electric field strength, it is desirable to refine the calculations by use of a more accurate representation of the electric field shape. Such a representation can be obtained if the exponent $3/2$ in equation (15) is changed and the intensity distribution is recomputed. By trial and error, the value of the exponent giving the best agreement between computed and measured intensity profiles can be found.

Some uncertainty arises in the comparison of computed and measured intensity profiles because of three-dimensional effects in the measured profiles. Light intensities measured by both methods discussed in Chapter 4 included radiation emitted over a finite depth of field. The computation procedure, on the other hand, will yield intensities corresponding to radiation emitted only in the plane of spark centerline.

Sawyer (1963) gives a discussion of the performance of an optical system similar to the one used in the present study (Figure 6) and points out that for a large uniform source every plane normal to the optical axis will contribute equally to the measured intensity. If the source is sufficiently small, the measured intensity will be zero unless the source is located at the focal point of collimating lens, (the focal point being in the plane of the spark centerline). The sparks studied here were between these two size extremes. Consequently, a convenient method of correcting the measured intensities was not available, so no correction was applied to the intensity-profile measurements.

The intensity at any point in the spark is directly proportional to the number density of excited emitters, that is, the number density of molecules in the $C^3\pi$ state. As in the case of the electron concentration, the number of emitters is determined by the difference between the excitation rate and the de-excitation rate.

The excitation rate is given by equations (16) and (17) if the excitation cross section is substituted for the ionization cross section. The excitation-cross-section data shown in Figure 19 are derived from values given by Langstroth (1934) in ratio form and are the sum of his measured intensities of the (0,2), (1,3), and (2,4) bands in the nitrogen second-positive system. In Figure 19, these intensities were converted to cross sections on the basis of the assumption that the maximum value of the excitation cross section and the maximum value of the ionization cross section are equal, as discussed previously. The broken line in Figure 19 corresponds to the curve fit

$$0 \text{ ev} \leq E < 15 \text{ ev}, \qquad X_E E = 0$$

$$15 \text{ ev} \leq E, \qquad X_E E = 52 \times 10^{-16} \text{ cm}^2$$

which was selected, as before, for ease of integration. When this is substituted into equation (17) and the integration performed over the range of electron energy between zero and infinity, the following result is obtained for the number of exciting collisions per unit volume per unit time:

$$n_x(r,t) = 43 \times 10^{-8} N_e N_m \frac{1}{\sqrt{\epsilon}} \exp\left[-\frac{22.5}{\epsilon}\right], \quad \text{cm}^{-3} \text{ sec}^{-1}. \qquad (23)$$

De-excitation (or radiative transition) takes place at a rate that depends on the transition probability and the number density of the excited emitters. Nicholls (1964) lists the transition probabilities for all bands in the nitrogen second-positive system. The probability of a radiative transition from a given vibrational level of the $C^3\pi$ state is the sum of the transition probabilities of all transitions from that vibrational level. In this study, the behavior of the zeroth vibrational level of the upper state is assumed to be representative of the entire upper state, since the zeroth level is the most heavily populated. The sum of the transition probabilities of all transitions from the zeroth vibrational level is 2.243×10^7 per second. The number of transitions per unit volume per unit time can therefore be written as

$$n_t(r,t) = 2.243 \times 10^7 N_u, \qquad \text{cm}^{-3}\ \text{sec}^{-1} \qquad (24)$$

where $n_t(r,t)$ is the rate of transitions per unit volume

N_u is the number of molecules in the upper excited state per unit volume.

The net rate of change of the number of upper-excited-state molecules per unit volume can now be expressed as

$$\frac{d}{dt} N_u(r,t) = n_x - n_t, \qquad (25)$$

where $\frac{d}{dt} N_u(r,t)$ is the derivative of $N_u(r,t)$, evaluated at radius r and time t.

This expression can be rewritten as

$$\frac{dN_u}{n_t - n_x} = - dt. \qquad (26)$$

If a sufficiently small interval of time is chosen, the excitation rate $n_x(r,t)$ can be considered to be invariant with time and equation (26) can be rewritten as

$$\frac{d(2.243 \times 10^7 N_u - n_x)}{(2.243 \times 10^7 N_u - n_x)} = - 2.243 \times 10^7 dt, \qquad (27)$$

when equation (24) is substituted for n_t. The solution of this equation is

$$2.243 \times 10^7 N_u - n_x = C\, e^{-2.243 \times 10^7 t} \tag{28}$$

and the constant can be evaluated by letting $N_u(r,t) = N_u(r,0)$ when $t = 0$. This gives as a final result, for a small time interval δt,

$$N_u(r,\delta t) = n_x(r,0)\, \frac{(1 - e^{-2.243 \times 10^7 \delta t})}{2.243 \times 10^7} + N_u(r,0)\, e^{-2.243 \times 10^7\, \delta t} . \tag{29}$$

The electric field strength and electron number density were evaluated previously as a function of radius for the entire spark process. The intensity profile, which is equivalent to the radial distribution of $N_u(r,t)$, can be found for all times during the process, since $N_u(r,t)$ is zero at the start of the spark. In the event that the computed and measured intensity profiles do not agree with each other, the exponent in equation (15) can be increased to make the computed profile more peaked or decreased to make it flatter.

Energy Transfer by Electron Collisions - The spark heating rate can be found from an examination of the number of collisions undergone by the average molecule and the energy transferred to the various modes of excitation as a result of each collision. The primary means of energy transfer is through electron collisions, and this aspect will be examined here.

The total number of electron-molecule collisions per unit volume per unit time is given by

$$n_c(r,t) = N_e \bar{v}_e \frac{1}{\ell_e} , \qquad cm^{-3} \text{ sec}^{-1} \qquad (30)$$

where $\bar{v}_e$ is the average electron velocity, and

ℓ_e is the electron mean free path, from Figure 18.

If the electrons have a Maxwellian velocity distribution, equation (30) can be rewritten as

$$n_c(r,t) = 0.546 \times 10^8 N_e \sqrt{\epsilon} \frac{1}{\ell_e} , \qquad cm^{-3} \text{ sec}^{-1} . \qquad (31)$$

As discussed earlier in this chapter, the mean fractional energy transfer per collision to rotational excitation is 2.72×10^{-4}. The corresponding value for translational excitation is 0.39×10^{-4}. The energy transferred by electron collisions per unit time per unit volume to rotational and translational excitation can therefore be written as

$$\frac{d}{dt} E_{R_c}(r,t) = 2.72 \times 10^{-4} n_c \epsilon = 1.48 \times 10^4 N_e \epsilon^{3/2} \frac{1}{\ell_e} ,$$

$$ev/cm^3 \text{ sec} , \qquad (32a)$$

$$\frac{d}{dt} E_{T_c}(r,t) = 0.39 \times 10^{-4} n_c \epsilon = 0.21 \times 10^4 N_e \epsilon^{3/2} \frac{1}{\ell_e} ,$$

$$ev/cm^3 \text{ sec} . \qquad (32b)$$

The energy transferred to vibrational excitation by electron collisions can be obtained if the sum of the energy transfer to other modes of excitation is subtracted from the total energy transfer. In addition to the rotational and translational excitation just discussed, ionization and electronic excitation must be considered. The energy expended on ionization is equal to the product of the number of ionizing collisions, given by equation (18), and the ionization energy, 15.7 ev. Similarly, the energy expended exciting the second-positive band system, the principle mode of electronic excitation, is equal to the number of exciting collisions, given by equation (23), and the excitation energy, 11.05 ev. We have not considered other types of excitation, such as dissociation by electron impact or excitation of other band systems, because the energy represented is negligibly small compared with the total energy transfer. The energy transferred to vibrational excitation by electron collision is therefore

$$\frac{d}{dt} E_V(r,t) = \eta n_c \epsilon - \frac{dE_{R_c}}{dt} - \frac{dE_{T_c}}{dt} - 15.7\, n_i - 11.05\, n_x, \quad \text{ev/cm}^3 \text{ sec.} \qquad (33)$$

Energy Transfer by Atom and Molecule Collisions - In general, molecules on the average each experience the same gain of energy as a result of electron collisions, and the contribution of atom or molecule collisions is not important. There are two instances where atom or molecule collisions must be considered, however. First, molecules that undergo collisions with unusally energetic electrons and become ionized or electronically excited can later undergo collisions with other molecules, transforming

this ionization or electronic excitation energy into other modes of excitation, such as translational or rotational kinetic energy. Second, if we wish to examine any single heating process discussed previously, we must take into account the net energy transfer to or from that mode of excitation by means of molecule collisions.

As discussed earlier in this chapter, the most probable recombination process in nitrogen is the dissociative recombination process. As a result of each recombination collision, an energy of 5.82 electron volts is added to the rotational and translational kinetic energy of the gas. The additional energy per unit volume per unit time due to dissociative recombination collisions can be expressed with the aid of equation (19) as

$$\frac{d}{dt} E_D(r,t) = 5.82\ n_r = \frac{5.25 \times 10^{-7}}{\sqrt{\epsilon}} N_e^2, \quad \text{ev/cm}^3 \text{ sec} . \qquad (34)$$

After dissociation occurs, this additional energy is transferred to the surrounding molecules through atom-molecule collisions, and it can be assumed that the additional energy is equally partitioned between the three translational and two rotational degrees of freedom.

Although a similar collisional de-excitation process is possible in the case of electronic excitation, it does not appear to be an important part of the spark process in pure nitrogen. In cases where such collisional de-excitation has occurred, it has usually been attributed to the presence of contaminants.

Relaxation processes (that is, the transfer of energy from one mode of excitation to another) are even more important to the present

study than the addition of energy through the dissociative recombination discussed above. This is a consequence of the widely differing fractional energy transfer per electron collision to the various molecular degrees of freedom. An examination of the magnitudes of the individual terms in equation (33) shows that for moderate values of electric field strength most of the energy transferred by electron collisions appears as vibrational excitation. Therefore, the ratio of vibrational energy transfer to rotational energy transfer to translational energy transfer is $\eta : 3.11 \times 10^{-4} : 0.39 \times 10^{-4}$ or, for an electric field strength of 30 v/cm/mm Hg, roughly $1:10^{-2} : 10^{-3}$. It appears, then, that any computation of rotational temperature in the spark must account for energy transferred from vibrational excitation or to translational excitation through relaxation processes.

Herzfeld and Litovitz (1959) report a vibrational relaxation time of $0.4 \times 10^{6}\ \tau_m$, and Greenspan (1959) lists a rotational relaxation time of $5.26\ \tau_m$, where τ_m is the time between molecular collisions experienced by the average molecule. If the values $\ell_m = 6.7 \times 10^{-3}$ cm and $\bar{v}_m = 4.75 \times 10^{4}$ cm/sec (corresponding to a pressure of 1.0 mm Hg and temperature of 295°K) are used for molecular mean free path and mean molecular velocity, a molecular collision rate of 7.1 collisions per molecule per microsecond is obtained. This gives a vibrational relaxation time of 5.6×10^{4} microseconds and a rotational relaxation time 0.74 microseconds. Therefore, in the 50-microsecond period that the spark-heated column is being studied, the amount of energy transferred to translational and rotational excitation through vibrational relaxation is small compared to the energy transferred through electron collisions.

The energy transferred to translational excitation through rotational relaxation is significant for the case discussed and must be considered in the computation program.

At this point the energy added to the rotational and translational degrees of freedom can be computed as the summation of the energy transferred through electron collisions, dissociative recombination collisions, and rotational relaxation. The rates of change of rotational and translational energy per unit volume are thus

$$\frac{d}{dt} E_R(r,t) = \frac{dE_{R_c}}{dt} + \frac{dE_{R_r}}{dt} + \frac{0.4\ dE_D}{dt} \tag{35a}$$

$$\frac{d}{dt} E_T(r,t) = \frac{dE_{T_c}}{dt} + \frac{dE_{T_r}}{dt} + \frac{0.6\ E_D}{dt} \tag{35b}$$

where $\frac{d}{dt} E_{R_r}(r,t)$ is the rate of change of rotational energy per unit volume due to rotational relaxation, and

$\frac{d}{dt} E_{T_r}(r,t)$ is the rate of change of translational energy per unit volume due to rotational relaxation.

For energy to be conserved in the rotational-translational relaxation process, we must have the equality

$$\frac{d}{dt} E_{R_r}(r,t) = -\frac{d}{dt} E_{T_r}(r,t) \ . \tag{36}$$

These two derivatives can be evaluated with the aid of the usual relaxation equation, given by Herzfeld and Litovitz (1959) as follows:

$$-\frac{d}{dt} E_{R_r}(r,t) = \frac{1}{\tau_R} [E_R - E_R^*] \tag{37}$$

where τ_R is the rotational relaxation time, and

E_R^* is the value that E_R would have in equilibrium with the translational degrees of freedom.

Since the gas in the spark column was in equilibrium before the spark, Greenspan's value of τ_R can be used to rewrite equation (37) as

$$-\frac{d}{dt} E_{R_r}(r,t) = \frac{1}{5.26\ \tau_m} [\Delta E_R - \frac{2}{3} \Delta E_T] , \tag{38}$$

where ΔE_R is the cumulative increase in rotational energy during the spark process, and

ΔE_T is the cumulative increase in translational energy during the spark process.

For pressures other than 1.0 mm, τ_m can be found by dividing the value for 1.0 mm (0.14 microseconds per collision) by the pressure.

Equations (35), (36) and (38) can now be combined to give final expressions for the rates of increase of rotational and translational energy as follows:

$$\frac{d}{dt} E_R(r,t) = \frac{dE_{R_c}}{dt} - \frac{1}{5.26\ \tau_m} [\Delta E_R - \frac{2}{3} \Delta E_T] + 0.4 \frac{dE_D}{dt} \tag{39a}$$

$$\frac{d}{dt} E_T(r,t) = \frac{dE_{T_c}}{dt} + \frac{1}{5.26\,\tau_m} \left[\Delta E_R - \frac{2}{3} \Delta E_T\right] + 0.6 \frac{dE_D}{dt} \qquad (39b)$$

Equations (33) and (39) form a complete set of differential equations for the energy added to molecular vibration, rotation, and translation. They cannot be solved because of their dependence on the electron number density $N_e(r,t)$, which has been calculated but not expressed in analytical form. The simplification required to get these equations in a form that can be solved will be discussed in the following paragraphs.

Vibrational, Rotational, and Translational Temperature - Because of the form of $N_e(r,t)$ a step-by-step integration process must be used to find the energy added to vibrational, rotational and translational excitation. The approach used in equation (22) will be used again in these computations. Energy added to vibrational excitation can be expressed by replacing equation (33) with the following finite-difference equation

$$\Delta E_V(r,\delta t) = \Delta E_V(r,0) + \left[\eta n_c \epsilon - \frac{dE_{R_c}}{dt} - \frac{dE_{T_c}}{dt} - 15.7\, n_i - 11.05 n_x\right]_{t=0} \delta t \qquad (40)$$

where ΔE_V is the cumulative increase in vibrational energy during the spark process up to time $t = 0$, and

$[\ ]_{t=0}$ indicates that the bracketed quantity is evaluated at $t = 0$ at each radius.

This change in vibrational energy can be expressed as a vibrational temperature if the vibrational energy in the gas before the start of the spark is neglected and the initial vibrational temperature is taken as zero. With these assumptions, vibrational temperature and ΔE_V can be related by the following expressions given by Vincenti and Kruger (1965):

$$\frac{\Delta E_V(r,t)}{N_m} = \frac{k\theta_V}{\exp[\theta_V/T_V] - 1} \tag{41}$$

where N_m is the molecular number density

θ_V is the characteristic temperature for vibration, 3390°K for nitrogen, and

T_V is the vibrational temperature.

For T_V to have any physical meaning in equation (41), the vibrational energy ΔE_V must be distributed among the vibrational energy levels with a Boltzmann distribution. This is probably the case during the final phase of the spark process but not during the initial one. If equation (41) is solved to T_V, the result is

$$T_V = 3390\left[\frac{1}{\log\left(1 + \frac{0.292\ N_m}{\Delta E_V}\right)}\right], \quad °K \tag{42}$$

where we have set $\theta_V = 0.292$ electron volts per molecule.

In a manner similar to that discussed above, equations (39) can be rewritten to facilitate solution:

$$\Delta E_R(r,\delta t) \tag{43a}$$

$$= \Delta E_R(r,0) + \left[\frac{d}{dt} E_{R_c} - \frac{1}{5.25\,\tau_m}\left(\Delta E_R - \frac{2}{3}\Delta E_T\right) + 0.4\,\frac{d}{dt} E_D\right]_{t=0} \delta t$$

$$\Delta E_T(r,\delta t) \tag{43b}$$

$$= \Delta E_T(r,0) + \left[\frac{d}{dt} E_{T_c} + \frac{1}{5.26\,\tau_m}\left(\Delta E_R - \frac{2}{3}\Delta E_T\right) + 0.6\,\frac{d}{dt} E_D\right]_{t=0} \delta t$$

The energy added to rotational or translational excitation, as computed from equations (43), can be expressed in terms of rotational or translational temperature change by use of the principle of equal partition of energy,

$$\Delta E = \frac{N_{df}}{2} k\Delta T$$

where N_{df} is the number of degrees of freedom over which the energy ΔE is distributed.

If the units of energy are electron volts, this can be reduced to

$$\Delta T_R = 11{,}610\ \Delta E_R\ , \qquad {}^\circ K \tag{44a}$$

since there are two degrees of freedom in rotation, and

$$\Delta T_T = 7{,}730\ \Delta E_T, \qquad {}^\circ K \qquad (44b)$$

since there are three degrees of freedom in translation. The absolute values of rotational and translational temperature in the spark column can be found from the sum of the change in temperature given by equations (44) and the initial temperature.

6. ANALYSIS OF THE DECAYING-PLASMA PROCESS

6.1. Behavior of Electrons

As the spark current decays to zero, the nitrogen molecules in the spark column cease to emit radiation in the second-positive band system. This does not signify a change in the nature of the processes occurring in the column, but merely indicates a large reduction in the mean electron energy. When the spark current approaches zero, the electric field strength also approaches zero and the electric field ceases to be the means whereby the electrons regain the energy lost through collisions.

In the present study, it is assumed that the vibrational temperature becomes the factor controlling electron energy once the effect of the electric field is no longer significant. This assumption is based on the work of Clouston et al. (1958), Hurle (1964), and Hurle and Russo (1965). Hurle examined the probability of vibrational de-excitation through molecule-molecule collisions and electron-molecule collisions in the range from 1,000°K to 5,000°K. He found that the probability of de-excitation by an electron-molecule collision at a temperature of 1,000°K is 15,000 times as great as the probability of de-excitation by a molecule-molecule collision. At 1,500°K it is 2,500 times as great. As a result of this and the low efficiency of energy interchange between electrons and translational or rotational excitation, Hurle reasoned that electron temperature will be very close to equilibrium with

vibrational temperature for the range of vibrational temperatures between 1,000°K and 3,000°K.

The validity of this reasoning was demonstrated by the results of experiments performed by Hurle and Russo. These experiments consisted of the measurement of temperature in nozzle flows by means of the sodium-line-reversal technique. The gases used were 100% argon and 99% argon, 1% nitrogen. With the former, the reversal temperature measured in the nozzle at an axial location having an area ratio of 8 was equal to the calculated nozzle-throat temperature, indicating that the electron temperature was "freezing" at the nozzle throat. The addition of 1% nitrogen caused a significant reduction in the measured reversal temperature. This magnitude of reduction could be explained only if it was assumed that the electrons were in equilibrium with the nitrogen vibrational temperature. Additional evidence for this assumption was provided by the agreement between the measured reversal temperature and the computed vibrational temperature.

6.2. Computation of Decaying-Plasma Characteristics

Except for the change in electron temperature just discussed, the decaying-plasma column behaves in a manner similar to the spark column. The same computation procedure can therefore be used to analyze both processes if this change is taken into account.

The electron energy will be in equilibrium with the molecular vibrational energy when the electron temperature and the vibrational

temperature are equal. Electron energy in ev and temperature in °K are related by the following equation:

$$\epsilon = \frac{3}{2} kT_e = \frac{1}{7,730} T_e \cdot \tag{45}$$

In the absence of the electric field, electron energy was assumed to be given by equation (45) with $T_e = T_V$, and the electron mean free path was assumed to be the mean free path in Figure 18 corresponding to this electron energy. With this assumption, appropriate equations in the previous sections can be solved for the total number of electron collisions, the number of electronic excitation, ionization, and recombination collisions, the electron density, and the vibrational, rotational, and translational temperatures. It should be noted, however, that equation (33) can be rewritten as

$$\frac{dQ(r,t)}{dt} = \eta n_e \epsilon = \frac{dE_{R_c}}{dt} + \frac{dE_{T_c}}{dt} + \frac{dE_V}{dt} + 15.7\, n_i + 11.05\, n_x, \quad \text{ev/cm}^3 \text{ sec}$$

where $Q(r,t)$ is the work done on the electrons by the electric field.

In the decaying plasma, dQ/dt is zero, therefore the term $\eta n_e \epsilon$ is also zero. This result is to be expected since η is the fractional energy loss per collision, and if the electron energy is maintained in equilibrium with vibrational temperature, there is no net energy loss through collisions.

During the decaying-plasma process, any energy going into other forms of excitation, such as translational or rotational excitation, via electron

collisions in the decaying plasma must be supplied at the expense of vibrational energy. As a consequence, the vibrational energy can be expected to decrease while the translational and rotational energy increase. Although ionization and electronic excitation continue, the rates will be very small compared to the rates occurring during the spark.

7. RESULTS OF COMPUTATIONS

7.1. Intensity Profiles

Integrated intensity profiles were computed for the 0.5-joule spark at 1.0 mm pressure without a magnetic field and with a 655-gauss magnetic field so that an accurate representation of the electric field shape could be obtained. These profiles are shown in Figure 20. In Figure 20(a) it is seen that the computed intensity profile for the spark without a magnetic field is more sharply peaked than the measured profile when the exponent 3/2 is used in equation (15) for electric field shape. An exponent of unity gives a better representation of the integrated intensity profile, as can be seen in the figure. This change in exponent causes a flattening of the computed electric field, suggesting that the electrode tips do not act as infinitesimal points as assumed, but act instead as finite surfaces.

In the case of the spark with a 655-gauss magnetic field (Figure 20(b)), a suitable intensity profile could not be obtained with an electric field shape given by equation (15) because of the rapid decrease in intensity with increasing radius near the center of the spark and the almost constant intensity at radii between 1.5 cm and 3 cm. It was found by trial and error that an electric field strength, decreasing in a linear manner with increasing radius, given by the equation

$$E(r,t)/p = [1 - 0.55\ r/D]\ E(0,t)/p, \qquad (46)$$

would yield a satisfactory intensity profile, so this was used for all further computation where a 655-gauss magnetic field was applied. The integrated intensity profile computed on the basis of equation (46) is shown in Figure 20(b), identified as "computed, equation (46)."

Computed luminosity, defined as the radial integral of computed intensity, is shown in Figure 21 as a function of time. Also shown in the figure are measured luminosity and current. In both Figure 21(a) and 21(b), it is seen that the computed luminosity is lower than the measured value at the final phase of the spark. This is probably a consequence of the following situation: Luminosity measurements were used to establish the spark duration, and the period of low luminosity near the end of the spark was masked by noise and not counted as a part of the spark duration. The actual spark duration, therefore, was probably a little longer than the 0.8-microsecond value used in the computations. It is apparent that if a longer duration had been used, better agreement with measured luminosity would have been obtained. The disagreement was not judged serious enough to warrant the additional expense of repeating the calculations, however. Aside from this discrepancy, it can be seen from a comparison of computed luminosity and current in Figure 21 that a good approximation to the current-time relationship can be obtained from luminosity measurements.

Instantaneous intensity profiles computed for a number of different values of time are shown in Figure 22 along with the corresponding measured values of intensity. All have been normalized so that the centerline value in each case has a magnitude of unity. This permits the shape of the computed and measured profiles to be compared even though the luminosities differed, as discussed above. In Figure 22(a) it is seen that the shape of the computed intensity profile for the zero-gauss magnetic field case has the same variation with time as the measured profile. Profiles obtained during the early phase of the spark are flat; those obtained later are more sharply peaked. The cause of this will be discussed in Section 7.3. The computed intensity profiles for the 655-gauss case show the same trend, but the measured values do not. It is apparent, therefore, that the effects of the magnetic field cannot be represented accurately by a simple change in the electric field shape.

7.2. Spark Temperature

The computed rate of change of rotational temperature is shown as a function of time in Figure 23 for the 0.5-joule spark at 1.0 mm pressure without a magnetic field and with a 655- gauss magnetic field. The straight lines shown on the figure are the rates given by the curve-fitted lines in Figure 12, and have been drawn only between 0.15 microseconds and 0.65 microseconds. A comparison of the computed rates with the experimentally derived values shows that the computed rate of change of temperature is, on the average, about two-thirds as great as the value indicated by measurements.

The computed rate of change of translational temperature for each case is also shown in Figure 23. The figure thus shows the computed departure from equilibrium between the translational and rotational temperatures. An experimental study of the rate of change of translational temperature is not possible at present because the measuring technique gives rotational temperature only.

A direct comparison between computed and measured temperatures can be obtained if the computed increase of temperature is added to the initial temperature present during the experiments. When this is done, however, the computed temperature is 50°K to 60°K less than the measured temperature over the entire spark duration. The most probable reason for this discrepancy is coupling between rotational and electronic excitation. As discussed earlier, the computation of rotational temperature is based on the assumption that the average fractional energy transfer per electron collision to rotational excitation is 2.72×10^{-4} for all values of electron energy. Since electronic excitation results from collisions with electrons having, on the average, an energy of about 18 ev, it can be anticipated on this basis that the average exciting collision will simultaneously increase the rotational kinetic energy by about 0.0049 ev, which corresponds to 57°K. Since the emitters comprise a very small fraction of the total number of molecules, it appears that on excitation, the average emitters have a rotational temperature about 57°K higher than the average molecular rotational temperatures.

Actually, some of the excess rotational kinetic energy will be lost through collisions with other molecules before emission occurs. As a result, the rotational temperature indicated by the emitted radiation

will be less than 57°K above the actual gas temperature. The fraction of this excess energy lost through molecular collisions before emission can be computed as follows on the basis of the electronic transition probability and the rotational relaxation time.

As a first step, we define the electronic relaxation time τ_e as the reciprocal of the transition probability. The number of transitions per unit time per unit volume can be expressed as a function of τ_e by rewriting equation (24) as

$$n_t(t) = \frac{1}{\tau_e} N_u, \tag{47}$$

neglecting, for the moment, any radial variation. If we examine a class of emitters that became excited at a specified time $t = 0$, the rate of change of the number density of the class will be the negative of the transition rate, that is,

$$\frac{dN_u(t)}{dt} = -n_t = -\frac{1}{\tau_e} N_u . \tag{48}$$

If we define $N_u(0)$ as the value of N_u when $t = 0$ (that is, the initial value of N_u), the solution of equation (48) for the number of emitters at time t is

$$N_u(t) = N_u(0)\, e^{-(t/\tau_e)} . \tag{49}$$

With this value, the change in the number of emitters occurring between (t) and $(t + \delta t)$ can be written as

$$\delta N_u(t) = -N_u(0)\, e^{-(t/\tau_e)}\, \frac{\delta t}{\tau_e}\,, \tag{50}$$

and the probability that a given member of the class of emitters will undergo a transition in the time interval (t) to $(t+\delta t)$ is

$$P(t)\,\delta t = \frac{\delta N_u(t)}{N_u(0)} = e^{-(t/\tau_e)}\, \frac{1}{\tau_e}\,\delta t\,.$$

Assume that the original $N_u(0)$ emitters each have an excess rotational energy due to excitation collisions. The average rate at which this excess energy is given up through relaxation as a consequence of molecular collisions after excitation can be expressed as in equation (37) as

$$\frac{de_R}{dt} = -\frac{1}{\tau_R}\,(e_R - e_R^*) \tag{51}$$

where e_R is the rotational kinetic energy per molecule, and

e_R^* is the local equilibrium value of e_R.

If the number of emitters is small compared with the total number of molecules, e_R^* will be equal to the energy that the emitters had before excitation. If we then set

$$e_R - e_R^* = \Delta e_R$$

and substitute this into equation (51), we can write the rate of change of energy due to relaxation as

$$\frac{de_R}{dt} = \frac{d\Delta e_R}{dt} = -\frac{1}{\tau_R}\ \Delta e_R \ . \tag{52}$$

This has the solution

$$\Delta e_R(t) = \Delta e_R(0)\ e^{-(t/\tau_R)} \tag{53}$$

where $\Delta e_R(0)$ is the value of $\Delta e_R(t)$ when $t = 0$.

The average member of the class of molecules which is still in an electronically excited state at time t will have lost an amount of rotational energy given by

$$\Delta e_R(0) - \Delta e_R(t) = \Delta e_R(0)\left[1 - e^{-(t/\tau_R)}\right] . \tag{54}$$

If δN_u of the class of molecules undergo an electronic transition during the time interval between (t) and $(t+\delta t)$, they will have lost (prior to the transition) rotational energy due to collisions in an amount

$$\delta N_u[\Delta e_R(0)]\ [1 - e^{-(t/\tau_R)}] = \Delta e_R(0)\ \frac{N_u(0)}{\tau_e}\ e^{-(t/\tau_e)}\ [1-e^{-(t/\tau_R)}]\ \delta t$$

The total rotational energy lost by collisions is the integral of this expression over the time of observation. The average fractional excess rotational energy loss by collisions prior to emission is then

$$\bar{H} = \frac{1}{\tau_e} \int_0^{t_{obs}} e^{-(t/\tau_e)} \left[1 - e^{-(t/\tau_R)}\right] dt \quad . \tag{56}$$

For an observation time t_{obs} sufficiently long, equation (56) can be written as

$$\bar{H} \approx \frac{\tau_e}{\tau_e + \tau_R} \tag{57}$$

For the case under discussion, we have

$$\tau_e = (2.243 \times 10^7)^{-1} \text{ sec} = 0.0445 \times 10^{-6} \text{ sec}$$

$$\tau_R = 0.74 \times 10^{-6} \text{ sec}$$

from which we obtain

$$\bar{H} = .057 \quad .$$

This result can be expressed as follows: If an incremental amount of energy Δe_R is transferred to molecular rotational excitation during an electronic excitation collision, an average fraction of this excess rotational energy equal to $\tau_e/(\tau_e + \tau_R)$ will be lost by the emitters through molecular collisions prior to emission. On the basis of this

result, the computed emitter rotational temperature can be written as

$$T_R(r,t) = T_0 + \Delta T_R(r,t) + (2.72 \times 10^{-4})(\bar{E}(r,t))\ (11{,}610)\ (1-\bar{H})$$

$$= 295 + \Delta T_R(r,t) + 2.98\ \bar{E}(r,t), \quad °K \tag{58}$$

where T_0 is the gas temperature before the spark, 295°K

$\bar{E}(r,t)$ is the mean energy of exciting electrons, in units of ev.

The mean energy of the exciting electrons $\bar{E}(r,t)$ is evaluated from the relation

$$\bar{E} = \frac{\int_0^\infty X_E\, N_E E\, dE}{\int_0^\infty X_E\, N_E dE} \tag{59}$$

which can be reduced to

$$\bar{E}(r,t) = 15 + (2/3)\ \epsilon(r,t), \qquad \text{ev}$$

for the excitation collision cross section represented by the broken line in Figure 19. With the substitution of this value, equation (58) can be rewritten as

$$T_R(r,t) = 339.7 + \Delta T_R(r,t) + 1.99\ \epsilon(r,t), \quad °K\ . \tag{60}$$

Emitter rotational temperatures computed on the basis of equation (60) for the spark centerline are shown in Figure 24. The curve-fit lines from Figure 12 for the 0.5-joule spark at 1.0 mm pressure without a magnetic field and with a 655-gauss magnetic field are also shown in the figure. The rates of change of temperature indicated by the computed data in Figure 24 are somewhat less than the corresponding rates of change shown in Figure 23. This is a consequence of the dependence of T_R in equation (60) on the mean electron energy which, as will be discussed in Section 7.3, decreases monotonically during the spark. Nevertheless, the agreement between the computed and measured values of rotational temperature is good, particularly when it is considered that the fractional-energy-transfer measurements obtained for mean electron energies of 0.5 ev or less have been applied to a case where the mean electron energy is approximately 20 ev. This situtation was brought about by an absence of measurements of energy transfer to translational and rotational excitational for electron energies higher than 0.5 ev.

Although the preceding discussion demonstrates the plausibility of the argument that the sudden initial increase in measured temperature is due to coupling of electronic and rotational excitation, and therefore affects only a small number of molecules, the discussion does not rule out the possiblity that the initial temperature increase is a general increase affecting all molecules. An examination of the measured and computed intensity profiles and the computed current densities can be used to show that such a possibility is highly unlikely. This will be done in the following paragraphs.

The relationship between current density and rate of increase of rotational energy due to electron collisions can be examined readily with the use of equations derived in Section 5.3. If equation (13) is used to eliminate N_e from equation (32a), the final result is

$$\frac{d}{dt} E_{R_c}(r,t) = 9.3 \times 10^{22} \frac{(\epsilon)^{3/2}}{W \ell_e} J, \quad \text{ev/cm}^3 \text{ sec} . \tag{61}$$

The quantities ϵ, W, and ℓ_e are functions of electric field strength only, so equation (61) can be used to find the rate of rotational energy increase per unit current density as a function of electric field strength. The results obtained from equation (61) on the basis of the electron data of Figure 18 are shown in Figure 25. The most significant feature of the results is that the rate of rotational energy increase has a maximum value of about 4.0×10^{18} ev/cm^3 sec at an electric field strength of 1.2 volts/cm/mm Hg. At field strengths higher than this value, the rate of rotational energy increase is reduced.

The curve-fit line in Figure 12 for the zero-gauss spark gives a rotational temperature of 357°K at a time of 0.15 microseconds. This corresponds to a spark-centerline rotational temperature increase of 62°K in 0.15 microseconds, or 413°K per microsecond. Since the computed intensity profiles in Figure 22(a) were in good agreement with the measured profiles, the computed current densities can be used with some degree of confidence. The computed average centerline current density over the first 0.15 microseconds is 4.0 amps/cm^2. When this value is multiplied by the maximum predicted rate of rotational energy increase from Figure 25, the result is

$$\frac{d}{dt} E_{R_c}(r,t) = 16 \times 10^{18} \text{ ev/cm}^3 \text{ sec},$$

which gives a maximum predicted rate of rotational temperature increase of 5.6°K per microsecond for the molecule density under consideration.

The foregoing discussion shows that if the initial measured temperature increase were a general increase in rotational temperature affecting all molecules, it would be seventy-five times as great as the maximum such increase predicted by the theory. Such a discrepancy is unlikely in view of the relatively good agreement between computed and measured rates of temperature increase for the period of time between 0.15 and 0.65 microseconds.

7.3. Effects of Changes in the Spark Parameters

Intensity Profile - Once the electric field shape was evaluated, spark characterisitics were computed for sparks with additional values of pressure and spark energy. In all cases an exponent of unity was used in equation (15) for the electric field shape; the effects of the magnetic field were not examined further. The combinations of spark energy and static pressure studied were as follows:

a) 0.05 joules, 1.0 mm

b) 0.5 joules, 0.1 mm

c) 0.5 joules, 1.0 mm (discussed previously)

d) 0.5 joules, 10 mm

e) 5.0 joules, 1.0 mm.

The objectives of this part of the study were to provide a further check of the computation procedure and to calculate the effects of the spark parameters on the initial electron-density profiles.

As a check of the validity of the computation procedure, integrated intensity profiles for the five cases were computed and plotted in Figure 26. It can be seen that the effect of decreasing either the static pressure or spark energy is to widen the integrated intensity profile. Similar trends are exhibited by the measured normalized spark radii without a magnetic field presented in Figure 16. In that figure the radius is seen to increase with decreasing pressure for all three values of spark energy. When the spark energy was decreased from 5.0 joules to 0.5 joules, the spark radius increased. When spark energy was decreased from 0.5 joules to 0.05 joules, however, the radius decreased. The reason for this apparently erratic behavior seems to be that the amount of light from the 0.05-joule spark is insufficient to make a good photographic exposure. The film nonlinearity, as a result, makes the spark image appear more narrow than it would if it had been properly exposed. Except for this one inconsistency, the results of the calculations are borne out by the experiments.

A significant depopulation of the ground state was found in the calculations for the 5.0-joule spark. As a consequence, its integrated intensity profile is open to some question. The other profiles are thought to be valid, since only a small fraction of the total number of molecules were electronically excited during the spark.

The causes for the spark width to vary in the manner described above can be seen in Figure 27, where the field strength at the spark centerline is plotted as a function of time for all five cases. Two trends are clear in the figure: 1) Field strength is increased throughout the spark duration if pressure is decreased. 2) Field strength decreases with increasing time in such a manner that the mean value is reduced if the spark duration is increased. If it is recalled that the lowest spark energy corresponded to the shortest spark duration, and conversely, we are able to identify the cases having relatively greater spark width as those having relatively higher mean field strength.

The reasons for this trend are as follows: Lower pressures mean higher field strengths because of a reduction in the number of molecules N_m and a proportional reduction in the rate of ionizing collisions $n_i(r,t)$ (equation (18). This requires a higher field strength to carry the current with the reduced number of electrons (equation (14)). The electric field strength drops during the spark lifetime because the ionization rate exceeds the recombination rate and, as a consequence, the number of electrons increases. By virtue of equation (14), the required field strength decreases. This process tends to be self canceling as the ionization rate is drastically reduced by the reduction in field strength. High field strengths tend to make the sparks wider because of the nonlinear variation of the rate of exciting collisions $n_x(r,t)$ with electron energy ϵ, and hence with field strength. As a result, an increase in field strength will cause $n_x(r,t)$ to increase a smaller percentage in the center of the spark (where field strength is larger) than at the edge (where it is smaller), making the edge of the spark relatively brighter.

The correspondence between high field strength and wide sparks explains why the intensity profiles in Figure 22(a) tend to be flat during the early phase of the spark duration and more peaked during the latter phase; the electric field strength is higher during the early phase. Although the computed profiles in Figure 22(b) also follow this trend, the measured profiles do not. It appears that a magnetic field is most effective in reducing the spark width during the early phase of the spark, when the field strength is highest and the electrons are the most energetic.

Electron-Density Profiles - Electron-density profiles corresponding to the time of termination of the spark have been computed for all five cases listed earlier and are shown in Figure 28(a). Also shown is the electron-density profile for the 0.5-joule spark at 1.0 mm pressure with a 655-gauss magnetic field. The electron-density profiles are much less peaked than the integrated intensity profiles, but show the same change in profile shape when pressure is changed.

It can be seen also in Figure 28(a) that an increase in spark energy from 0.05 joules to 5.0 joules increases the peak ionization level by a factor of six. Kyser (1964) found that such an increase would increase the integrated intensity by about a factor of 100. It appears, therefore, that the electron-density level is much less sensitive than the luminous intensity to changes in the spark parameters.

It is of interest to note that the largest electron density for the sparks at 1.0 mm pressure corresponds to an ionization level of 0.07%.

The peak electron density for the 0.1-mm spark corresponds to an ionization level of 0.13% and for the 10-mm spark to 0.004%.

Average Spark Temperatures - The validity of the temperature calculations for the 0.5-joule spark at 1.0 mm pressure with and without a magnetic field was demonstrated by a comparison with the measured temperature history in Figure 24. Similar measurements are not available for the other cases under study. It is possible, however, to compute an average temperature for each of these cases and compare these average temperatures with the measured average values of Figure 13. Since the measured average values were, by the nature of the averaging process, weighted according to the instantaneous light intensity, the corresponding computed averages must be obtained by a similar process.

As a first step, equation (58) is rewritten in the form

$$\tilde{T}_R(r) = 295 + \Delta\tilde{T}_R(r) + 2.98\,\tilde{E}(r), \qquad {}^\circ K \qquad (62)$$

where $\tilde{T}_R(r)$ is the average rotational temperature,

$$\Delta\tilde{T}_R(r) = \frac{\int_0^{\tau_s} \Delta T_R \, I dt}{\int_0^{\tau_s} I dt},$$

$$\tilde{E}(r) = \frac{\int_0^{\tau_s} \bar{E} \, I dt}{\int_0^{\tau_s} I dt},$$

τ_s is the spark duration, and

I is the spark intensity at the point under study.

On the basis of equation (62) average rotational temperatures of 350°K, 352°K and 385°K were computed for the 0.05-joule, 0.5-joule and 5.0-joule sparks at 1.0 mm pressure. The averages of the corresponding measured values from Figure 13 are 382°K, 364°K and 421°K. An average temperature of 379°K was computed for the 0.5-joule spark at 1.0 mm pressure with a 655-gauss magnetic field, compared to a measured value of 385°K. In these five cases, it is seen that the computed values are an average of about 20°K lower than the measure values.

To compute average temperatures for the remaining two cases, the factor $\tilde{H}$ in equation (57) is recomputed for the rotational relaxation times corresponding to pressures of 0.1 mm and 10.0 mm. These computations give average spark temperatures of 362°K and 332°K for pressures of 0.1 mm and 10 mm, compared with measured values of 348°K and 385°K. The reasons for the relatively poor agreement between computed and measured values for these two cases are not known.

7.4. Decaying-Plasma Process

Recombination of Ions and Electrons - The most significant aspect of the decaying-plasma process in the spark-heated column is the recombination of free electrons. Electron-density profiles are plotted in Figure 28(b) for a time of 50 microseconds after the initiation of the spark. A

comparison of these profiles with those of Figure 28(a) shows that the peak values are reduced by a factor of 50 to 100 during the 50 microseconds and that the profiles have become very much flatter. The profile flattening is due to the nature of the recombination rate, given by equation (19). This can be seen if equation (19) is substituted into equation (20) for n_r and n_i is set equal to zero, which gives

$$\frac{dN_e(r,t)}{dt} = - \frac{0.9 \times 10^{-7}}{\sqrt{\epsilon}} N_e^2(r,t) \tag{63}$$

Since ϵ changes little with time in the decaying plasma it can be assumed constant in time and equation (63) then has a solution,

$$\frac{1}{N_e(r,t)} = \frac{1}{N_e(r,0)} + \frac{0.9 \times 10^{-7}}{\sqrt{\epsilon}} t \tag{64}$$

where $N_e(r,0) = N_e(r,t)$ at $t = 0$. If $N_e(r,0)$ is the electron density when the spark terminates, it is apparent from Figure 28(a) that its value is strongly dependent on radius. The time-dependent term has very little dependence on radius, however, since $\sqrt{\epsilon}$ does not vary appreciably. After 50 microseconds, the time-dependent term has a magnitude of about 10^{-11} for all values of radius, completely overwhelming the radius-dependent term wherever the initial number density is greater than about 10^{12} electrons/cm^3. As can be seen in Figure 28(a), this represents virtually the entire ionization profile.

The conclusion that can be drawn here is that, although the electron number density in the spark-heated column remains at a level well above that of the surrounding gas, electron-ion recombination will severely

flatten the elctron-density profile. This flattening can be avoided to some degree by an overall reduction in the initial electron density, but such a corrective measure is apt to reduce the electron density in the spark-heated column to a level close to that of the surrounding gas.

Diffusion of Electrons - On the basis of the electron-density profiles of Figure 28(b), the electron-diffusion problem can be studied. The most significant factor in the diffusion problem is whether the diffusion occurs as electron diffusion or ambipolar diffusion. If electron diffusion occurs, it will probably have a significant effect on the electron-density profile. Electron diffusion occurs only in plasmas of relatively low electron density, where the Debye length is greater than the electron mean free path. The Debye length is given by the expression

$$\lambda_D = 6.9 \left(\frac{T_e}{N_e} \right)^{1/2} , \qquad \text{cm} . \tag{65}$$

The centerline electron density for the 0.5-joule spark at 1.0 mm pressure without a magnetic field is 10.64×10^{10} electrons/cm^3. The calculated electron temperature, with $T_e = T_v$, is for this case 1,900°K (or 0.25 ev). When these values are substituted into equation (65) the result is

$$\lambda_D = 9 \times 10^{-4} \text{ cm} .$$

From Figure 18 it can be seen that the mean free path of electrons with an energy of 0.25 ev is

$$\ell_e = 4 \times 10^{-2} \text{ cm} .$$

Thus, the Debye length is very much smaller than the electron mean free path, and consequently electron diffusion need not be considered.

Ambipolar diffusion is limited by the ion-diffusion process since each diffusing electron must be accompanied by a diffusing ion. A simple examination of the ion-diffusion coefficient will show that ion diffusion is negligible in the 50-microsecond period under study. The diffusion coefficient is given in simple kinetic theory by the expression

$$D = \ell_m \bar{v}_m / 3 . \tag{66}$$

When the values of ℓ_m and $\bar{v}_m$ corresponding to 1.0 mm pressure and 295°K (listed previously) are substituted, the result is

$$D = 106 \text{ cm}^2/\text{sec} .$$

The product of the diffusion coefficient and the time of interest will give the number of ions diffusing through a unit area per unit concentration gradient. In the case being considered, this product is

$$D\tau = (106 \text{ cm}^2/\text{sec}) \ (50 \times 10^{-6} \text{ sec}) = 0.053 \text{ cm}^2 .$$

This value is a measure of the relative change in ion-concentration gradient due to diffusion during the 50-microsecond time of interest.

It is seen to be insignificant compared with the 100-fold change in ion-concentration gradient due to recombination during the same interval. When the pressure is reduced to 0.1 mm, the product $D\tau$ becomes 0.53 cm^2 and could be considered significant if the recombination rate were not so high. It is possible that at low pressures in gases other than nitrogen, ion diffusion could become a significant factor.

Thermal Expansion - The problem of thermal expansion of the spark-heated column of gas will be approached from a point of view of studying the prevention of excessive heating rather than one of studying the effects of thermal expansion once excessive heating has occurred. The feasibility of this procedure will be demonstrated by the small values of computed rotational and translational temperature increase discussed in the following paragraphs.

A comparison of the computed increases in rotational and translational temperature at the spark centerline for each of the three spark energies is shown in Figure 29. All computations are for 1.0 mm pressure without a magnetic field. A striking feature of Figure 29 is the continued increase in temperature exhibited in each case after the spark has terminated. The energy represented by this increase comes from two sources, ionization energy and vibrational energy. The ionization energy is transferred to molecular translation and rotation via the dissociative-recombination process; the vibrational energy is transferred to translation and rotation via electron collisions. De-excitation of vibration directly through molecule-molecule collisions has not been considered because of its relatively slow rate.

The computed final temperature increase is 1.9°K for the 0.05-joule spark, 11.2°K for the 0.5-joule spark, and 83.3°K for the 5.0-joule spark. These values represent temperature increases of 0.6%, 3.8%, and 28% over the initial temperature of 295°K. The first two values would not cause an appreciable expansion of the spark-heated column of gas, but the third probably would. If the static temperature were reduced significantly, the increase of 11.2°K due to the spark in the second case could cause an appreciable expansion, and it might then by desirable to keep the spark energy correspondingly lower.

In reality the situation with the 5.0-joule spark would be somewhat worse than indicated by the computed final temperature increase. In this case a final vibrational temperature of 9600°K was calculated, which means that an appreciable degree of dissociation could be expected. The effect of the dissociation would be to cause the column to expand, much in the same manner as a temperature increase, because of the resulting increase in the particle density. Also, the computed temperatures should be treated with suspicion in this case because the gas in the spark column is obviously disturbed by the spark process, in contradiction to the original assumption. In all other cases, the disturbance is slight.

Equilibrium between the translational and rotational temperatures is seen in Figure 29 to be established within about two microseconds of the termination of the spark process. It appears, therefore, that this particular departure from equilibrium is of no consequence except for its effect on temperature measurements made during the spark lifetime.

8. SIMPLIFIED COMPUTATION OF ELECTRON DENSITY AND MEAN ENERGY

The results presented in the previous chapter show that the computation technique adequately describes the spark process, consequently the electron energy and density can be computed if the current-time relationship is known. Unfortunately, the computations do not lend themselves to manual calculation because of the large number of time intervals that must be utilized in the integration of equation (21). It appears that a good approximation to the computed electron density can still be obtained when certain simplifying assumptions are made, if the spark luminosity is known as a function of time and the integrated intensity is also available. This procedure permits a significant reduction in the amount of effort required to compute the final electron-density profile and the mean electron energy during the mid-portion of the spark duration. It is not meant to replace the more complete set of computations discussed in the two previous chapters; it is intended rather to show how an approximate value for electron density can be computed from luminosity measurements. The details are given in the following paragraphs.

As noted earlier, the maximum current can be computed from an observation of spark luminosity as a function of time. When the area under the luminosity-time trace is equated to the initial charge on the

energy-storage capacitor, the constant of proportionality between luminosity and current can be obtained, and the peak current can be readily found. The validity of this procedure was shown in Figure 21, where computed luminosity and current were plotted as functions of time and shown to have similar behavior.

The current density at the moment of peak current can be found to a good approximation if the current-density profile at that moment is assumed to be identical to the integrated intensity profile. A comparison of computed curves for the two profiles is shown in Figure 30 for the 0.5-joule spark at 1.0 mm pressure. It is seen that the relative agreement between the two profiles here is virtually as good as the agreement between the measured and computed integrated intensity profiles shown in Figure 20. Absolute values can be assigned to the current-density profile at peak current if the peak current is set equal to the integral of the corresponding current density over the spark radius, in the manner of equation (14).

When the electron density is a maximum, equation (20), the equation for the rate of change of electron density, can be written as

$$\frac{dN_e(r,t)}{dt} = n_i - n_r = 0,$$

which states that the ionizing collision and recombination collision rates are equal. From this, N_e can be found with the substitution of equations (18) and (19) for n_i and n_r. The final result is as follows:

$$N_e(r,t) = 0.145\, N_m\, \epsilon \left[e^{-(27.3/\epsilon)} + 0.76\, e^{-(43.5/\epsilon)} \right] . \qquad (67)$$

Before we can solve this, a second relationship between N_e and ϵ must be established. This can be done if it is assumed that the maximum electron density occurs when the current is at its peak. The validity of such an assumption can be seen from an examination of Figure 31, where computed electron densities at three different radii are plotted versus time. Although the peak values occur a short time after the peak current, the change in electron density during this time is small and the assumption appears valid.

The second equation for N_e and ϵ is obtained from the current-density profile through equation (13):

$$J(r) = W(r)\, N_e(r)\, q_e, \qquad (68)$$

where $J(r)$ is found from the measured integrated intensity profile in the manner discussed above, and the relationship between ϵ and W is as given by Figure 18. In this manner the peak electron density can be computed if equations (67) and (68) are solved by iteration at all values of radius. Since the electron concentration changes little during the remainder of the spark, the values at spark termination can be assumed equal to the peak values. The value of ϵ obtained will be representative of the electron energy in the middle portion of the spark duration, but it cannot be used to infer values at other times.

Electron density in the decaying plasma is then found from equation (64). An approximate value of 0.25 ev can be used for ϵ since equation (64) is not very sensitive to ϵ. In this manner, electron-density profiles similar to those shown in Figure 28(b) can be obtained with relative ease.

9. DETECTION OF THE SPARK-HEATED COLUMN

Even though the spark and decaying-plasma processes appear to be reasonably well understood as a result of the studies presented in the previous chapters, few conclusions about the accuracy and limitations of flow-velocity measurements can be made until the methods of detecting the location of spark-heated columns are likewise well understood. In the following paragraphs, the properties of the spark-heated column that allow detection will be examined. The methods of detection will also be discussed, but with less emphasis.

9.1. Discussion of Profile Shapes

Profiles of vibrational temperature, electron density, integrated intensity, and degree of dissociation, all corresponding to the time of termination of the spark, are shown in Figure 32(a) for the 0.5-joule spark at 1.0 mm pressure. It is seen that the profiles progress from flattest to most peaked in the order listed above. Rotational- and translational-temperature profiles are not considered because there is no practical method of measuring these temperatures after the spark terminates.

Profiles of the four quantities listed above are also shown in Figure 32(b) for a time of 50 microseconds after the start of the spark. During the 49.2 microsecond period between the two sets of profiles, the electron density has been drastically reduced (Figure 28) and its profile shape has been flattened to the point that it is the flattest in the figure. The dissociation profile has been flattened somewhat less, and the vibrational-temperature and integrated intensity profiles are unchanged.

The shapes of the profiles shown in Figure 32(b) have a direct bearing on the accuracy with which the center of the spark-heated column can be located. This, in turn, has a direct effect on the accuracy of any velocity measurements that might be made from a study of the column motion. In this discussion we shall assume that the center of the spark-heated column can be located with a measuring uncertainty equal to 20% of the diameter of the column at the point where the detected quantity is 80% of its maximum value. With this assumption, an absolute uncertainty of measurement can be assigned, on the basis of the shape of the profile detected, to any measuring scheme.

9.2. Detection by Electron Density

Several methods of detecting the spark-heated column have been proposed based on electron density. These include the use of Langmuir probes, microwave transmission, or a second spark. A Langmuir probe can be used to obtain a direct measurement of electron density, so in

this case the center of the spark-heated column can be located after 50 microseconds with an uncertainty of measurement of 0.7 cm. The uncertanty of measurement obtained with microwave transmission will not be discussed since it is dependent on the geometry of the measuring apparatus.

When a second spark is used to detect the location of the column, the process is somewhat more complex than with a Langmuir probe. As in the case of the first spark, we are confronted with the basic problem of computing the spark characterisitics. Of primary interest is the luminous intensity, which can be computed from the equations already developed in Chapter 5. The electric field shape (equation (15)) and the initial electron concentration, however, will be different from those used with the first spark.

Rail electrodes such as those used by Kyser (1964) can be expected to produce an electric field that has a uniform strength over a large distance in the plane of the electrodes. The field strength will not be uniform in a plane normal to this, but it will decrease much less rapidly with distance than given by equation (15). For practical purposes, therefore, a uniform electric field should be a good approximation of the actual field shape. The approximation is particularly good when the second spark is viewed normal to the plane of the electrodes, since in this case the observed profile is influenced very little by the non-uniformity in electric field strength mentioned above. On the basis of these considerations, a uniform electric field strength was used in the computations.

The initial electron concentration for the second spark is taken as the electron concentration in the decaying plasma from the first

spark after 50 microseconds. The case chosen for computation was the 0.5-joule spark at 1.0 mm pressure. The initial electron density is then given by the appropriate curve in Figure 28(b).

The computed integrated intensity profile for the second spark is shown in Figure 33. Also shown in the figure are the electron-density profiles before the second spark, at termination of the spark (0.8 microsecond), and at 50 microseconds. The first two electron-density profiles are virtually identical, indicating that electron density remained sufficiently low during the spark to prevent the profiles from being distorted by recombination. As a consequence, the integrated intensity profile is identical to the electron-density profile. The reason for this is seen from an inspection of equation (23). The integrated profile is given to a good approximation by the integration of equation (23) over the spark duration, because almost all of the excited emitters undergo transitions during this period. In a uniform electric field, ϵ will be uniform and n_x will have the same radial variation as N_e. If the electron-density profile is invariant with time during the spark, the integrated intensity profile will be identical to it.

From this discussion it can be concluded that the technique of striking a second spark through the spark-heated column is simply another method of measuring electron concentration. If the electric field strength is uniform, the integrated spark intensity will be directly proportional to the electron-density at the instant the second spark is struck. The measuring accuracy, therefore, can be expected to be the same as that achieved with a Langmuir probe. For the case under discussion, the uncertainty of measurement would therefore again be 0.7 cm.

In Figure 33 it is seen that the electron-density profile is extremely flat 50 microseconds after the second spark. This will preclude the use of third and subsequent sparks for more detailed measurements unless some contaminant is added to the gas to retard recombination.

9.3. Detection by Vibrational Temperature

Clouston et al. (1958) have suggested and Hurle and Russo (1964) have shown experimentally that the electron temperature tends to equilibrate with the molecular vibrational temperature. Therefore, an electron-temperature measuring technique such as the sodium-line-reversal method will permit vibrational temperature to be used to detect the spark-heated column. The line-reversal technique will give a direct measurement of temperature only if the gas in the light path is uniform, and this is not the case in the spark-heated column. Therefore, it is doubtful that the measuring uncertainty of 0.5 cm based on Figure 32(b) could be obtained. One further complication in the sodium-line-reversal technique is that the test gas in the wind tunnel would have to be seeded with sodium impurities. If such seeding were done, however, it is likely that the resulting decrease in the rate of recombination of ions and electrons would make it possible to obtain a better accuracy of measurement with electron-detection techniques, so the line-reversal technique might not then give the relatively better measuring accuracy suggested by Figure 32(b).

9.4. Detection by Degree of Dissociation

Each electron-ion recombination collision can be expected to produce two neutral atoms. Since the atoms recombine slowly, the degree of dissociation could be used to detect the location of the spark-heated column after a long period of time. During the time interval from termination of the spark to 50 microseconds after start of the spark, the dissociation profile becomes flattened as a consequence of the additional atoms produced by dissociative recombination of electrons and ions. This flattens the dissociation profile because the initial electron-density profile is relatively flat by comparison with the initial dissociation profile.

A method of detecting atom concentration is provided by the catalytic probe. Hoenig (1959) gives a discussion of such probes and an interpretation of the data. The most satisfactory probe of this type consists of two fine wires inserted in the flow, one catalytic and the other non-catalytic. The two wires are connected as parts of a Wheatstone bridge, so that only the difference in heat transfer to the two wires, due to recombination at the surface of the catalytic wire, is recorded. Although it is difficult to secure an absolute measurement of degree of dissociation, a relative measurement is easily obtained. For measuring relative dissociation profiles, this is all that is needed.

On the basis of the accuracy-of-measurement criterion discussed earlier, the degree-of-dissociation profile shown in Figure 32(b) corresponds to an uncertainty of measurement of 0.3 cm.

9.5. Detection by Residual Luminous Intensity

Once the spark is extinguished, no further radiation in the second-positive band system is emitted. A subsequent transition occurs, however, between the lower level of the second-positive system and a third level. This subsequent transition, called the first-positive band system, has a long upper-state lifetime (5 microseconds) so its intensity at any point is proportional to the integrated excitation-collision rate. As discussed earlier, the integrated excitation-collision rate has the same profile as the integrated intensity. The relative intensity profile of the residual radiation will remain unchanged during the 50-microsecond period of interest, but the absolute intensity will diminish drastically.

From this discussion it appears that the spark-heated column can be detected by means of a photomultiplier tube and a lens system focused on a point in the path of the column. Since the radiation from the first-positive system is in the near infrared, the photomultiplier tube should be near-infrared sensitive. Such a system should, on the basis of the criterion being used here and the integrated intensity profile in Figure 32(b), give an uncertainty of measurement of 0.3 cm.

10. CONCLUDING REMARKS

10.1. Accuracy of Velocity Measurements

The relative uncertainty in measurement of velocity is given by the sum of the uncertainty in measurement of the initial and final positions of the spark-heated column divided by the distance traveled. Because of the high precision of readily available time-measuring techniques, possible errors in time measurement are not considered to be a limiting factor. Errors in time measurement are not included in this analysis, therefore. The uncertainty of measurement of the iniital position can be found from the profiles in Figure 32(a) and the criterion discussed in the previous chapter. These uncertainties are, in order of decreasing uncertainty, for the various profiles,

a) vibrational temperature: 0.5 cm,

b) electron density: 0.3 cm,

c) integrated intensity: 0.3 cm,

d) degree of dissociation: 0.2 cm.

The uncertainties of measurement of the final position of the spark-heated column are, in order of decreasing uncertainty, from the previous chapter,

a) electron density: 0.7 cm,

b) vibrational temperature: 0.5 cm,

c) degree of dissociation: 0.3 cm,

d) residual luminous intensity: 0.3 cm.

These uncertainties in position can be converted into relative uncertainties in velocity if a characteristic travel distance is introduced. The electrode gap appears to be the best choice for the characteristic distance, since in equation (15) for electric field strength the radius appears only in the ratio of radius to electrode gap. Therefore, if the electrode gap were decreased by a factor of two, the electric field shape would be changed so that a specified value of $E(r)/E(0)$ would occur at one-half of the radius at which it occurred before the change. Since the various profiles, such as integrated intensity, electron density, etc., are strongly dependent on electric field shape, they would experience a similar change. A reduction in electrode gap by a factor of two would thus also reduce the position-measuring uncertainty by a factor of approximately two. In the following discussion the travel distance will therefore be taken equal to the electrode gap, which was 12.7 cm in the present studies. The results can readily be applied to cases having other values of electrode gap.

On the basis of the measuring uncertainties and travel distance given above, we can compute the relative velocity-measuring uncertainty associated with the instrumentation techniques discussed in the previous chapter.

Langmuir-Probe Technique - If a Langmuir probe is used to detect the initial and final position of the spark-heated column, the sum of the position-measuring uncertainties will be 1.0 cm, which will give an

expected velocity-measuring uncertainty of 8%. In practice, it would be difficult to achieve a value this low because the initial-position probe would have to be located a slight distance downstream of the spark location, and the ionization profile would deteriorate slightly during the time required to travel this distance. Additional uncertainty might also result from the effect of the flow disturbances caused by the presence of the probe.

Photographic Technique - If the initial position of the spark-heated column is obtained from a photograph of the spark and the final position from a photograph of a second spark, the expected velocity-measuring uncertainty will be 8%. The uncertainty is slightly less than with the Langmuir probe because the initial location of the spark-heated column is detected from the integrated intensity rather than the electron density. The two profiles are compared in Figure 32(a).

Sodium-Line-Reversal Technique - If the vibrational-temperature profile is used to detect the location of the column, a velocity-measuring uncertainty of 8% can, in principle, be obtained. As discussed in the previous chapter, it would in practice be difficult to realize an uncertainty this low.

Photomultiplier Technique - If the residual-intensity profile is used to detect the column location, a velocity-measuring uncertainty of 5% can be expected. Although the initial location must be downstream from the spark location, no decrease in accuracy will result because the residual-intensity profile does not deteriorate with time.

Catalytic-Probe Technique - If a catalytic probe is used to detect the position of the column, the expected uncertainty in velocity measurement will be 4%. This figure would again be difficult to achieve in practice as catalytic probes are subject to the same problems encountered with the Langmuir probe.

Methods of Improving Accuracy - As seen in Figure 20(b), a 655-gauss magnetic field parallel to the spark axis will cause an appreciable reduction in spark width. It is of interest to examine the effect of such a magnetic field on the uncertainty of velocity measurements made by the photographic technique and the photomultiplier technique. The other detection techniques will not be discussed because they appear to be less promising. With a 655-gauss magnetic field, the computed uncertainty of locating the position of the spark by intensity measurements is 0.05 cm. When the same spark is detected after 50 microseconds by a second spark, which gives an integrated intensity proportional to the electron density profile in Figure 28(b), the uncertainty is 0.18 cm. Therefore, the uncertainty of velocity measurement is 2% when the photographic technique is used and 1% when the photomultiplier technique is used. These values represent a reduction in uncertainty by a factor of 4 and 5, respectively, as a result of the applied magnetic field. It appears, then, that an externally applied magnetic field is an effective means of reducing velocity-measuring uncertainty at pressures of 1.0 mm and below. At higher pressures, owing to the reduced effectiveness of the magnetic field, it might be more profitable to reduce the electrode gap while the measuring distance is held fixed. When a

magnetic field is used to confine the spark, the extent to which the measuring uncertainty could be reduced by a reduction in electrode gap is unknown because there is no theoretical basis for the electric-field-shape relationship given in equation (46).

10.2. Discussion of Measurements Made in a Hypersonic Stream

The validity of the estimates of measuring uncertainty developed in the previous section can be ascertained by an examination of measurements made in a hypersonic stream. Only measurements made with the photographic technique and the photomultiplier technique will be discussed.

Photographic Technique - Velocity measurements made in the empty test section of the Stanford spark-heated wind tunnel are shown in Figures 34 to 37. The time between sparks was approximately 50 microseconds in all cases, and the test section densities corresponded to the density in the static chamber at 1.0 mm pressure.

A photograph of three sparks struck across a 10.2-cm spark gap is shown in Figure 34. Although the definition of the third spark is poorer than that of the second spark, it is apparent that the spark is better defined than was predicted. With travel distances of just under the length of the electrode gap used in the experiments, the uncertainty of velocity measurement should be about 8% when the first two sparks are used and several times greater than this value when the second and third sparks are used. An indication of the actual uncertainty can be obtained

from the data scatter in Figure 35. In the figure, v_{12} denotes the velocity obtained from the displacement of the second spark relative to the first, v_{13} the velocity obtained from the first and third sparks, and v_{23} the velocity obtained from the second and third sparks. If it is assumed that the actual flow velocity was uniform and equal to the average of the 15 data points in the figure, then all of the data fall within an uncertainty band of $\pm$ 5%.

This greater-than-expected accuracy can be attributed to contaminants in the flow reducing the rapid ion-electron recombination rate. Further evidence for this assumption comes from experiments supported by the National Aeronautics and Space Administration under Contract NAS-2-3303 and conducted by the author in the one-foot hypersonic shock tunnel at Ames Research Center, when it proved difficult to strike a second spark through the ionized column after only 30 microseconds. The test gas in the Ames facility is extremely pure by contrast to the high contamination level in the Stanford tunnel.

The effectiveness of a magnetic field in reducing the uncertainty of measurement can be seen in Figures 36 and 37. The spark images are better defined in Figure 36 than in Figure 34, and the apparent data scatter is somewhat reduced. If the flow is assumed to be uniform with a velocity given by the average of the data points in Figure 37, all of the data fall within a band of $\pm$ 1%. This is approximately the expected improvement over the measurements made without a magnetic field.

A microphotometer trace of a photograph of two sparks in a hypersonic stream is shown in Figure 38. The photograph was made during the experiments in the one-foot hypersonic shock tunnel at the Ames Research Center.

The electrode gap was 10 cm and the travel of the spark-heated column was 17 cm. The uncertainty in locating the center of the column, expected on the basis of the criterion discussed in the previous chapter, is indicated by the bars in the figure. This uncertainty corresponds to a velocity-measuring uncertainty of $3\frac{1}{2}\%$. A direct comparison between this value and the uncertainty of measurement based on Figure 32 can not be made because the spark energy and static pressure were not the same as in Figure 38. The intensity profile of the second spark is virtually as peaked as the profile of the first spark. This would not be expected in view of the profile-flattening trend shown in Figure 32, and probably is a result of driver-gas contamination in the flow.

Photomultiplier Technique - During the experiments conducted at the Ames Research Center, the residual luminosity of the spark column was examined with the photomultiplier arrangement shown in Figure 39. The lens was adjusted so that a spot 9.2 cm downstream of the point midway between the electrodes was focused on the aperture. Figure 40 shows the output of the photomultiplier tube as recorded by an oscilloscope. The excursion in the center of the trace represents the passage of the luminous column past the focal point of the system. The excursions on each end of the trace represent reflected light from the spark used to generate the column and from a second spark used to detect it at a later time. Figure 41 is the microphotometer record obtained from a photograph of the spark used to generate the column. The flow velocity computed from shock-velocity measurements was 0.42 cm/μs, so that the time base of 5 μs/cm, or 5μs per major division, in Figure 40 is equivalent to 2.1 cm

per major division. With this correspondence between time in Figure 40 and distance indicated in Figure 41, a remarkable similarity is seen to exist between the two profiles. The photographed profile is slightly wider, however, probably, as a result of film nonlinearity and the displacement, due to flow velocity, of the spark column during the spark duration. In spite of this, the implication is that the residual intensity profile is very nearly the same shape as the integrated intensity profile, as was discussed in Section 9.5.

10.3. Resume

The structure of spark columns used for velocity measurement in a hypersonic stream has been studied experimentally and analytically. The objective was the evaluation of effects of thermal expansion, electron diffusion, and electron-ion recombination on the accuracy of measurement. Nitrogen was the only gas considered in the study.

A crucial assumption in the analysis was that the gas in the spark column is little affected by the spark. The validity of this assumption can be seen from an examination of the computed ionization level and temperature of the spark at time of termination. For the 0.5-joule spark at 1.0 mm pressure these are as follows: ionization level = 0.02%, $\Delta T_R = 7^\circ K$, $\Delta T_T = 3^\circ K$, and $T_v = 1900^\circ K$. At this vibrational temperature, less than 20% of the molecules are excited vibrationally, so all four values are seen to satisfy the restriction.

The results of the analysis show that thermal expansion and electron diffusion will not necessarily affect the measuring accuracy, but electron-ion recombination will adversely affect the accuracy of any measurement that depends on residual ionization of the spark-heated column of gas. Consequently, several methods of measurement not depending on ionization were investigated.

It was found that velocity-measuring techniques depending on residual luminosity or degree of dissociation will give slightly better accuracy of measurement than those depending on residual ionization. With any of the techniques considered, it appears possible to measure velocity with an accuracy of about 2% by using either 1) a sufficiently large ratio of measuring distance ot electrode gap, or 2) a magnetic field for confining the spark. The validity of these results is demonstrated qualitatively by data obtained in a hypersonic stream.

Without further analysis these results cannot be applied to situations where gases other than nitrogen or air are used. This is a consequence of the importance of certain microscopic properties that are peculiar to each gas. If, for example, the gas were a monatomic gas, dissociation measurements would not be meaningful. If a radiative transition with a long lifetime did not occur, measurements that depend on residual luminosity could not be used. In a monatomic gas the electron-ion recombination rate is smaller than in nitrogen, because of the absence of dissociative recombination processes, so the accuracy of measurements that depend on ionization would probably be improved. In such a case, the most accurate methods of measurement would be those depending on residual ionization, which is the opposite of the results for nitrogen.

REFERENCES

ANDERSON, J. M., 1964, "Hall Effect and Electron Drift Velocity in the Plasma of the Positive Column," Physics and Fluids, Vol. 7, p. 1517.

BATES, D. R., 1950, "Dissociative Recombination," Physical Review, Vol. 78, p. 492.

BIALECKE, E. P. and DOUGAL, A. A., 1958, "Pressure and Temperature Variation of the Electron-Ion Recombination Coefficient in Nitrogen," Journal of Geophysical Research, Vol. 63, p. 539.

CLOUSTON, J. G., GAYDON, A. G., and GLASS, I. I., 1958, "Temperature Measurements of Shock Waves by the Spectrum-Line Reversal Method," Proceedings of the Royal Society (London), Series A, Vol. 248, p. 429.

CROMPTON, R. W. and SUTTON, D. J., 1952, "Diffusion of Slow Electrons in Nitrogen and Hydrogen," Proceedings of the Royal Society (London), Series A, Vol. 215, p. 467.

CUNNINGHAM, J. W. and DICKS, J. B., 1964, "A Microwave Method of Measuring Plasma Velocity," Proceedings of the Third Hypervelocity Techniques Symposium, Denver, March 1964.

FAIRE, A. C. and CHAMPION, A. C., 1959, "Measurements of Dissociative Recombination and Diffusion in Nitrogen at Low Pressures," Physical Review, Vol. 113, p. 1.

FULLER, W. H. Jr., 1965, Private Communication.

GERJUOY, E. and STEIN, S., 1955, "Rotational Excitation by Slow Electrons," Physical Review, Vol. 97, p. 1671.

GREENSPAN, M.,1959, "Rotational Relaxation in Nitrogen, Oxygen, and Air," Journal of the Acoustical Society of America, Vol. 31, p. 155.

HAAS, R., 1957, "Unterschunger iber den Energieverlust Langsamer Elektronen in Stickstoff," Z. Physick, Vol. 148, p. 177.

HERZBERG, G., 1950, Spectra of Diatomic Molecules, D. van Nostrand and Co., New York.

HERZFELD, K, F., and LITOVITZ, T. A., 1959, Absorption and Dispersion of Ultrasonic Waves, Academic Press, New York.

HOENIG, S. B., 1959, "Use of a Catalytic Probe for Detection of Dissociated Non-Equilibrium Flow," A.R.S. Journal, Vol. 29, p. 361.

HURLE, I. R., 1964, "On the Thermal Energy Transfer Between Free Electrons and Molecular Vibration," Journal of Chemical Physics, Vol. 41, p. 3592.

HURLE, I. R. and RUSSO, A. L., 1965, "Spectrum-Line Reversal Measurements of Free-Electron and Coupled N_2 Vibrational Temperatures in Expansion Flows," Journal of Chemical Physics, Vol. 43, p. 4434.

KARAMCHETI, K., VALI, W., KYSER, J. B., and RASMUSSEN, M. L., 1962, "Measurements of Pressure and Speed of Flow in a Spark-Heated Hypersonic Wind Tunnel," Arnold Engineering Development Center, AEDC-TRD-62-218.

KYSER, J. B., 1964, "Development of a Tracer-Spark Technique for the Study of Hypervelocity Flow Fields," Proceedings of the Third Hypervelocity Techniques Symposium, Denver, March 1964.

LONGSTROTH, G. O., 1934, "The Exictation of Band Systems by Electron Impact," Proceedings of the Royal Society (London), Series A, Vol. 146, p. 166.

MASSEY, H. S. W. and BURHOP, E. H. S., 1952, Electronic and Ionic Impact Phenomena, Oxford University Press, Oxford.

NEILSEN, R. A., 1936, "Absolute Values of the Electron Drift Velocity in Nitrogen, Helium, Neon, and Argon," Physical Review, Vol. 50, p. 950.

NICHOLLS, R. W., 1964, "Transition Probabilities of Aeronomically Important Spectra," Annales de Geophysique, Tome 20, p. 144.

RUDINGER, G., 1964, Comments on "Tracer-Spark Technique for Velocity Mapping of Hypersonic Flow Fields," AIAA Journal, Vol. 2, p. 1517.

SAMPSON, D. H., and MJOLSNESS, R. C., 1965, "Theory of Rotational Excitation of Homonuclear Diatomic Molecules by Slow Electrons. Application to N_2 and H_2," Physical Review, Vol. 140, p. 1466.

SAWYER, R. A., 1963, Experimental Spectroscopy, Dover Publications, Inc., New York.

SAYERS, J., 1956, Solar Eclipses and The Upper Atmosphere, Pergamon Press, Inc., New York.

SHULZ, C. J., 1959, "Measurement of Excitation of N_2, CO, and He by Electron Impact," Physical Review, Vol. 116, p. 1141.

TOWNSEND, J. S. and BAILEY, V. A., 1921, "The Motion of Electrons in Gases," Philosphical Magazine, Vol. 42, p. 873.

VINCENTI, W. G., and KRUGER, C. H., Jr., 1965, "Introduction to Physical Gas Dynamics, John Wiley and Sons, Inc., New York.

VON ENGLE, A., 1955, Ionized Gases, Oxford University Press, Oxford.

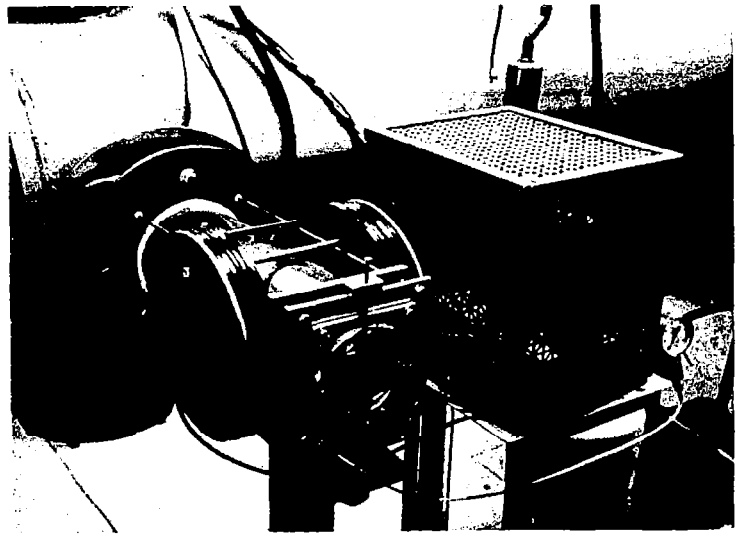

a) Static-Test Chamber and Spark Circuit

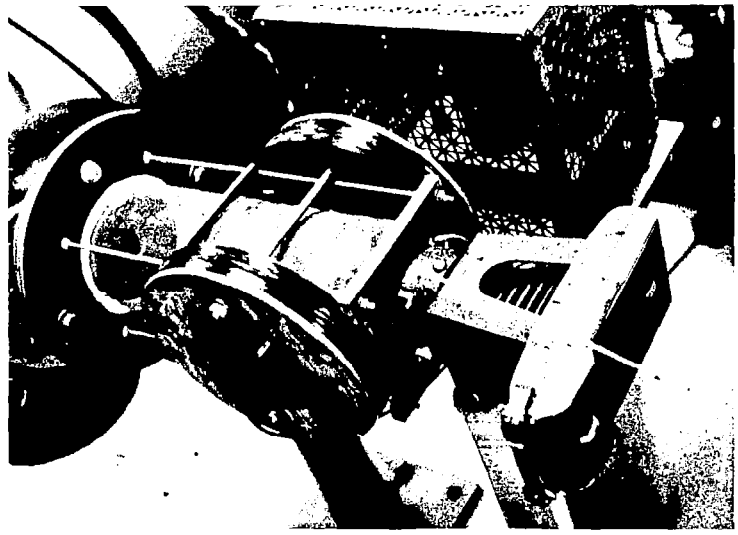

b) Camera Mounted on Static-Test Chamber

FIG. 1. PHOTOGRAPHS OF STATIC-TEST CHAMBER.

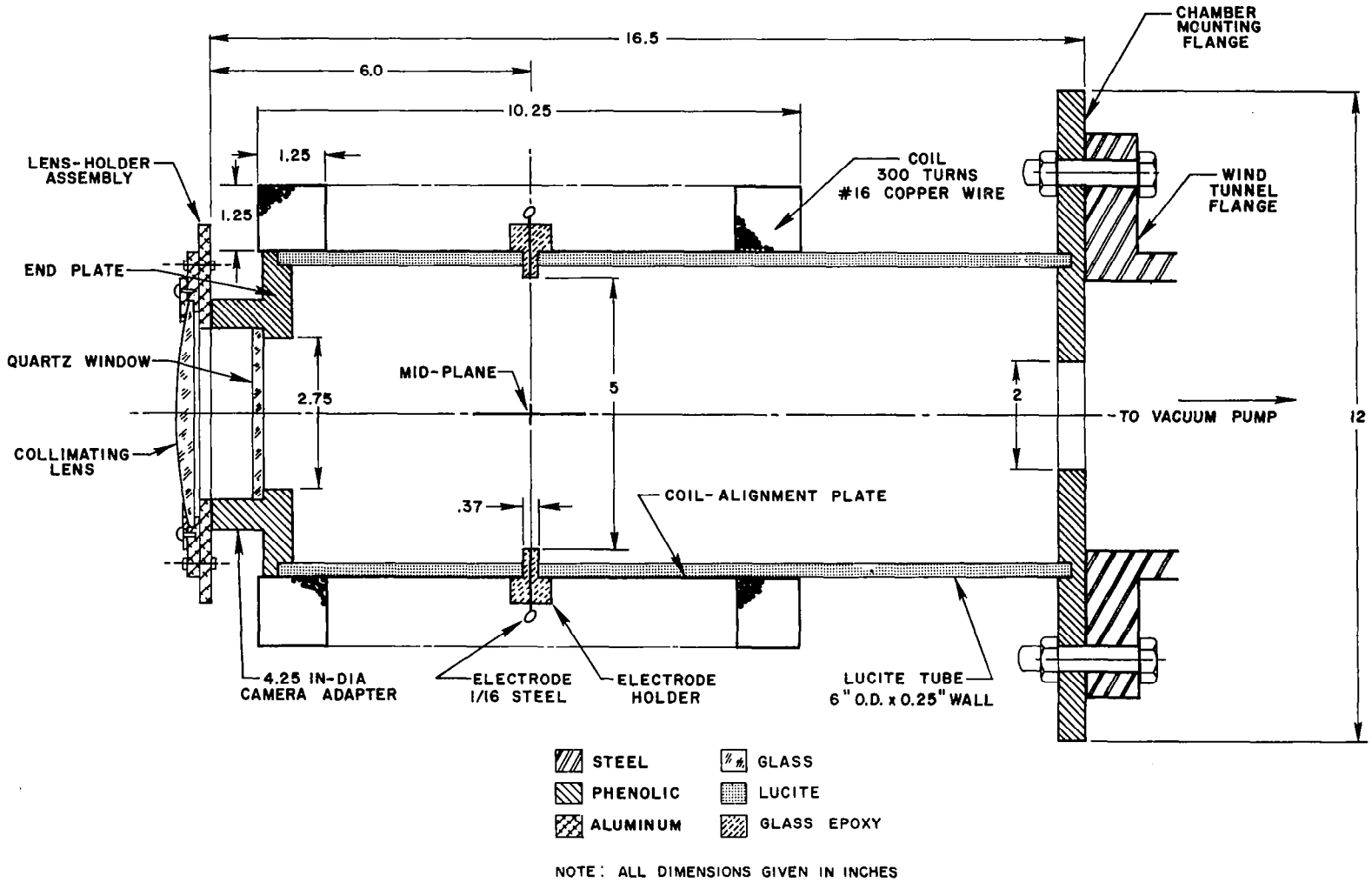

FIG. 2. SECTIONAL VIEW OF STATIC-TEST CHAMBER.

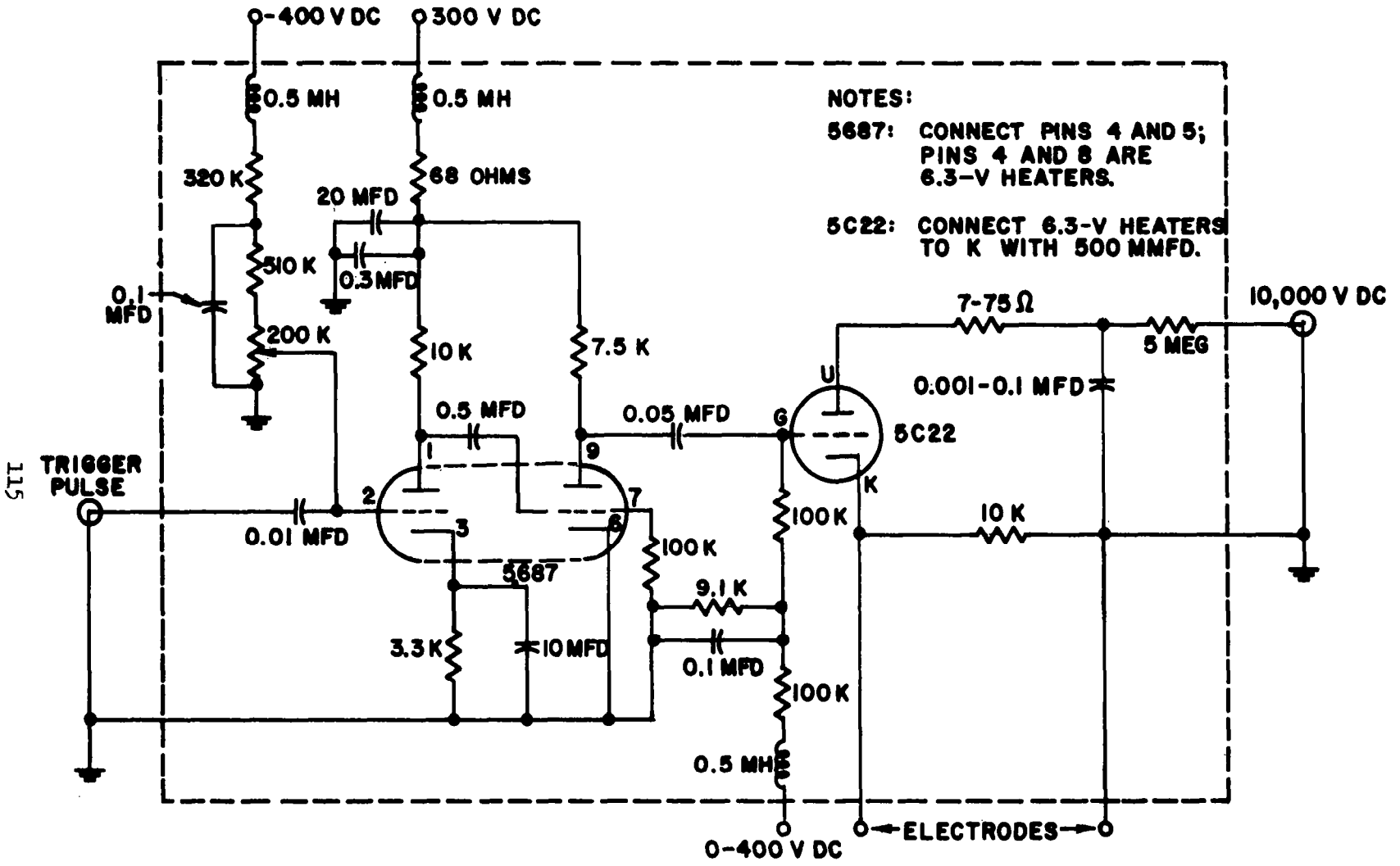

FIG. 3. DIAGRAM OF CIRCUIT USED TO PRODUCE SPARKS.

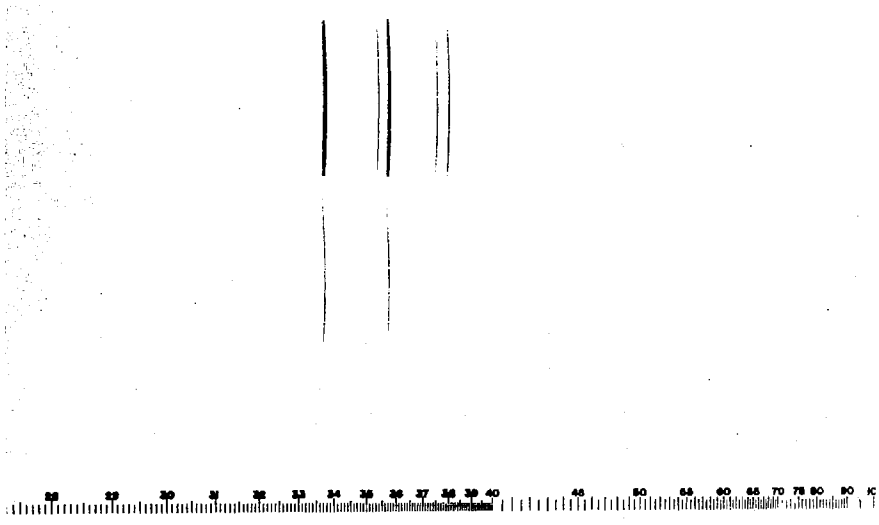

a) 0-Gauss Magnetic Field

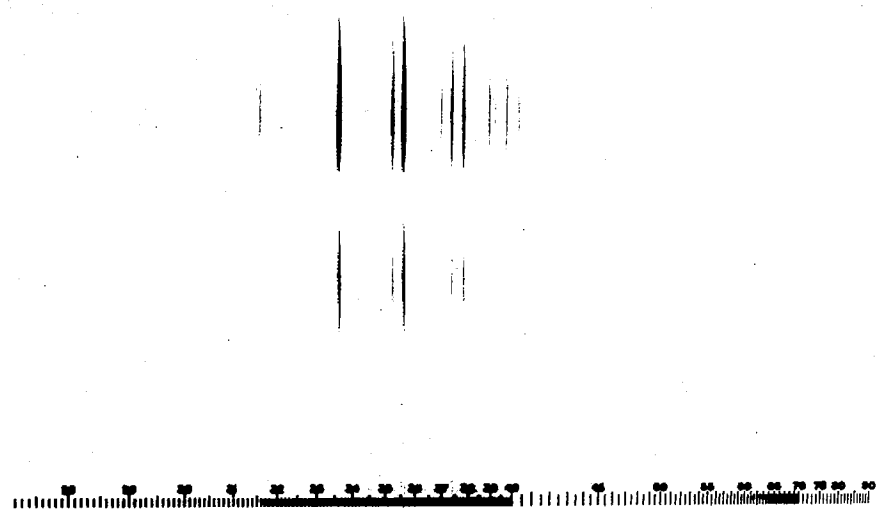

b) 655-Gauss Magnetic Field

FIG. 4. SPECTRA OF SPARKS IN NITROGEN.

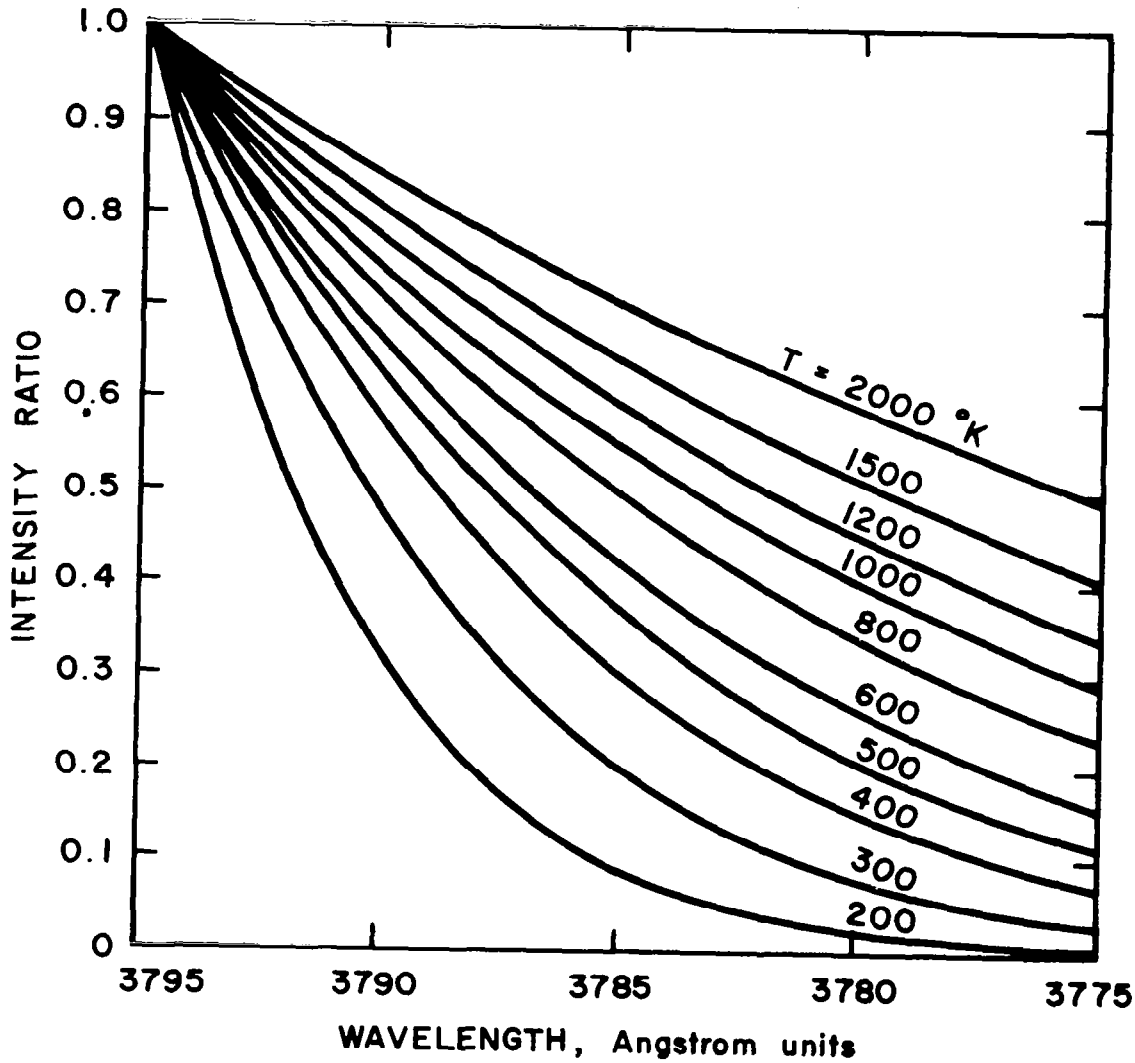

FIG. 5. EFFECT OF ROTATIONAL TEMPERATURE ON BAND-INTENSITY DISTRIBUTION.

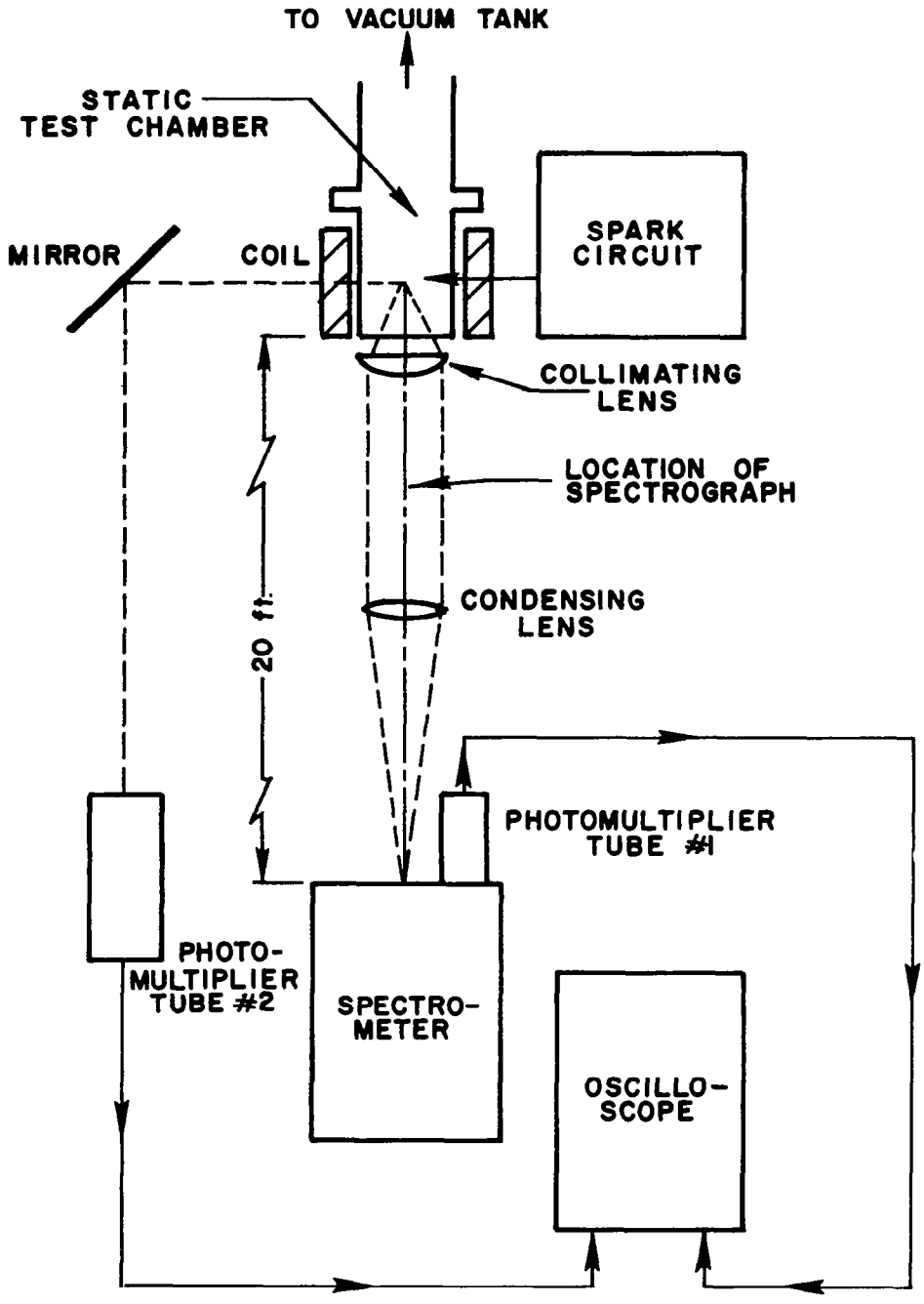

FIG. 6. APPARATUS FOR MAKING SPARK-TEMPERATURE MEASUREMENTS.

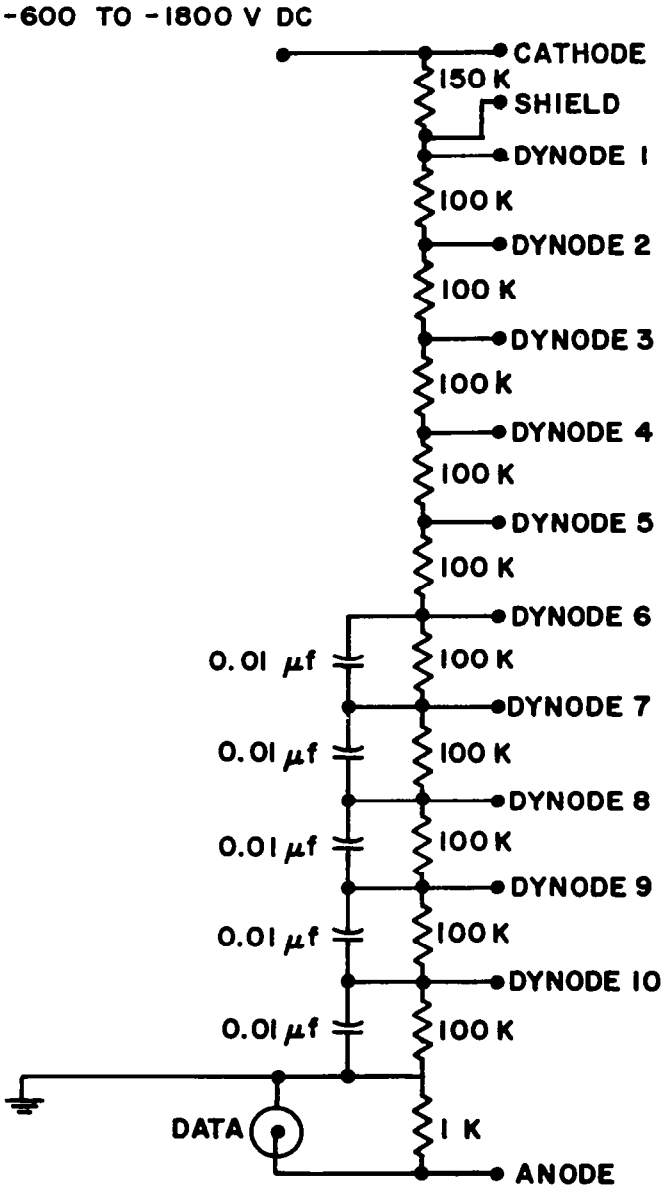

FIG. 7. PHOTOMULTIPLIER CIRCUIT.

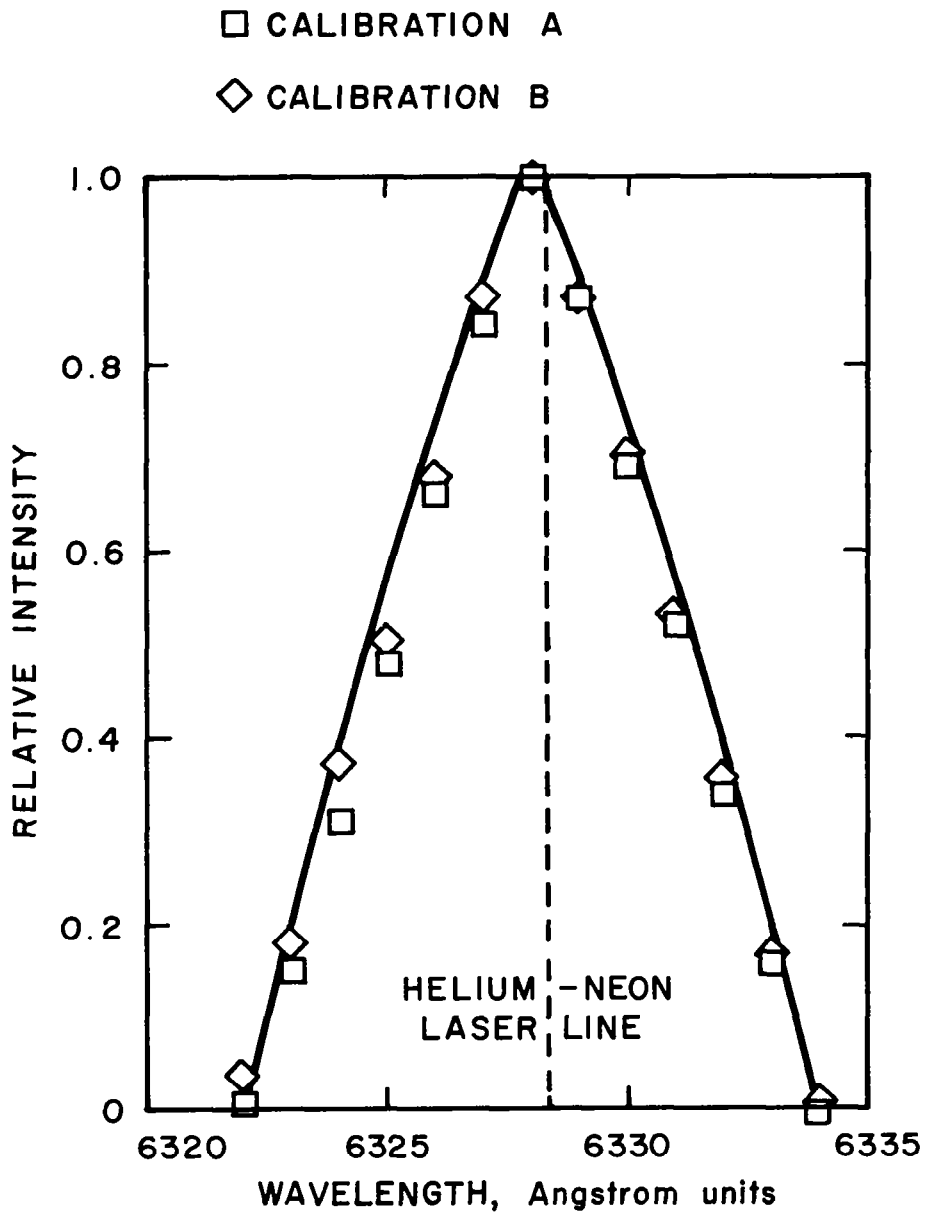

FIG. 8. INSTRUMENT-PROFILE CALIBRATION;
400μ SLIT WIDTH.

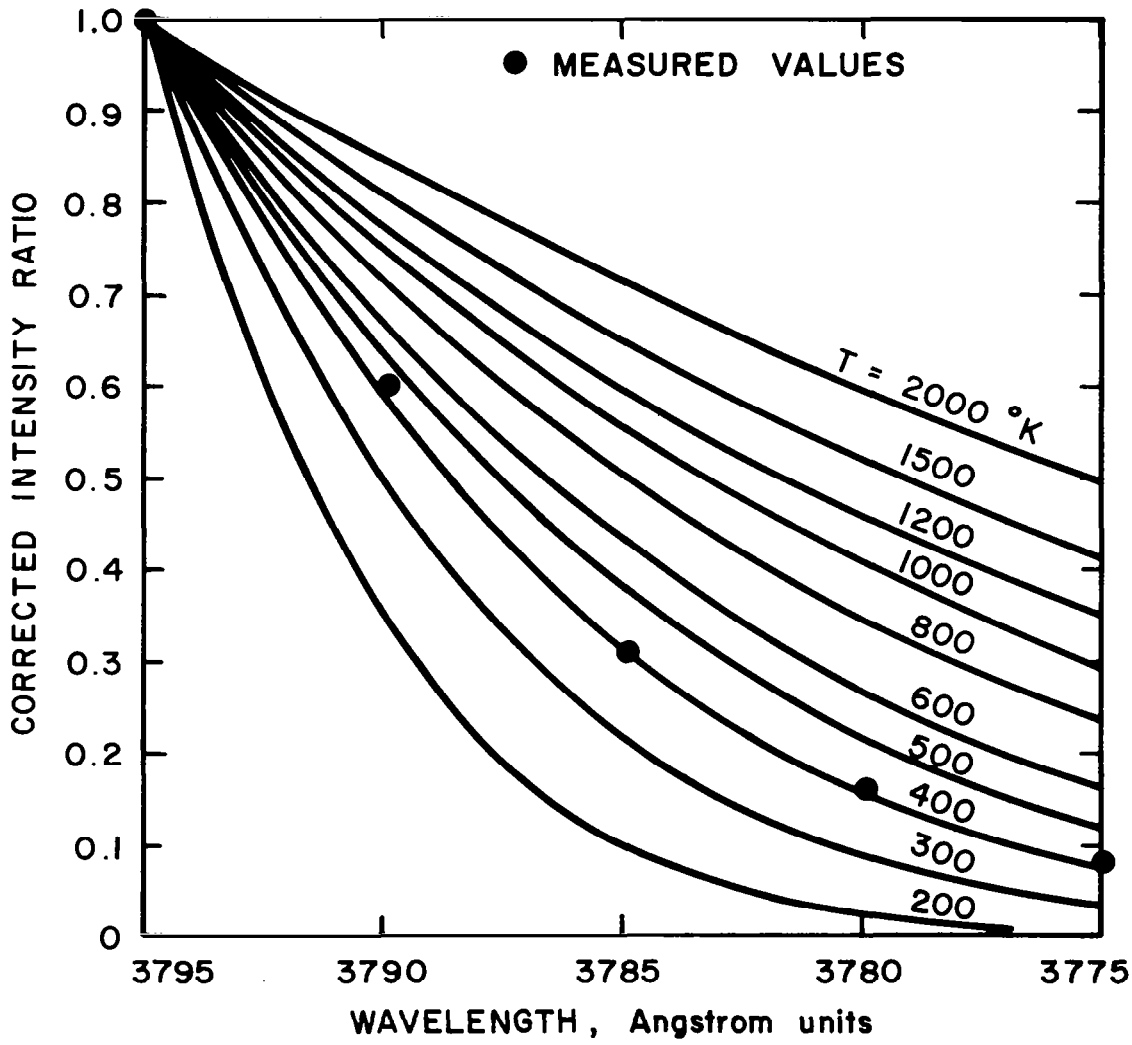

FIG. 9. CORRECTED BAND-INTENSITY DISTRIBUTION; 400μ SLIT WIDTH.

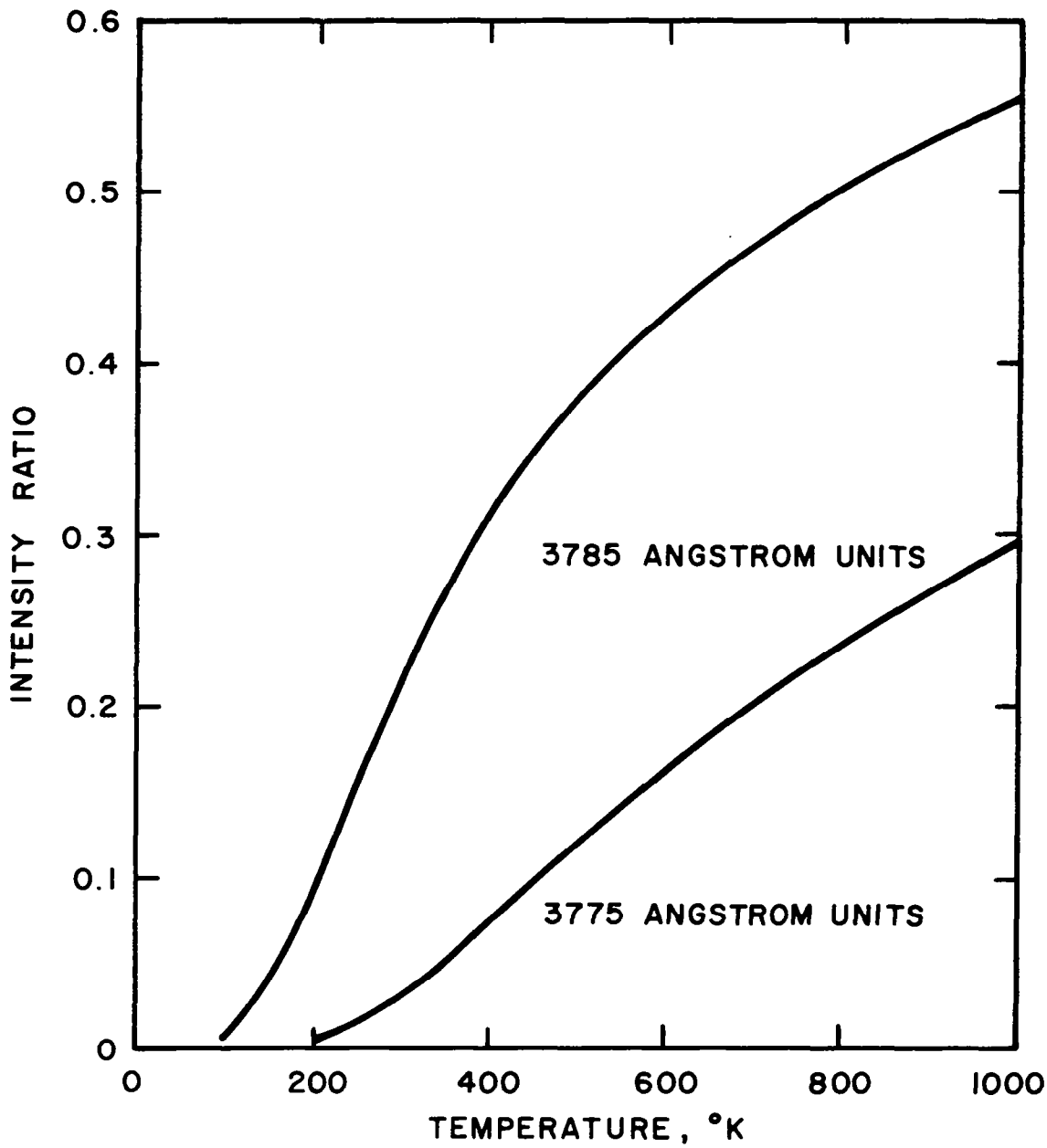

FIG. 10. INTENSITY RATIO VS TEMPERATURE;
400μ SLIT WIDTH.

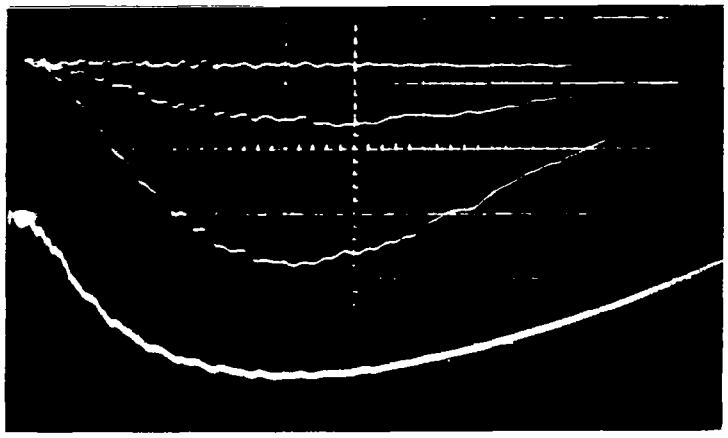

Upper Trace: Spectrometer Output, 0.02 V/cm
Lower Trace: Monitor
Time Base: 0.2μs/cm

a) 5.0-Joule Spark

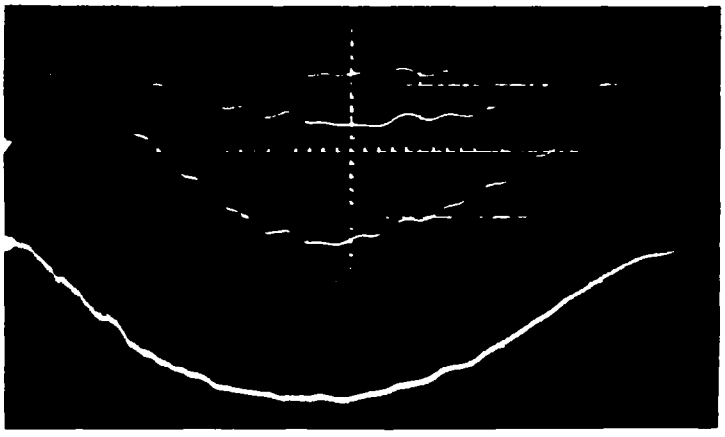

Upper Trace: Spectrometer Output, 0.02 V/cm
Lower Trace: Monitor
Time Base: 0.1μs/cm

b) 0.5-Joule Spark

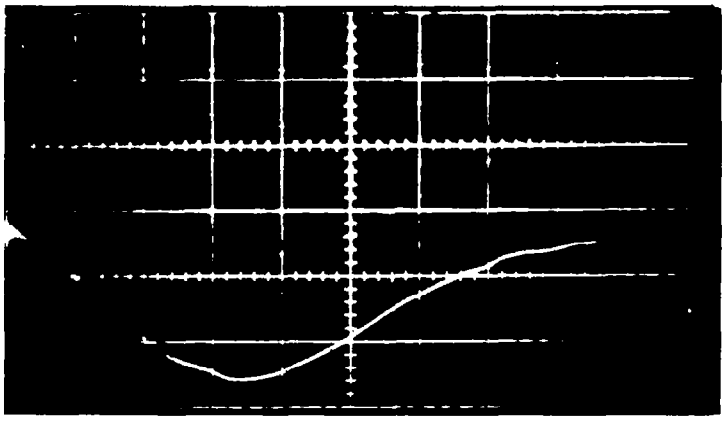

Upper Trace: Spectrometer Output, 0.02 V/cm
Lower Trace: Monitor
Time Base: 0.04μs/cm

c) 0.05-Joule Spark

FIG. 11. OSCILLOSCOPE TRACES OF SPECTROMETER OUTPUT.

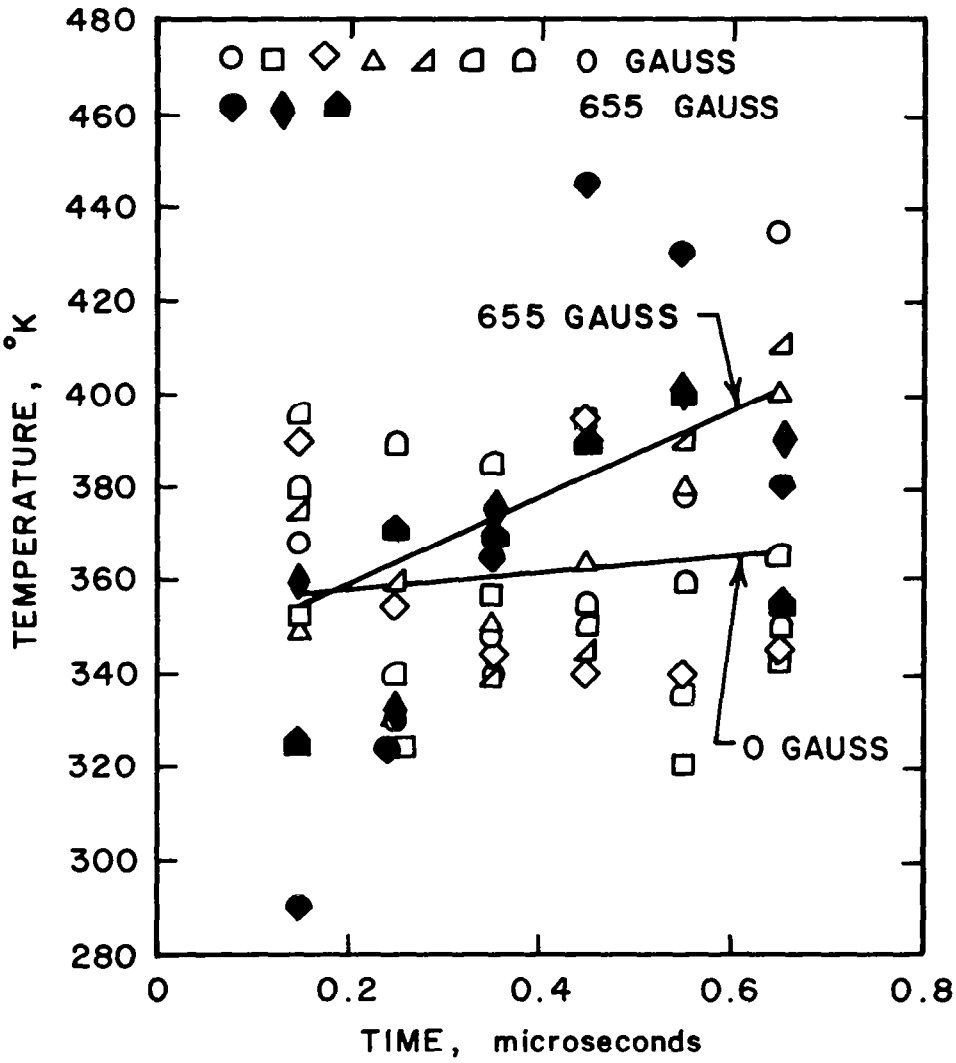

FIG. 12. TIME-RESOLVED CENTERLINE SPARK-TEMPERATURE MEASUREMENTS.

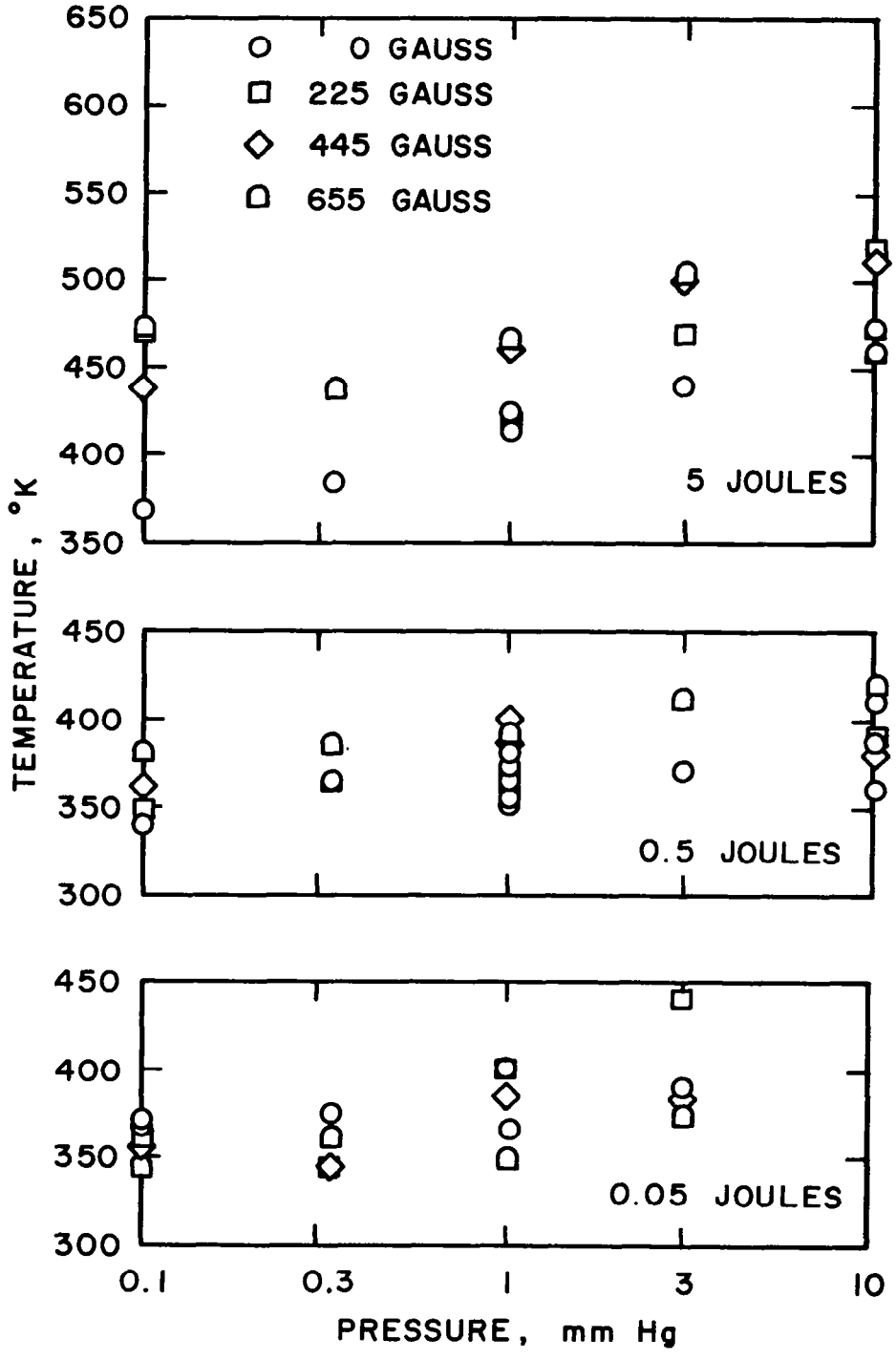

FIG. 13. AVERAGE CENTERLINE SPARK-TEMPERATURE MEASUREMENTS.

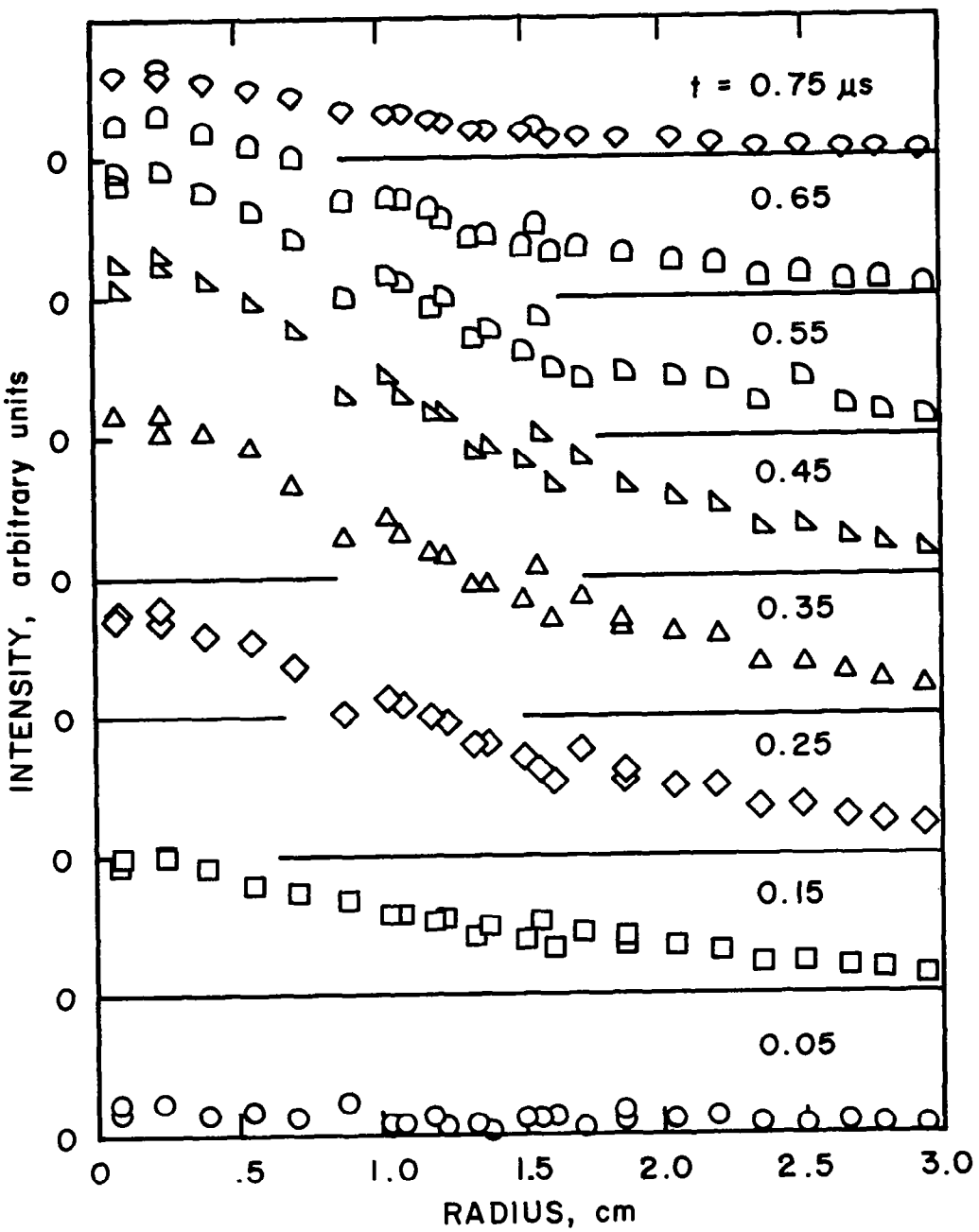

a) Without a Magnetic Field

FIG. 14. MEASURED TIME-RESOLVED INTENSITY PROFILES.

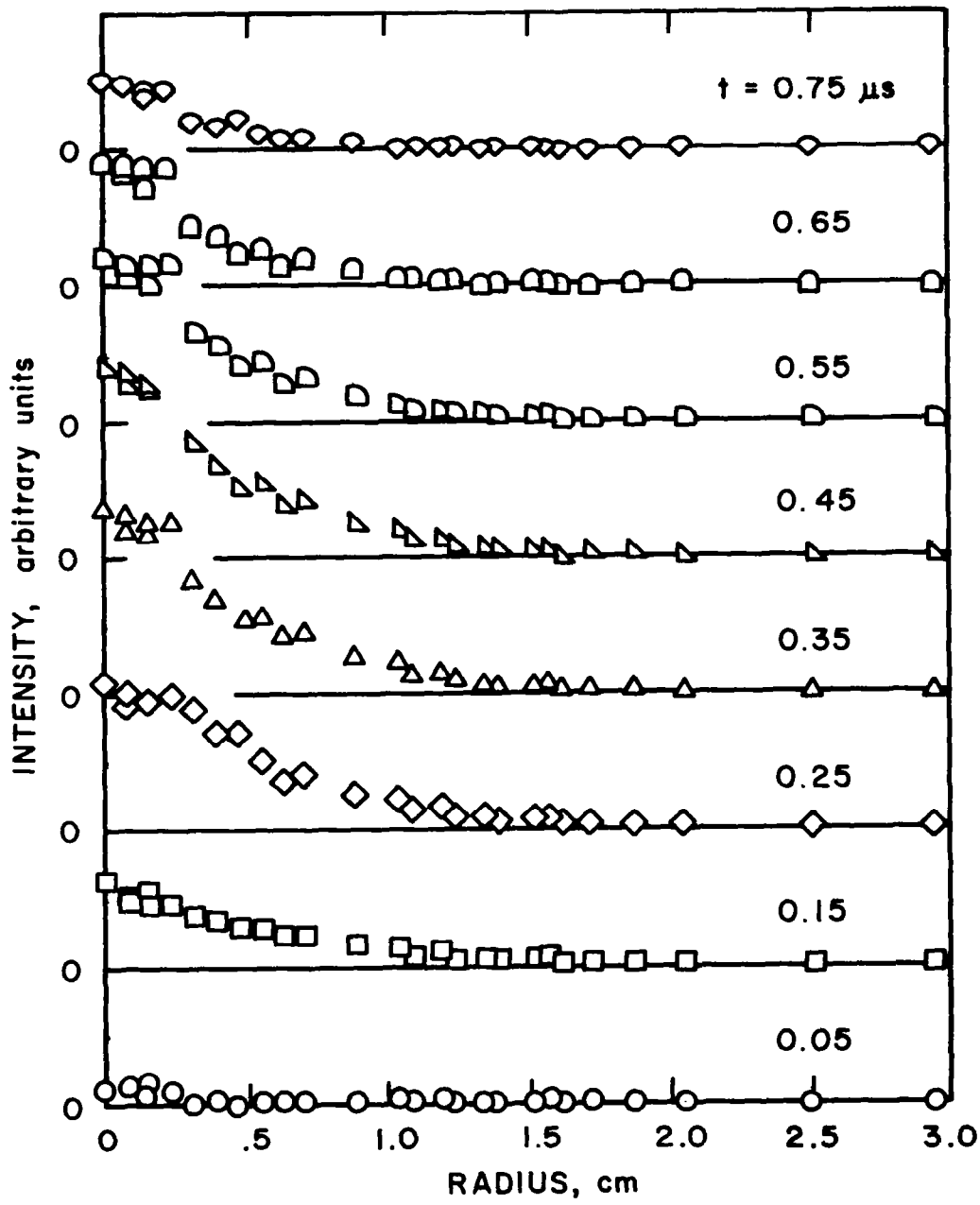

b) With a 655-Gauss Magnetic Field.

FIG. 14. CONCLUDED

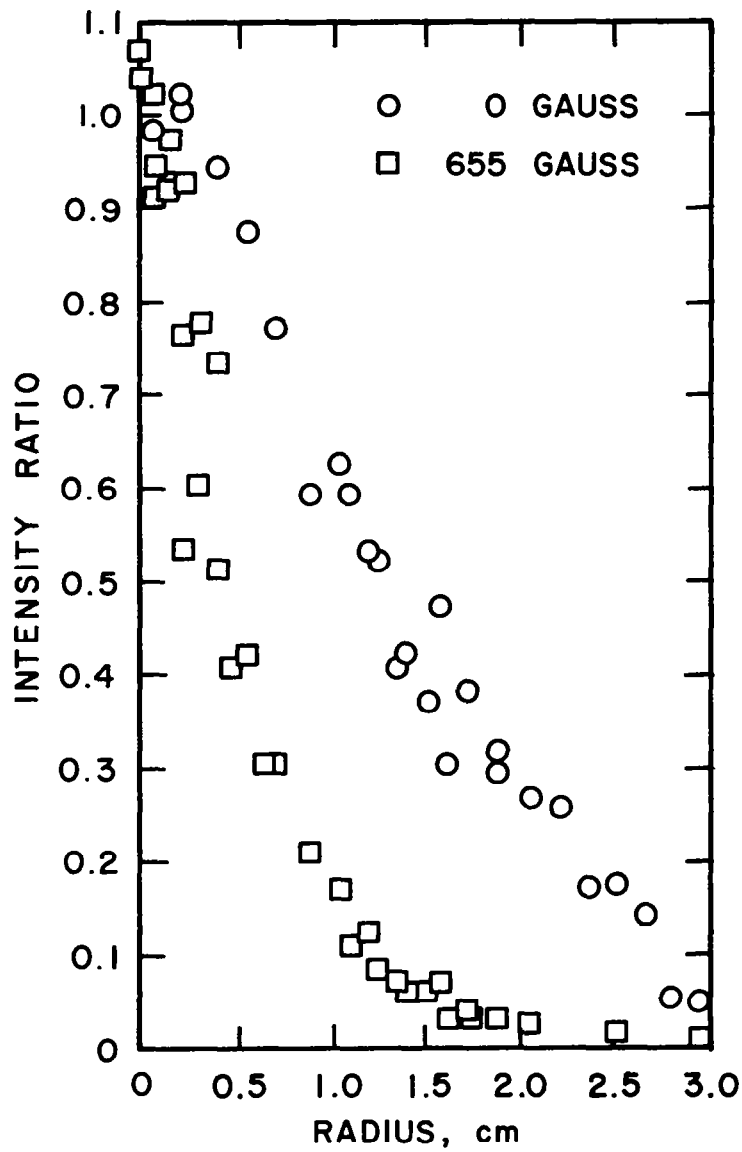

FIG. 15. MEASURED INTEGRATED INTENSITY PROFILES.

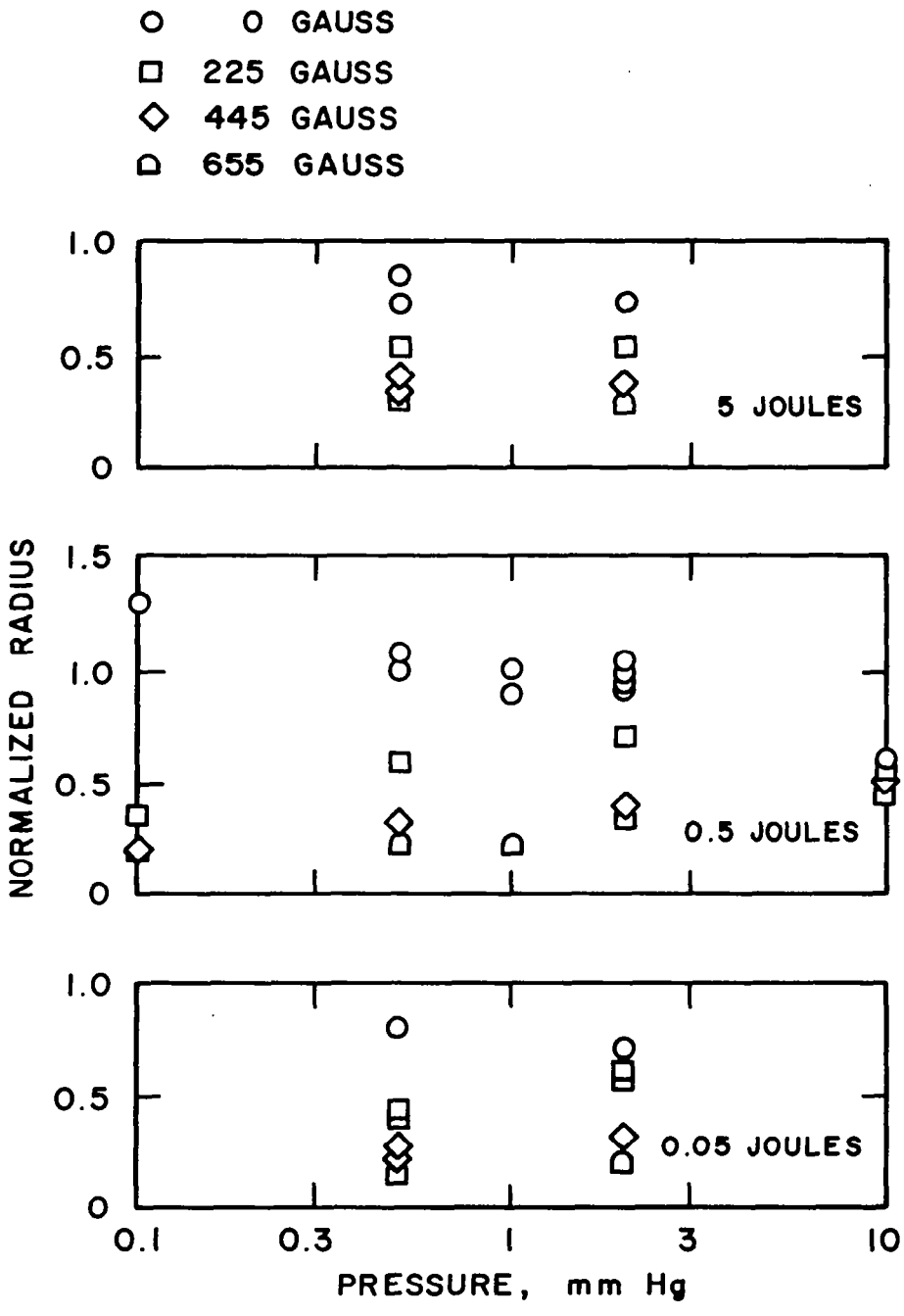

FIG. 16. NORMALIZED SPARK RADIUS.

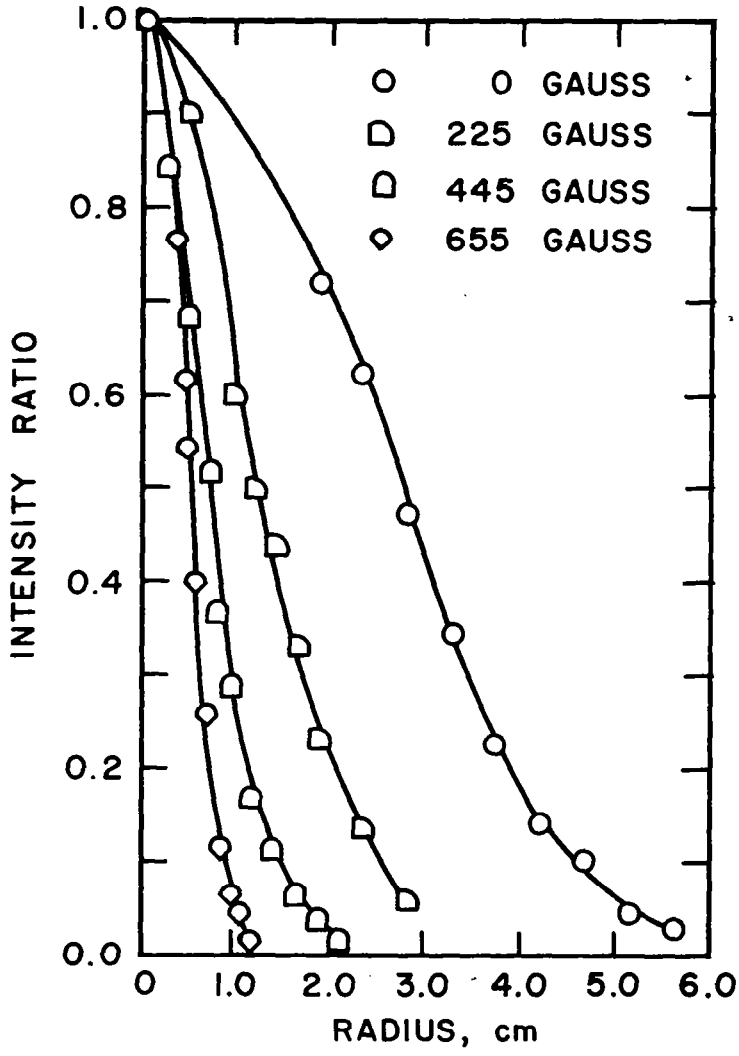

FIG. 17. SPARK-INTENSITY PROFILES OBTAINED FROM PHOTOGRAPHIC DATA.

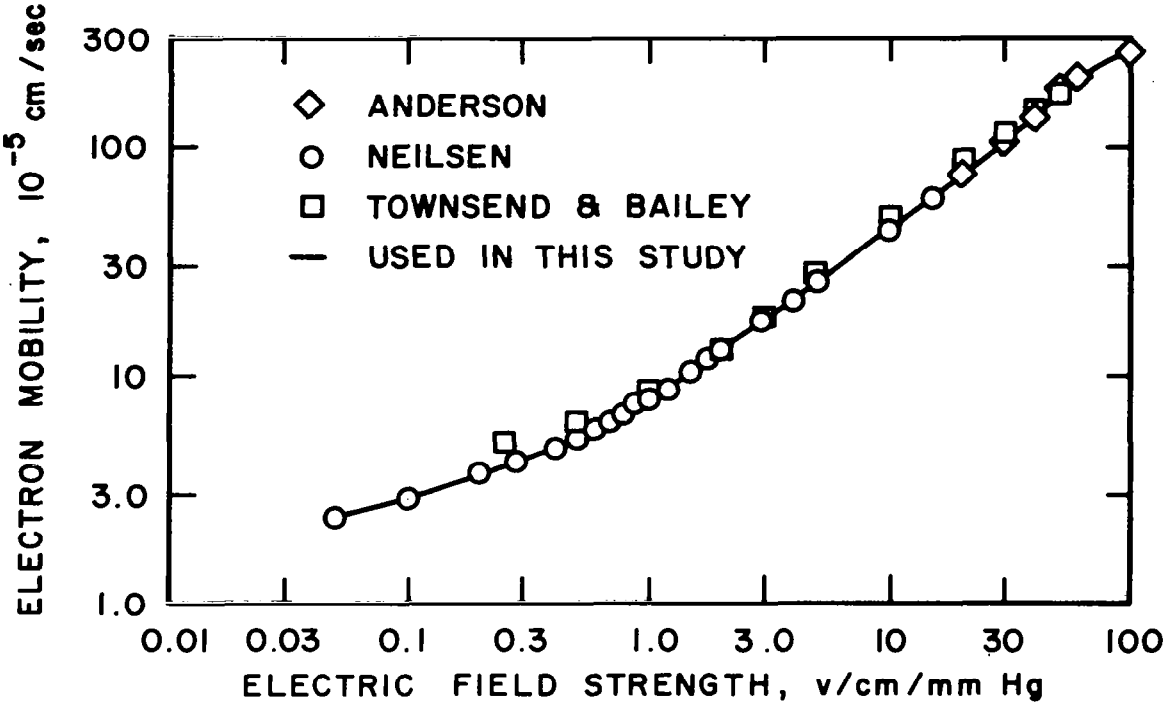

a) Electron Mobility, W

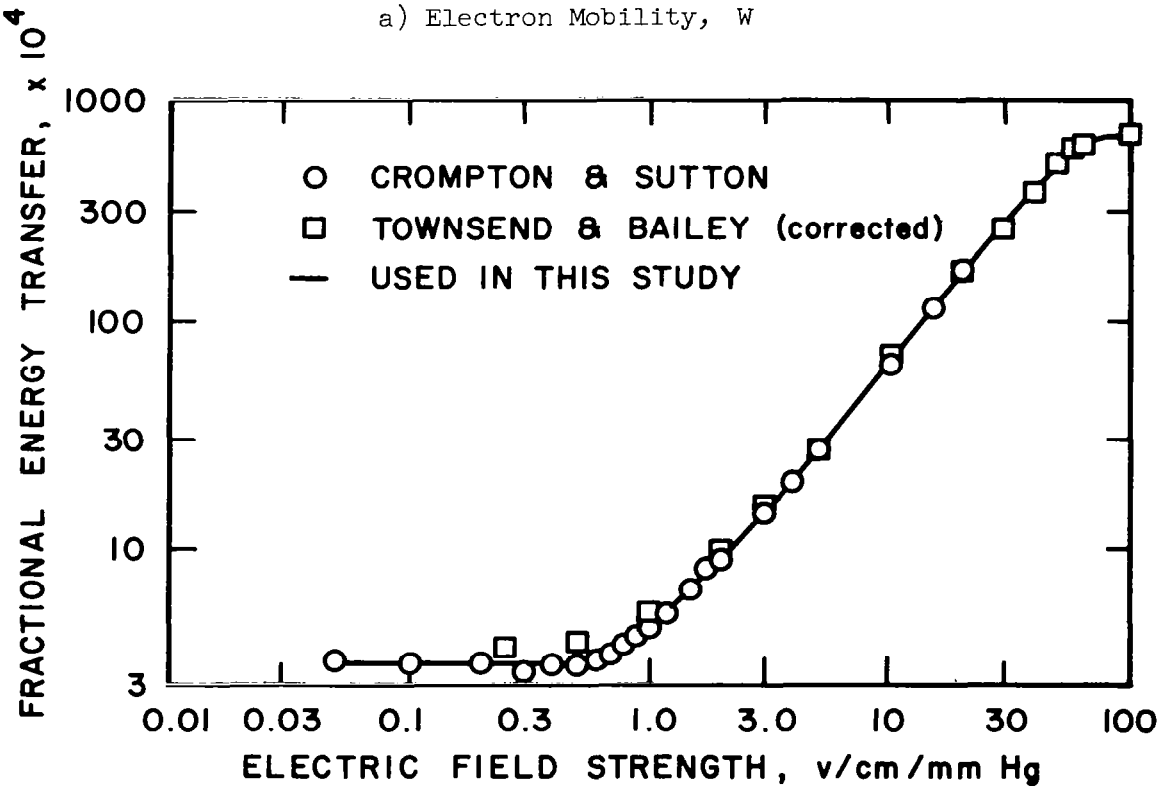

b) Fractional Energy Transfer, η

FIG. 18. ELECTRON CHARACTERISTICS AS A FUNCTION OF ELECTRIC FIELD STRENGTH.

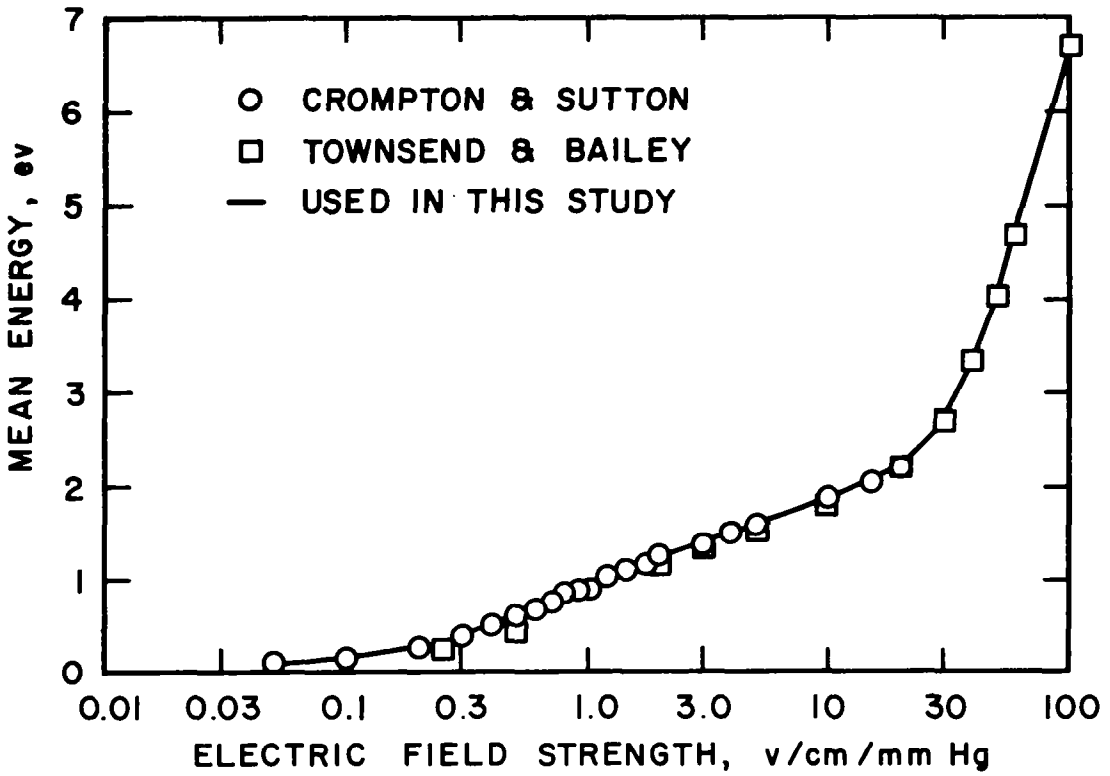

c) Mean Energy, ϵ

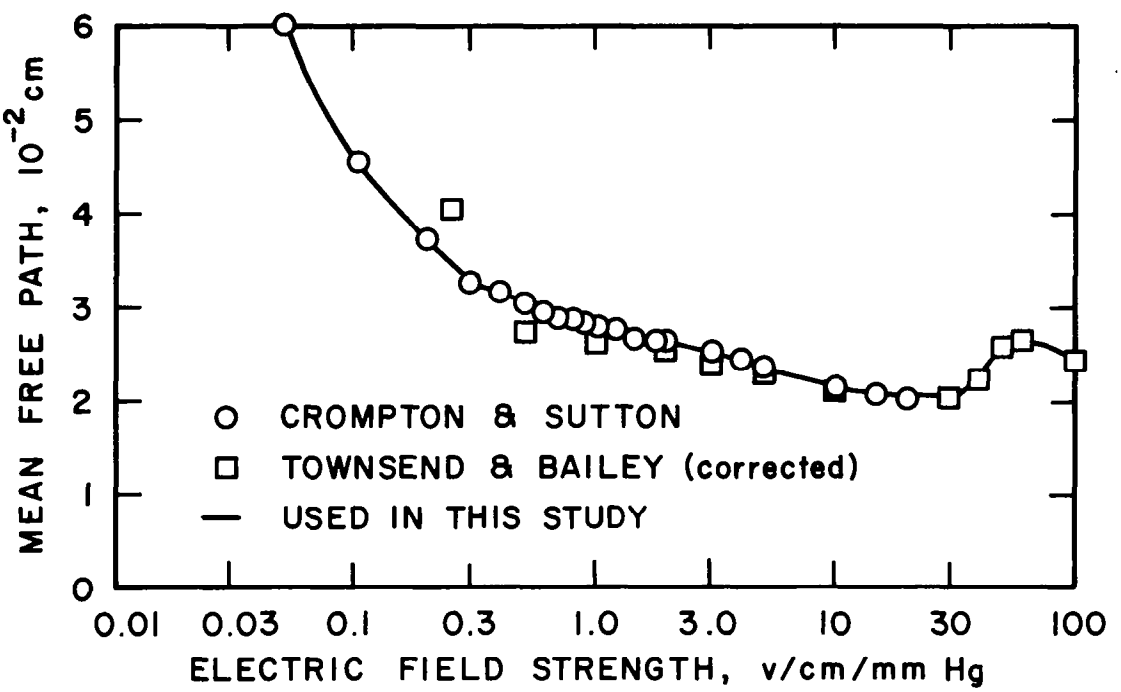

d) Mean Free Path, ℓ_e

FIG. 18. CONCLUDED.

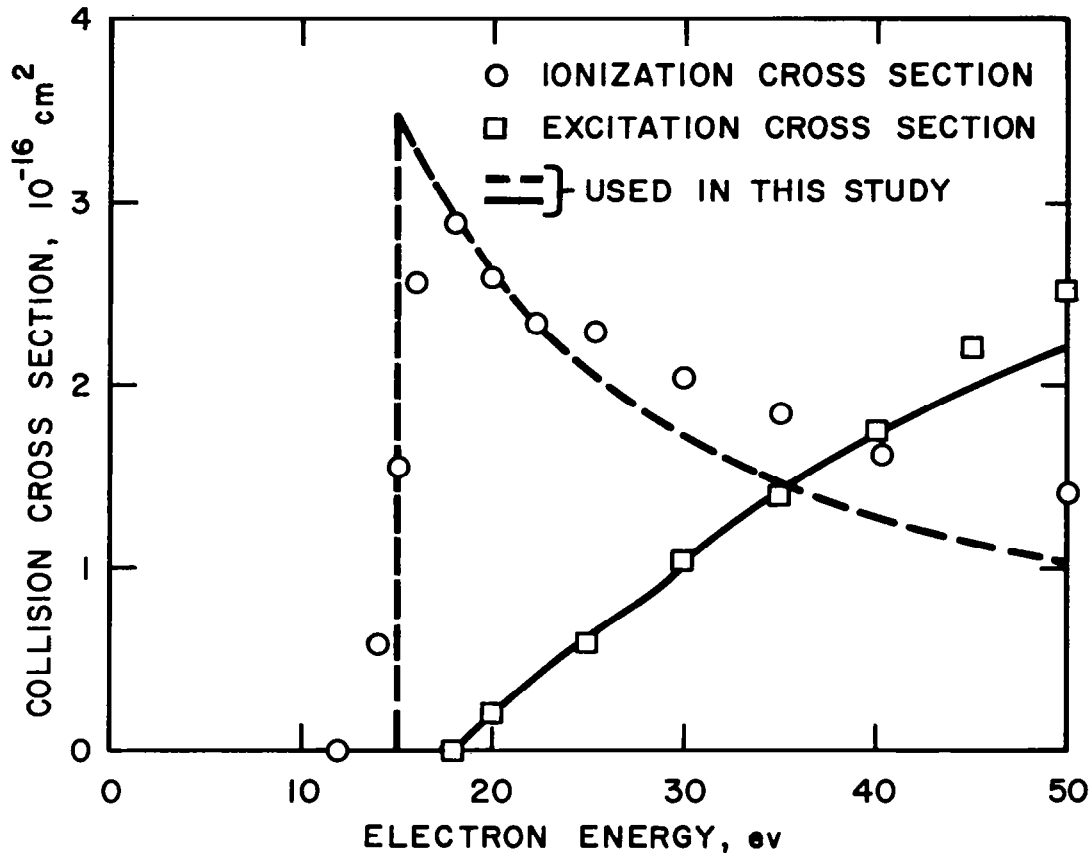

FIG. 19. COLLISION CROSS SECTIONS FOR IONIZATION AND EXCITATION OF SECOND-POSITIVE BAND SYSTEM.

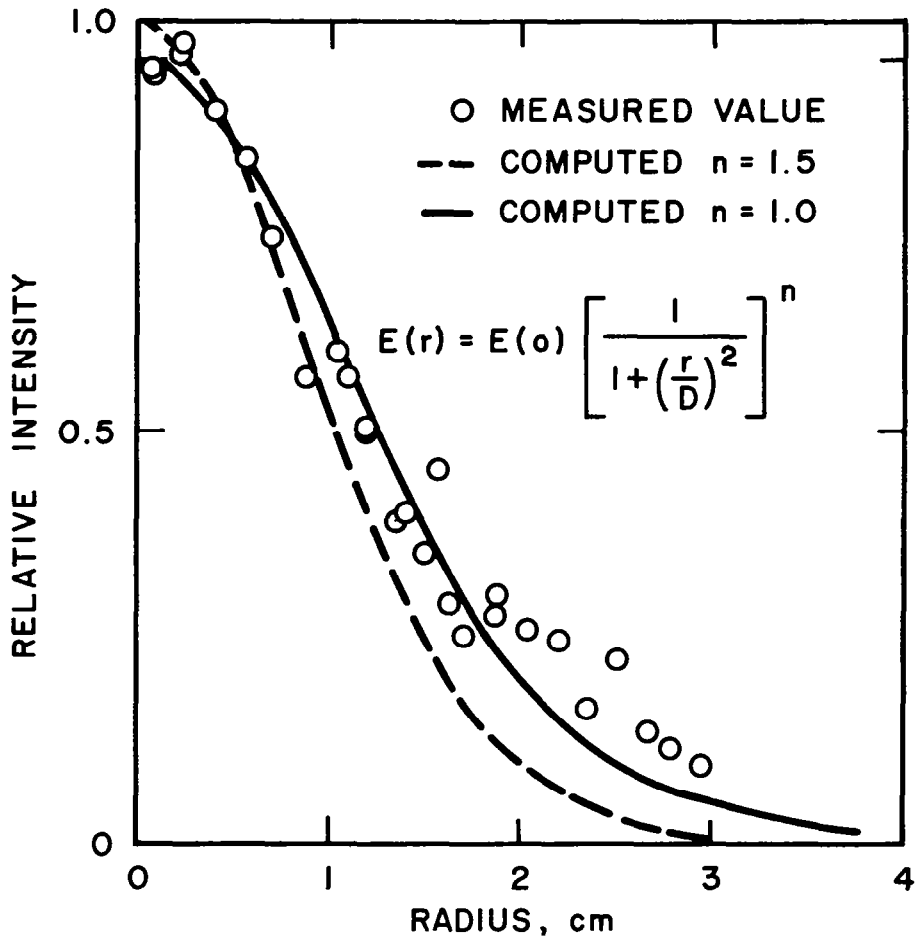

a) Without a Magnetic Field

FIG. 20. COMPARISON OF INTEGRATED INTENSITY PROFILES.

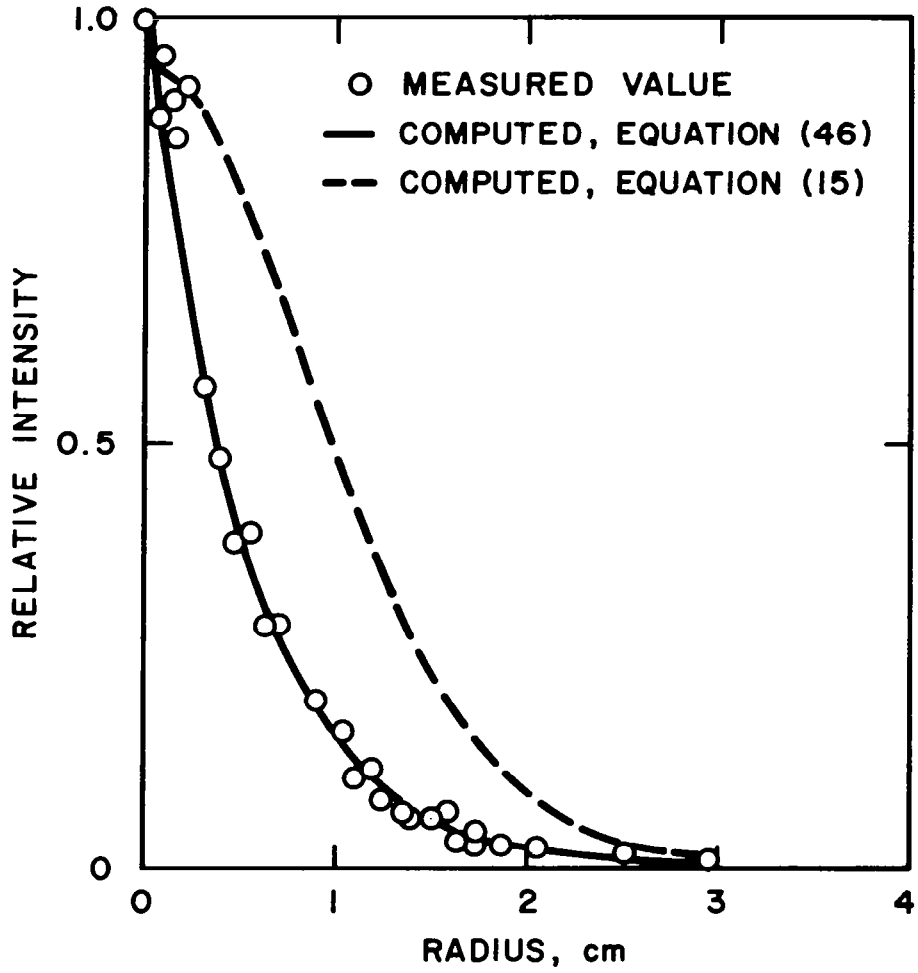

b) With a 655-Gauss Magnetic Field

FIG. 20. CONCLUDED.

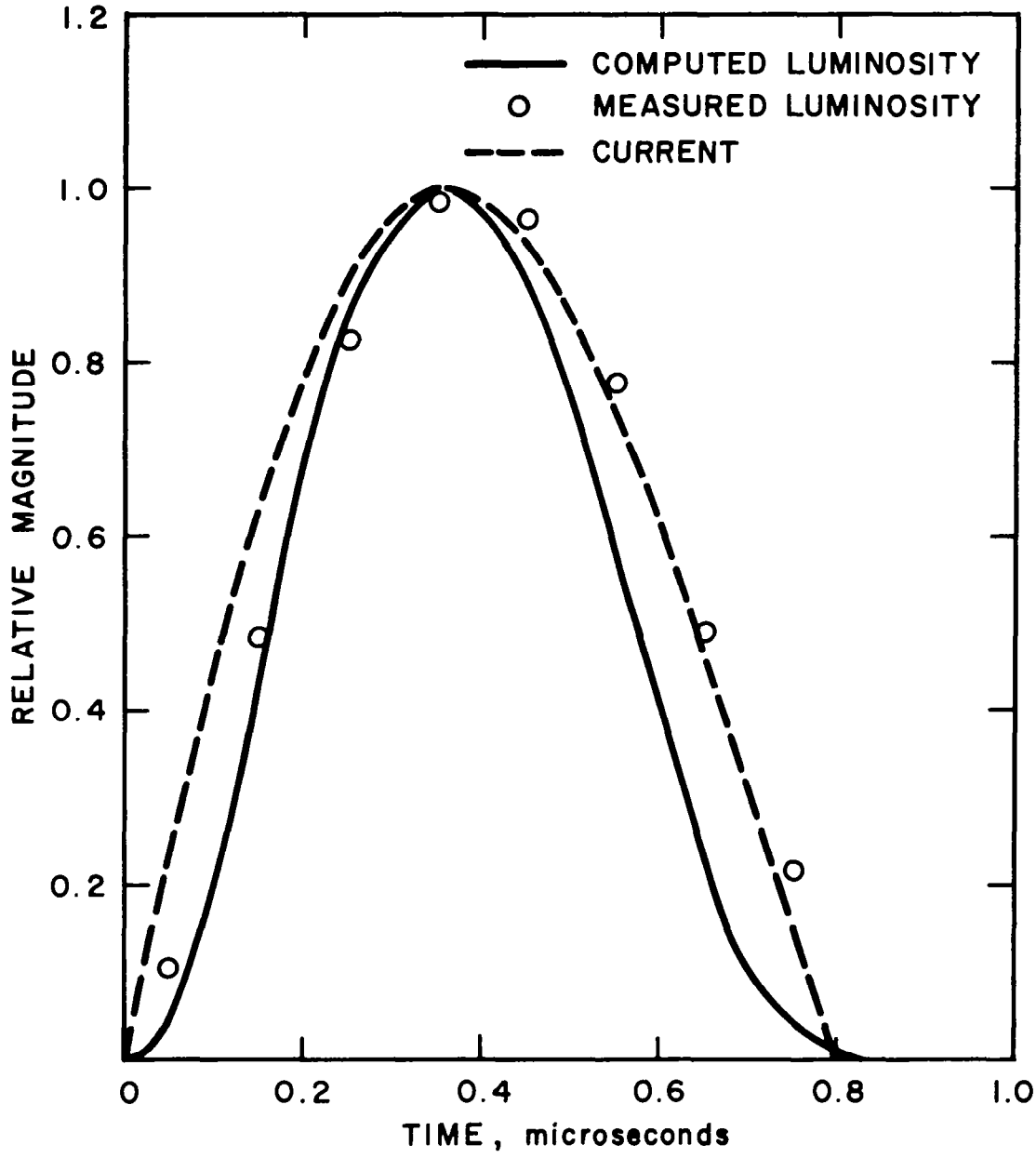

a) Without a Magnetic Field

FIG. 21. COMPARISON OF COMPUTED AND MEASURED LUMINOSITY.

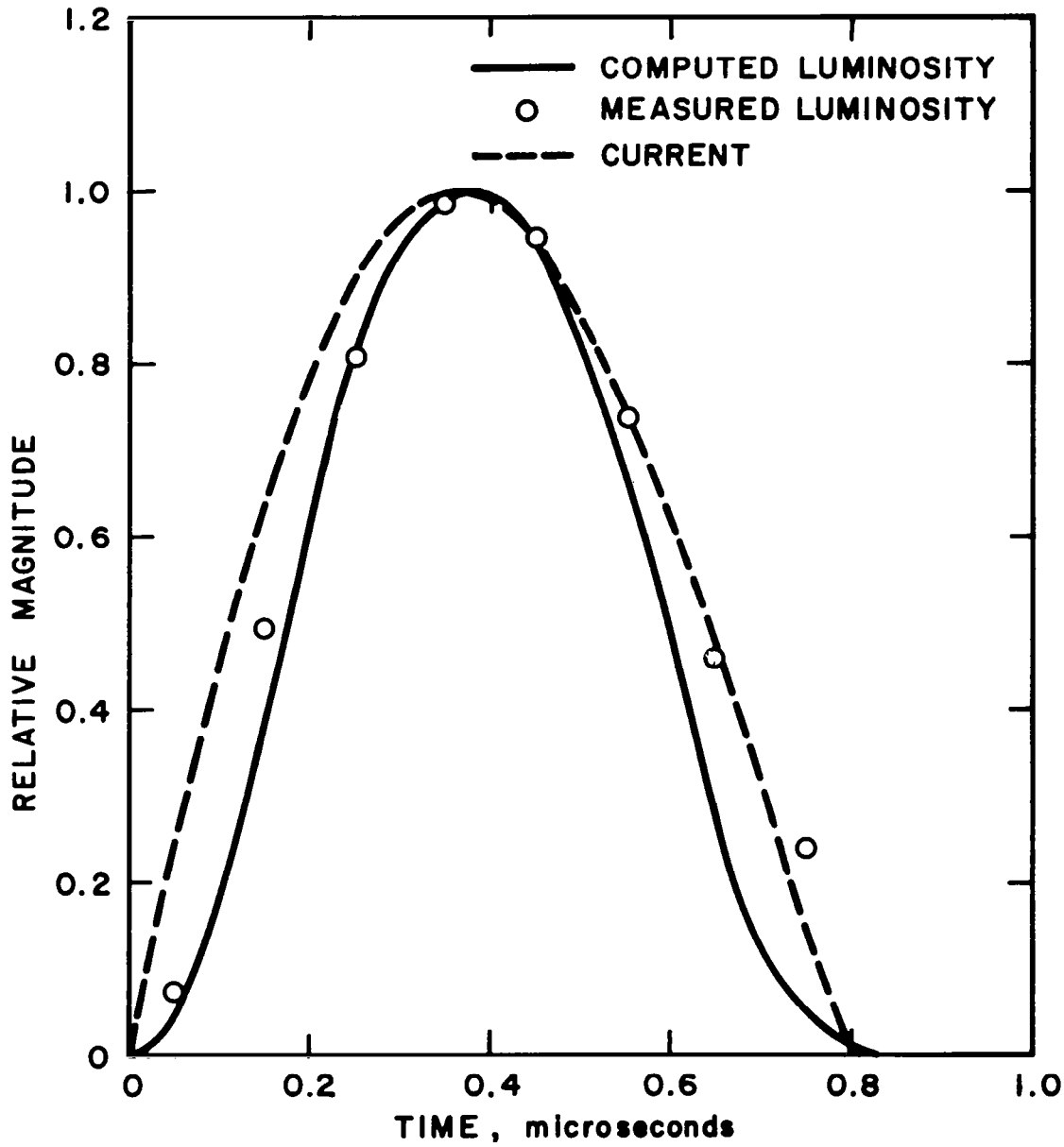

b) With a 655-Gauss Magnetic Field

FIG. 21. CONCLUDED.

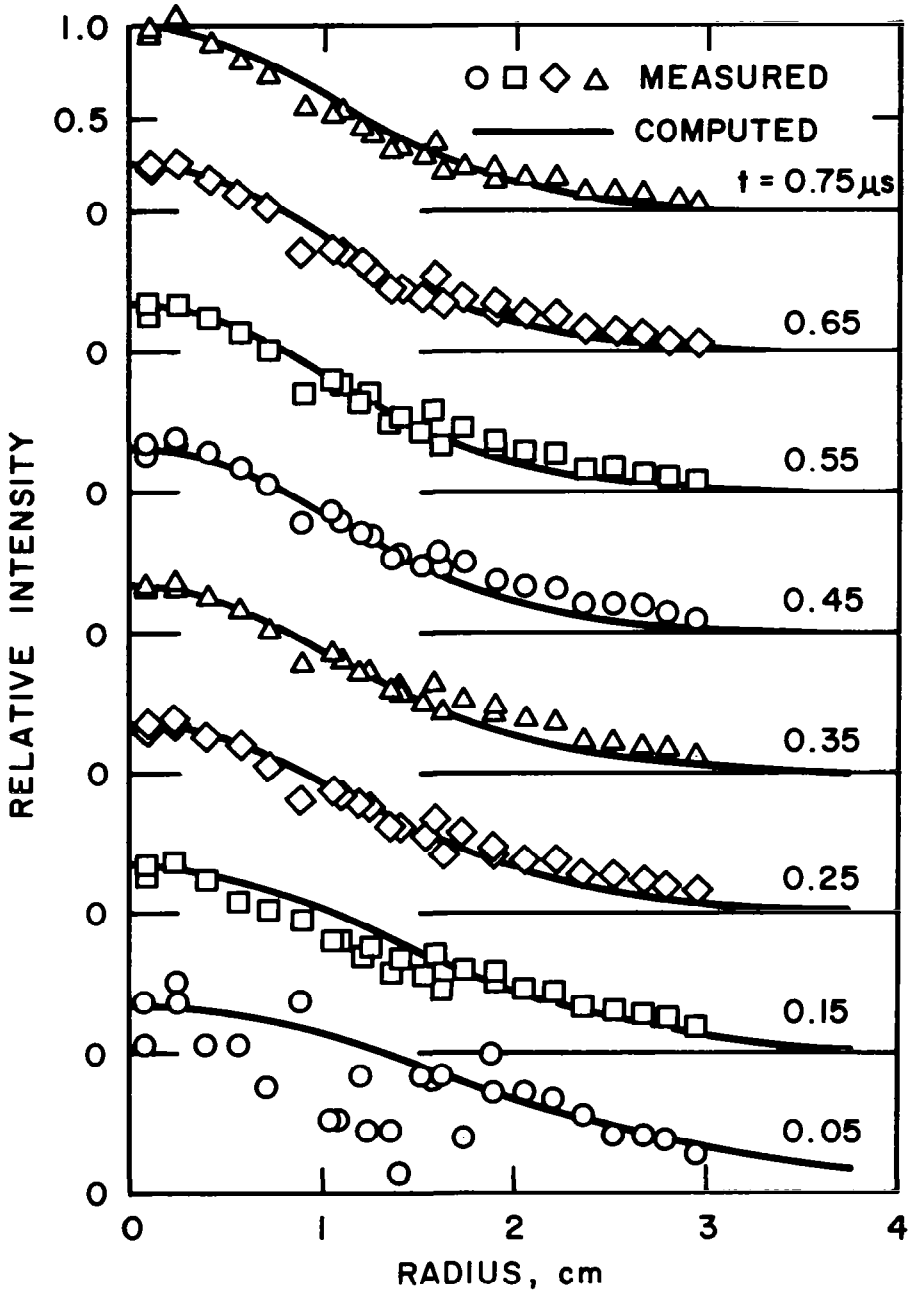

a) Without a Magnetic Field

FIG. 22. COMPARISON OF COMPUTED AND MEASURED TIME-RESOLVED INTENSITY PROFILES.

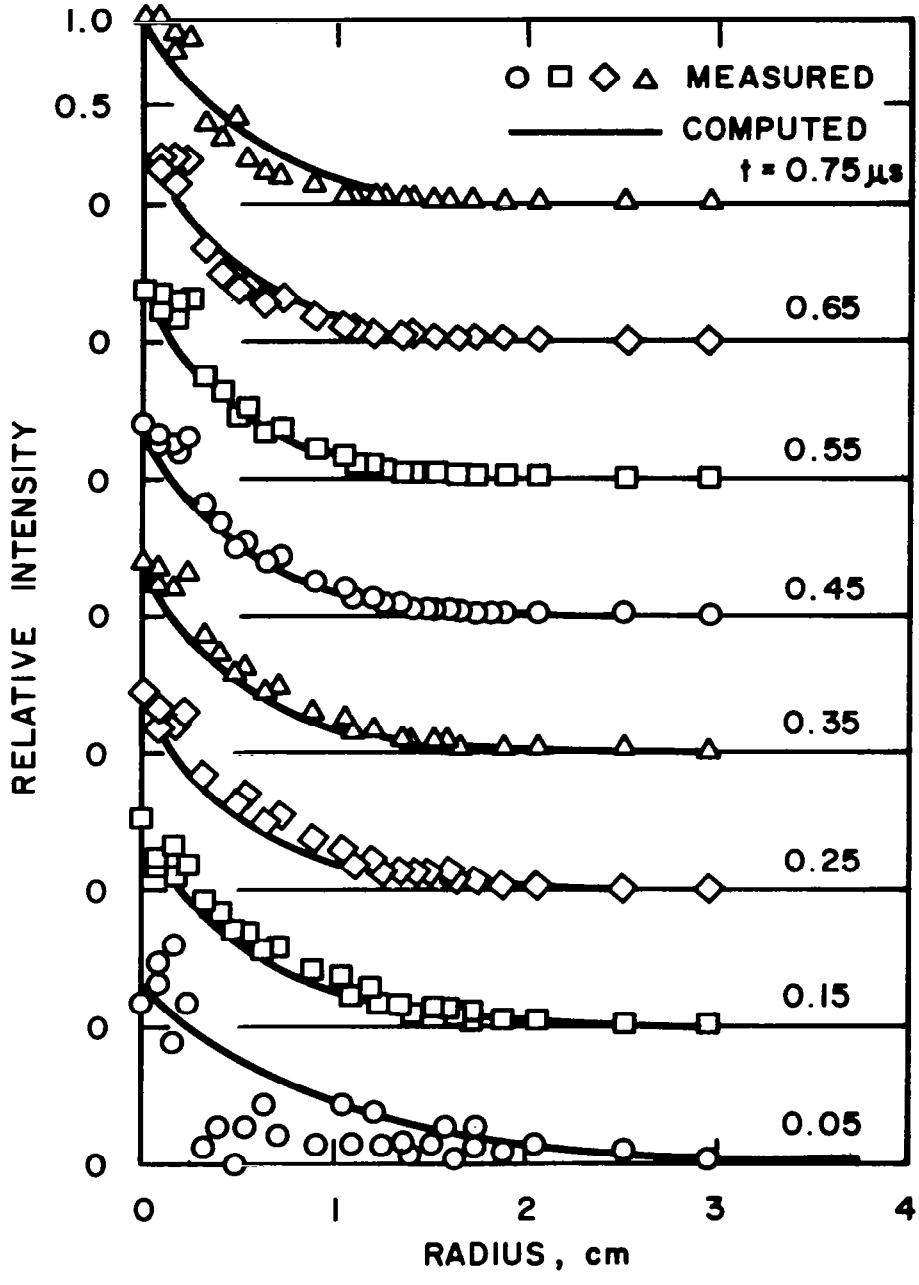

b) With a 655-Gauss Magnetic Field

FIG. 22. CONCLUDED.

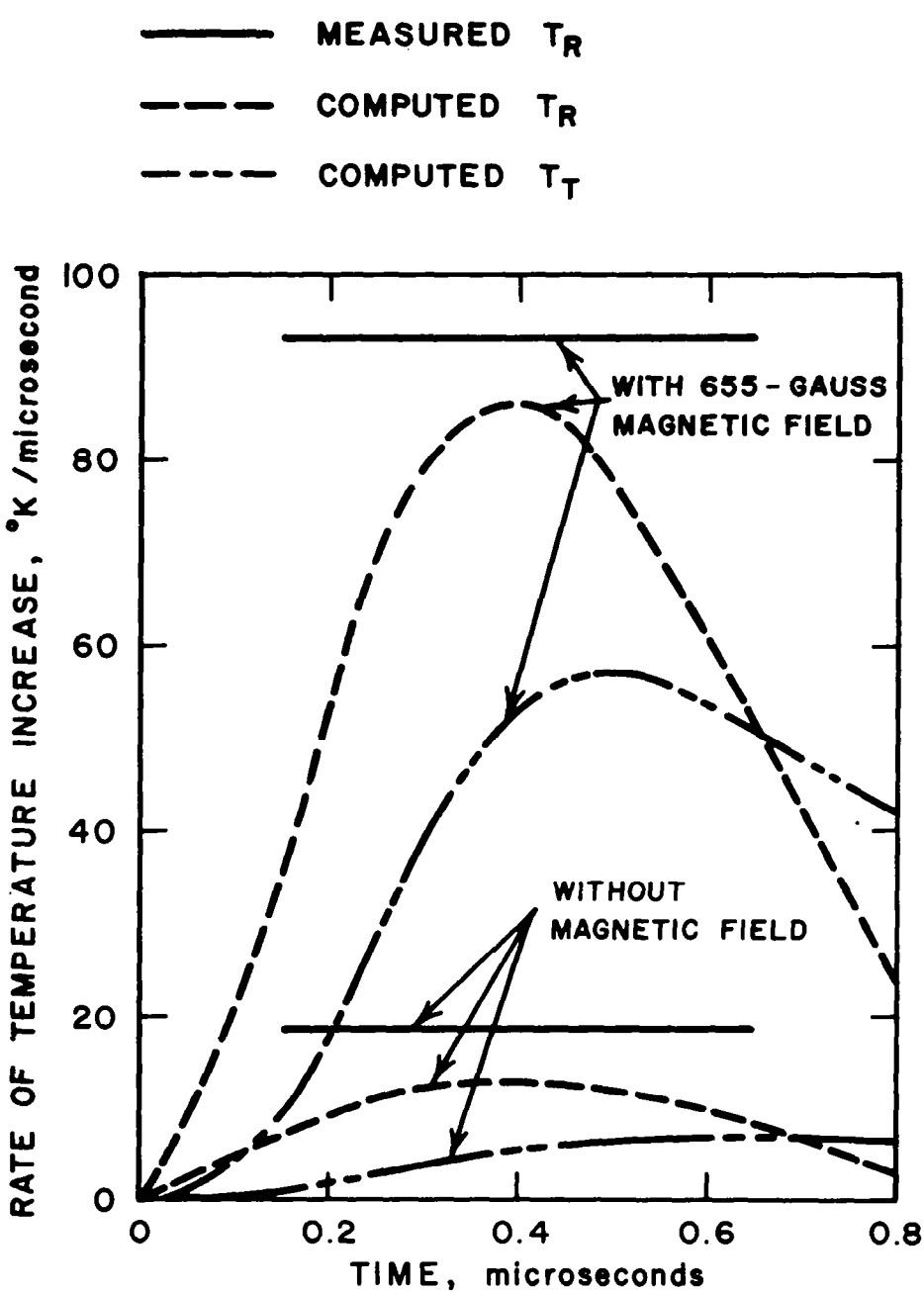

FIG. 23. COMPARISON OF COMPUTED AND MEASURED RATES OF TEMPERATURE INCREASE AT SPARK CENTERLINE.

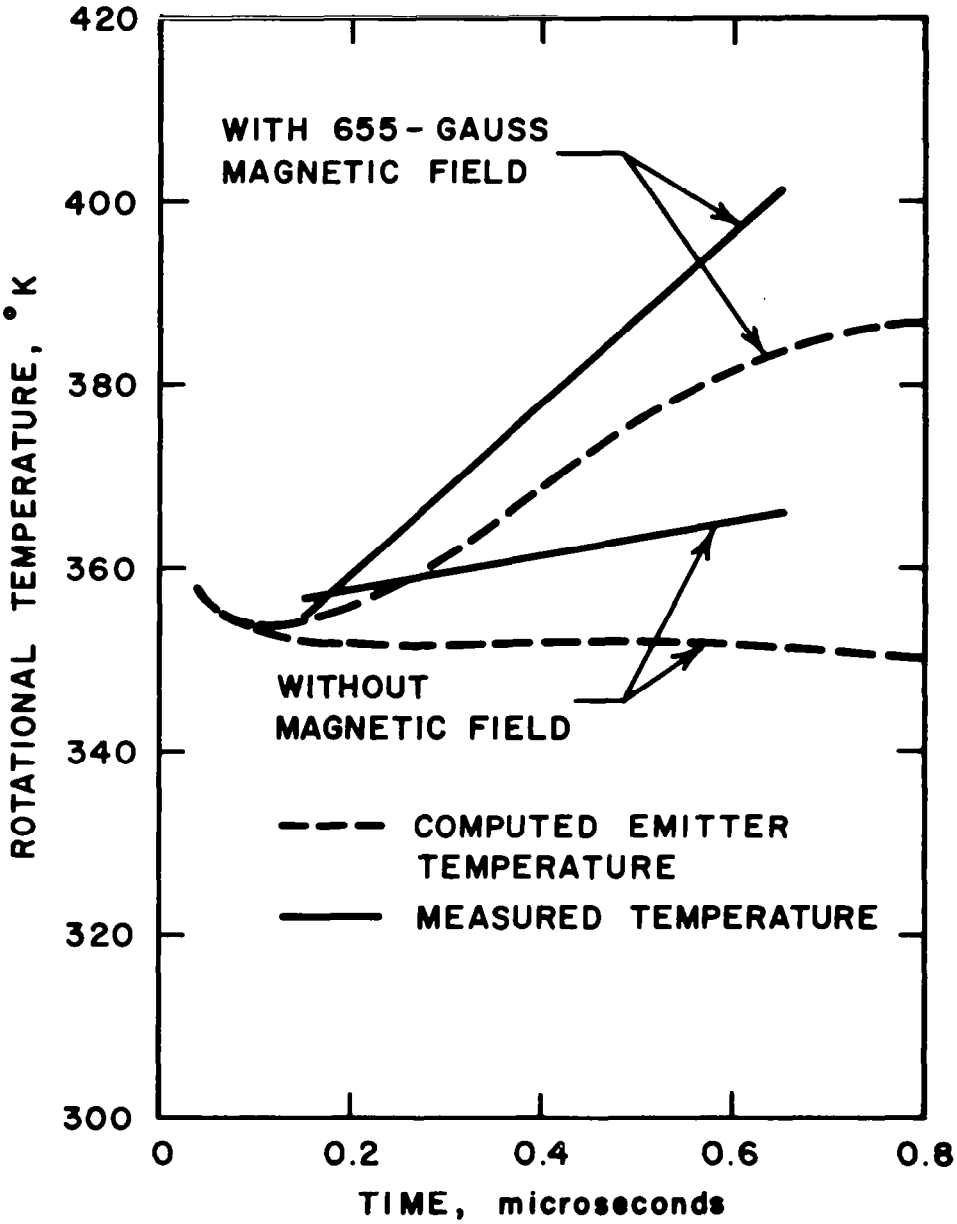

FIG. 24. COMPARISON OF COMPUTED EMITTER TEMPERATURE AND MEASURED TEMPERATURE AT SPARK CENTERLINE.

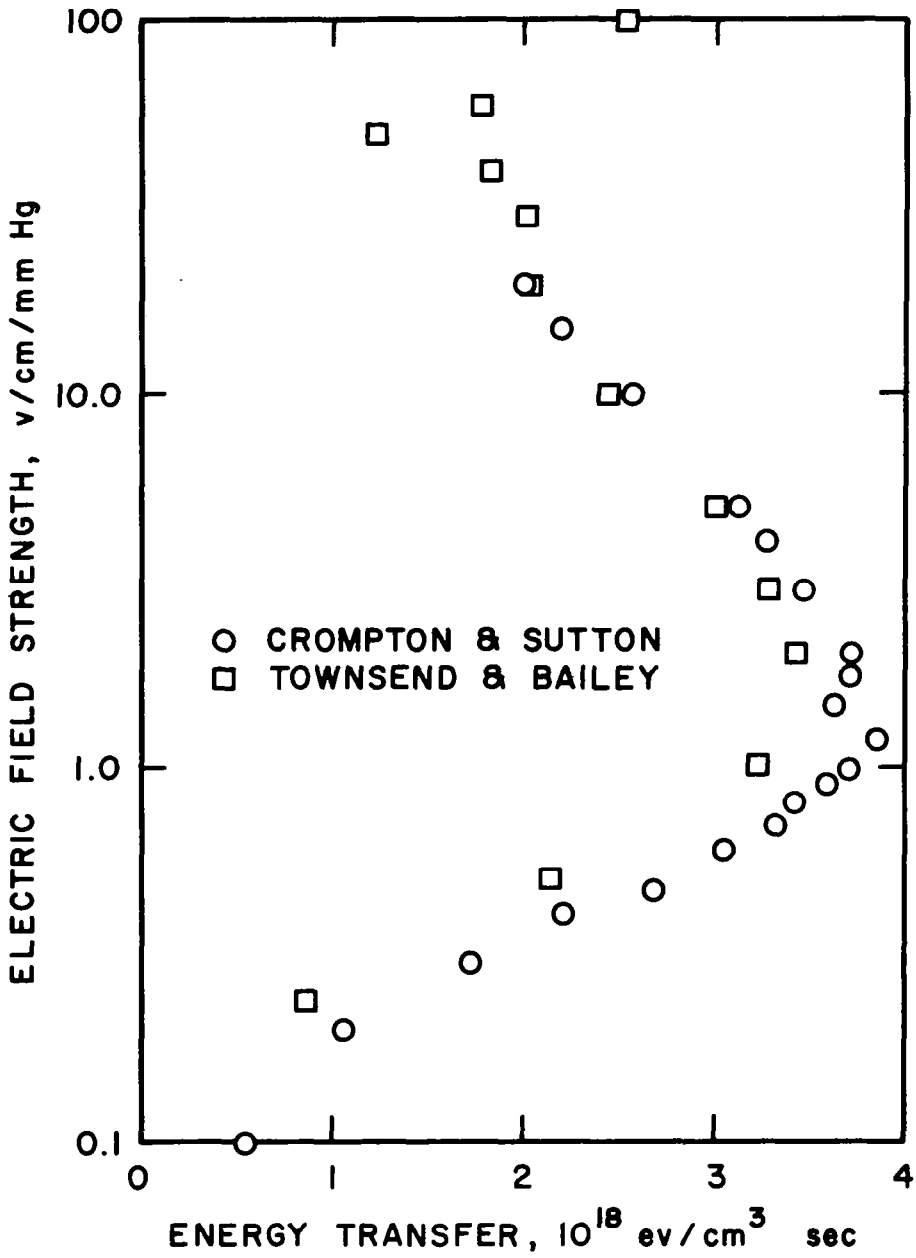

FIG. 25. RATE OF ROTATIONAL ENERGY INCREASE FOR A CURRENT DENSITY OF 1.0 amp/cm^2.

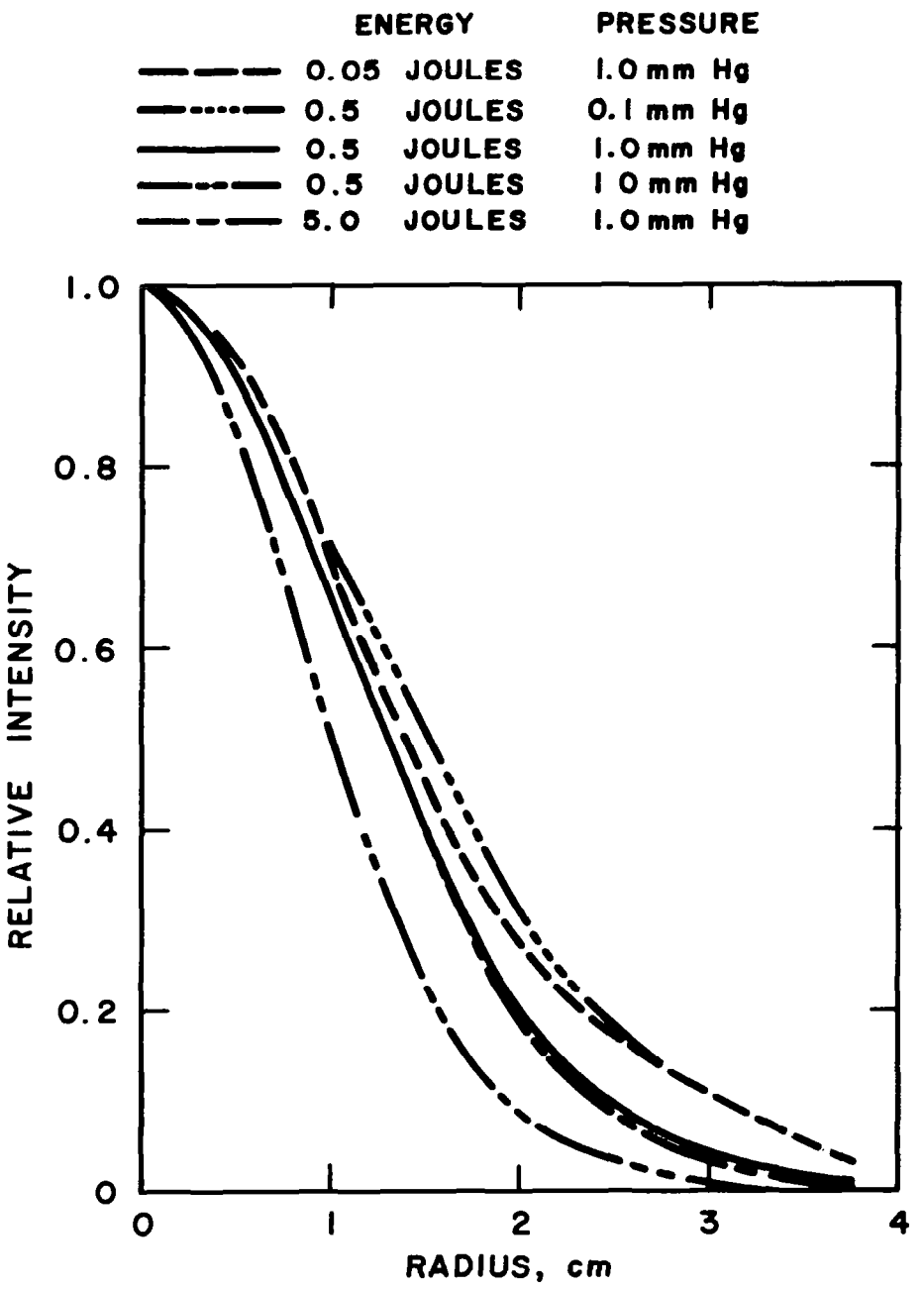

FIG. 26. EFFECT OF SPARK ENERGY AND STATIC PRESSURE ON COMPUTED INTEGRATED INTENSITY PROFILE.

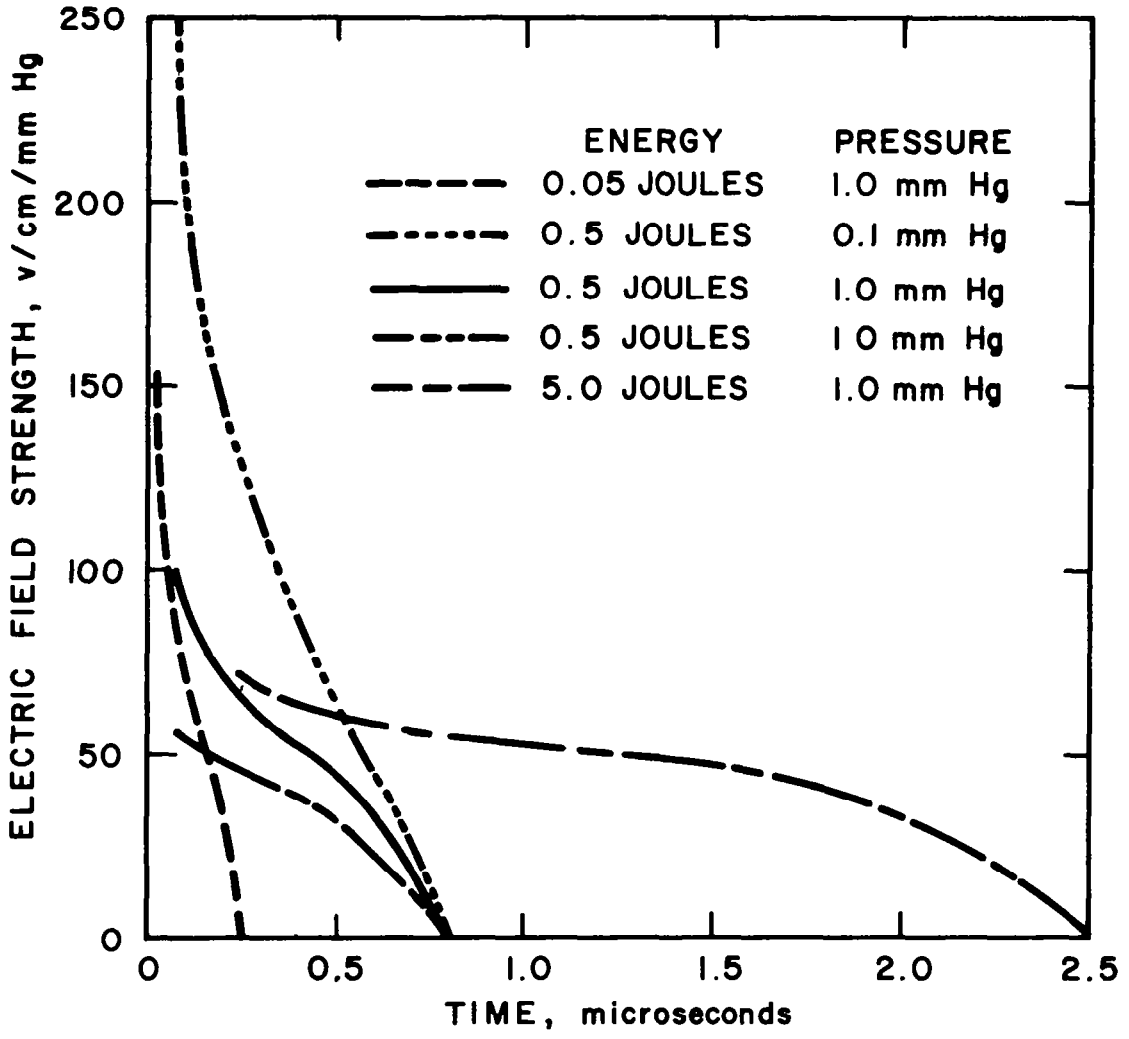

FIG. 27. EFFECT OF SPARK ENERGY AND STATIC PRESSURE ON COMPUTED ELECTRIC FIELD STRENGTH.

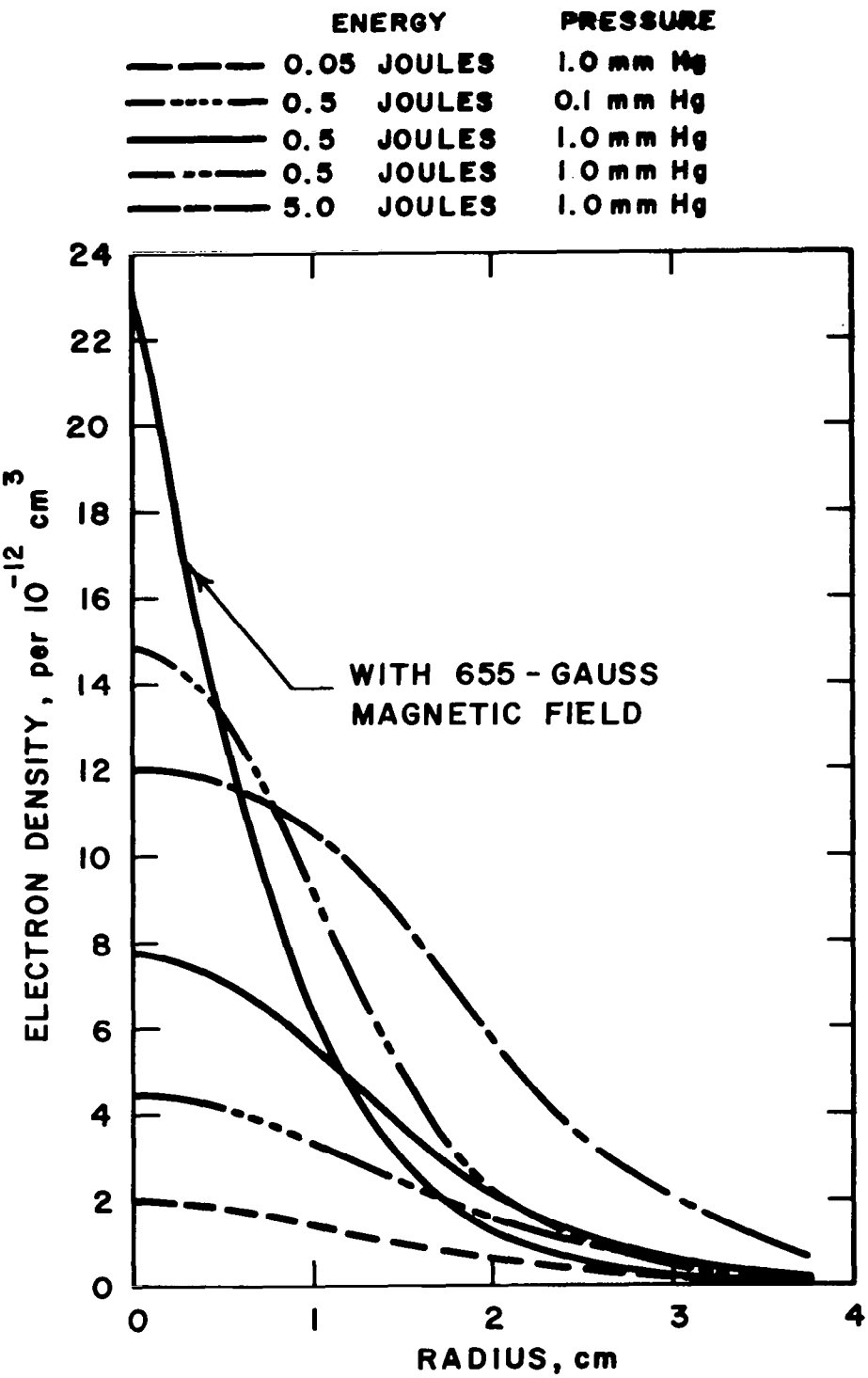

a) At Termination of Spark

FIG. 28. EFFECT OF SPARK ENERGY, STATIC PRESSURE, AND MAGNETIC FIELD STRENGTH ON COMPUTED ELECTRON DENSITY

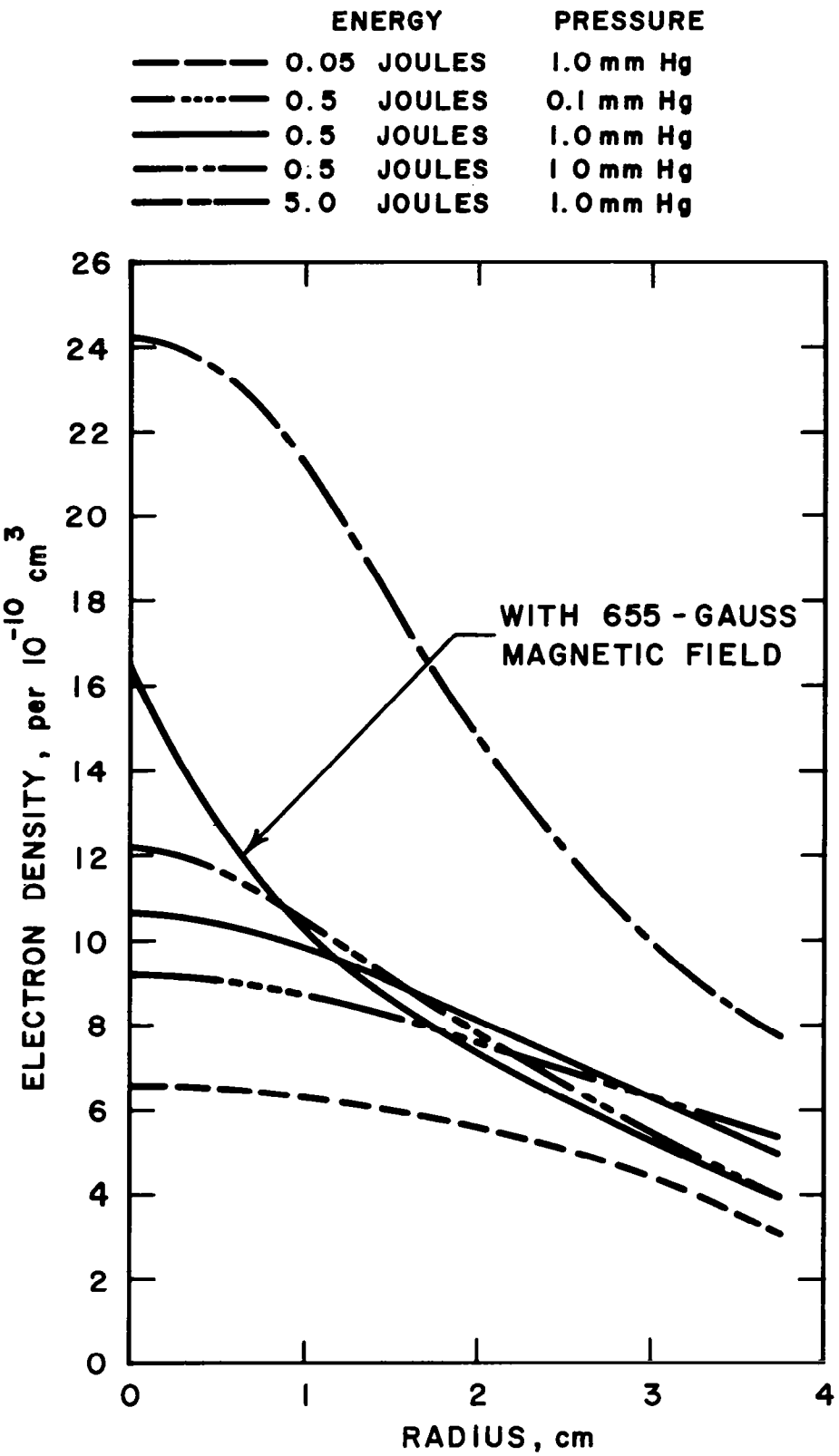

b) At 50 Microseconds

FIG. 28. CONCLUDED.

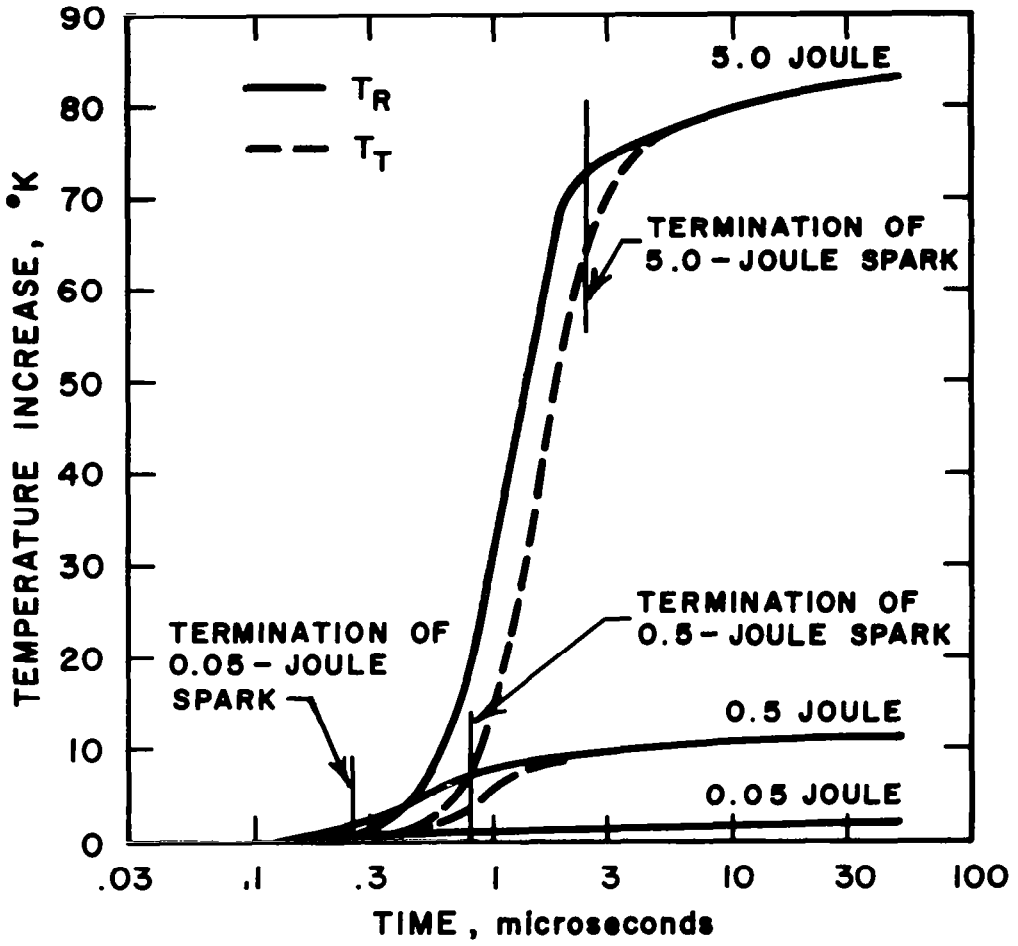

FIG. 29. COMPUTED TEMPERATURE INCREASE AT SPARK-HEATED COLUMN CENTERLINE AS A FUNCTION OF TIME.

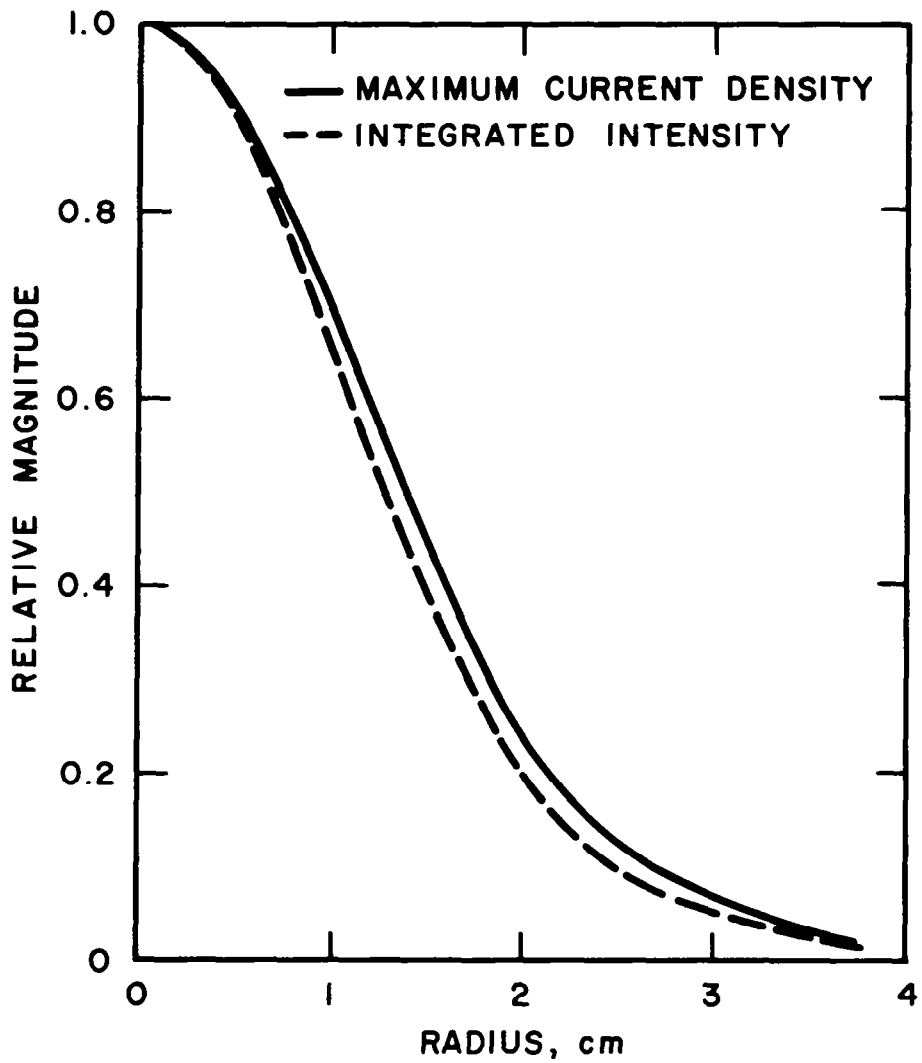

FIG. 30. COMPARISON OF COMPUTED MAXIMUM-CURRENT-DENSITY AND INTEGRATED INTENSITY PROFILES.

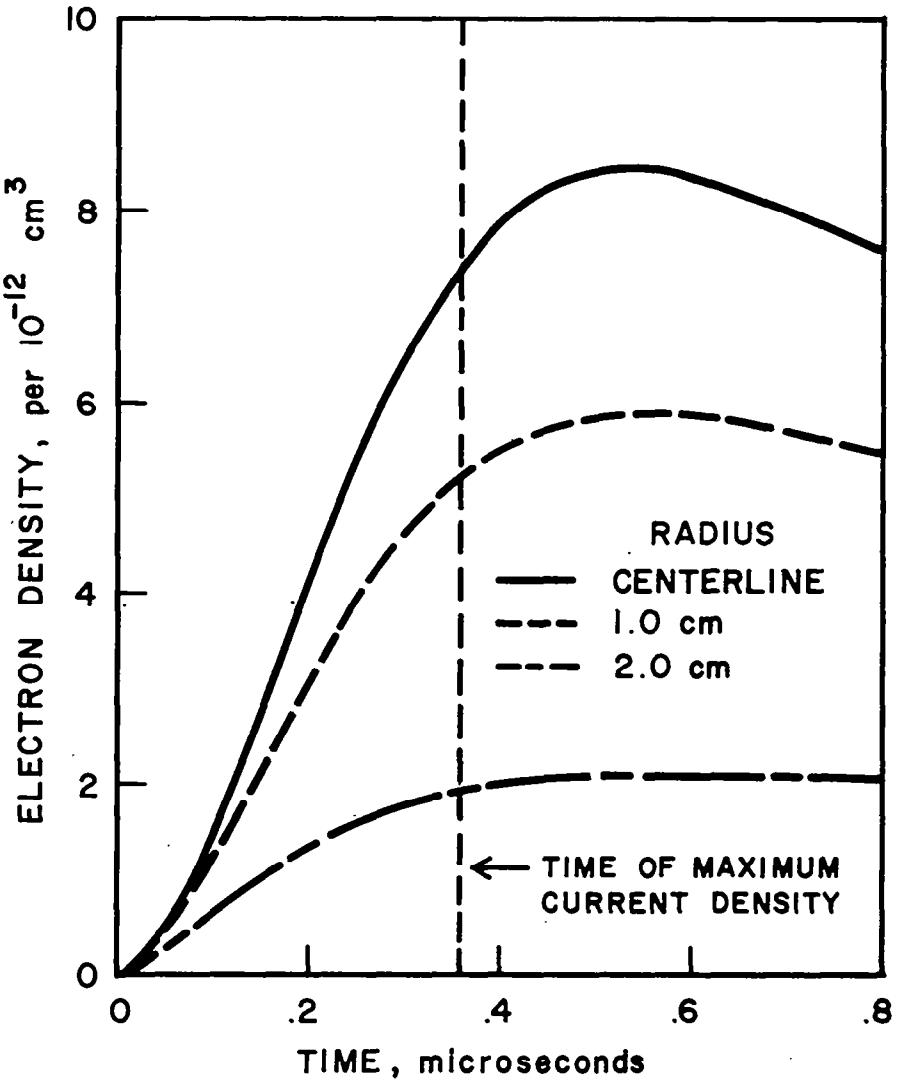

FIG. 31. VARIATION OF COMPUTED ELECTRON DENSITY WITH TIME.

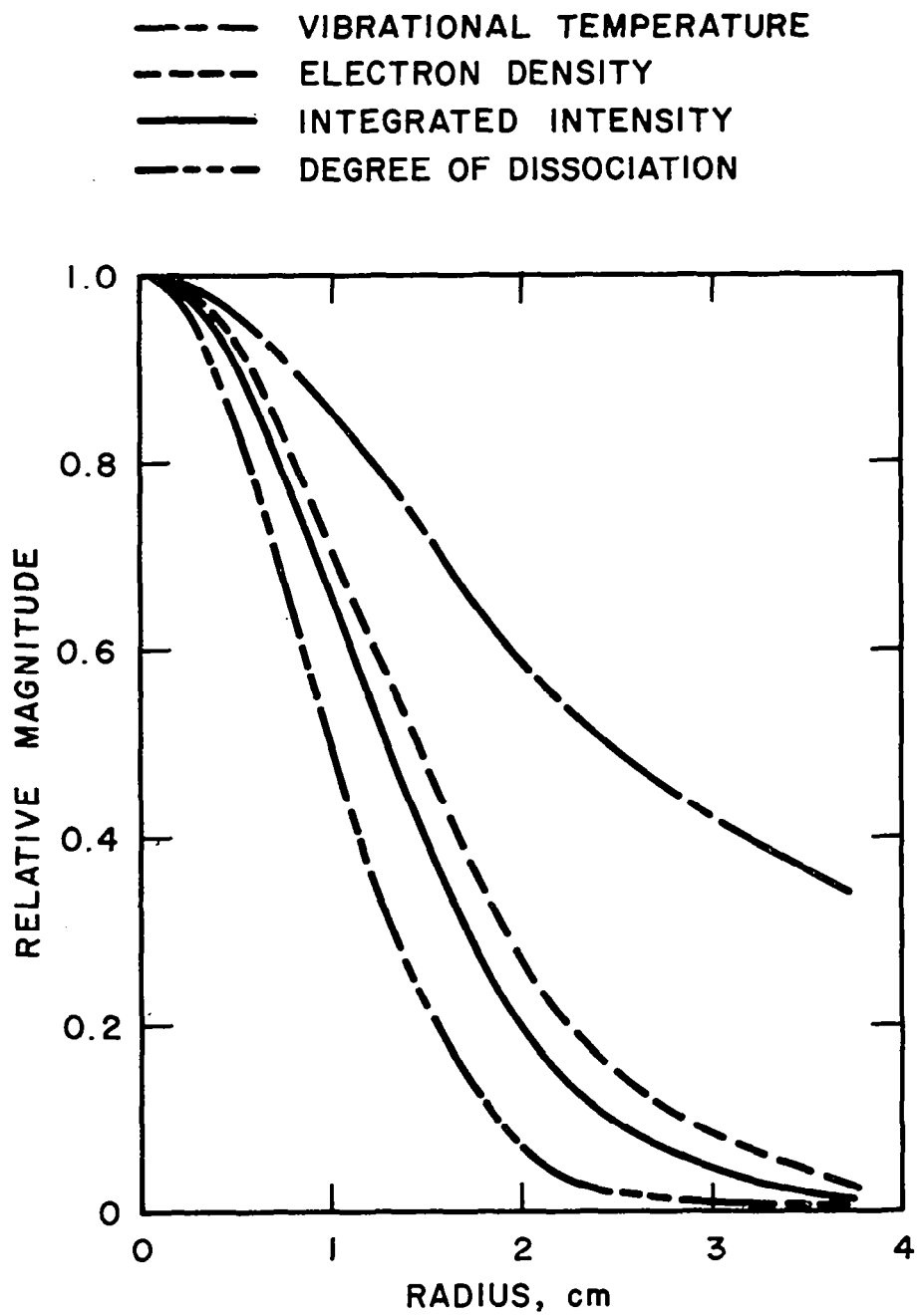

a) At Termination of Spark

FIG. 32. COMPARISON OF VARIOUS COMPUTED PROFILES.

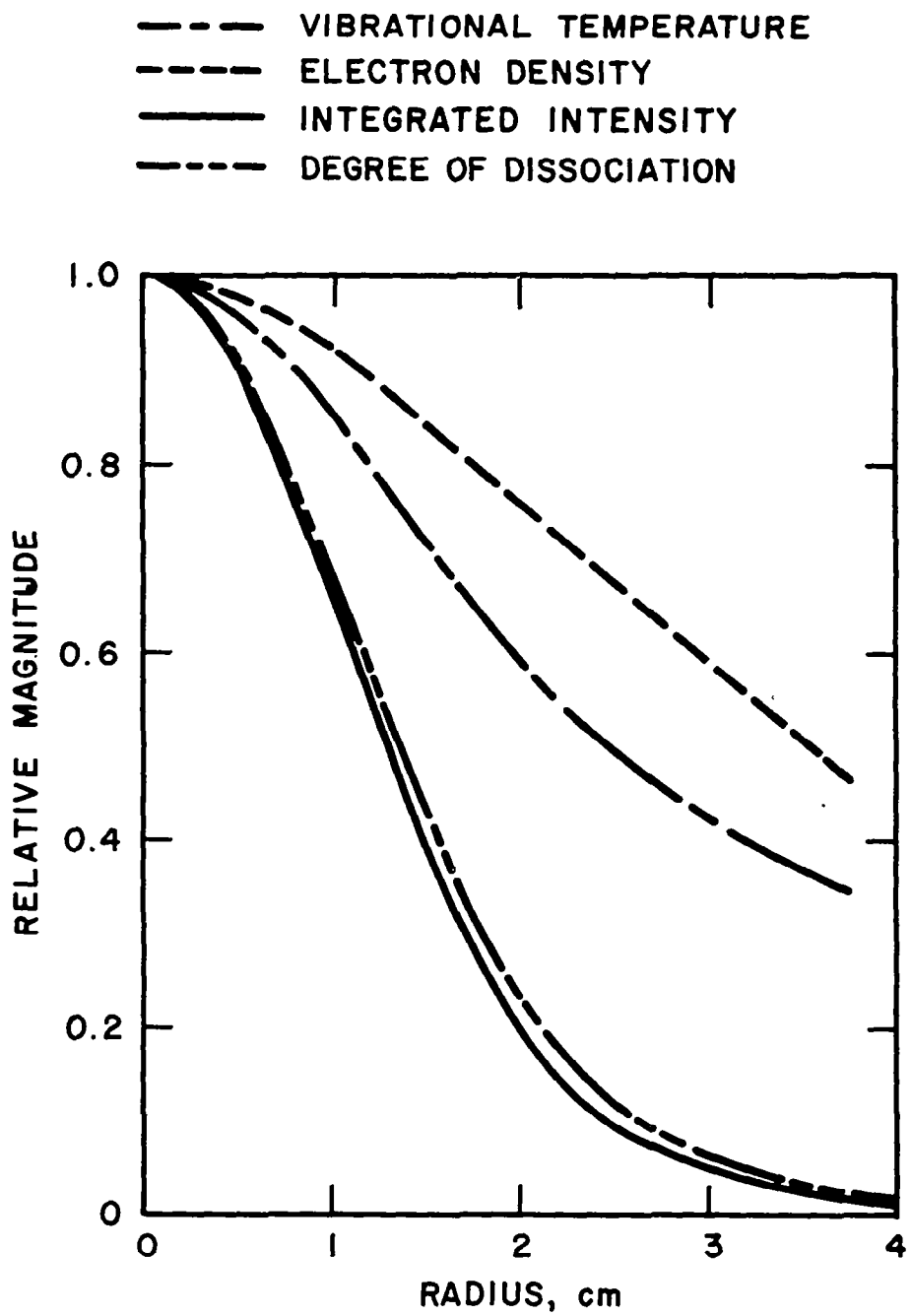

b) At 50 Microseconds

FIG. 32. CONCLUDED.

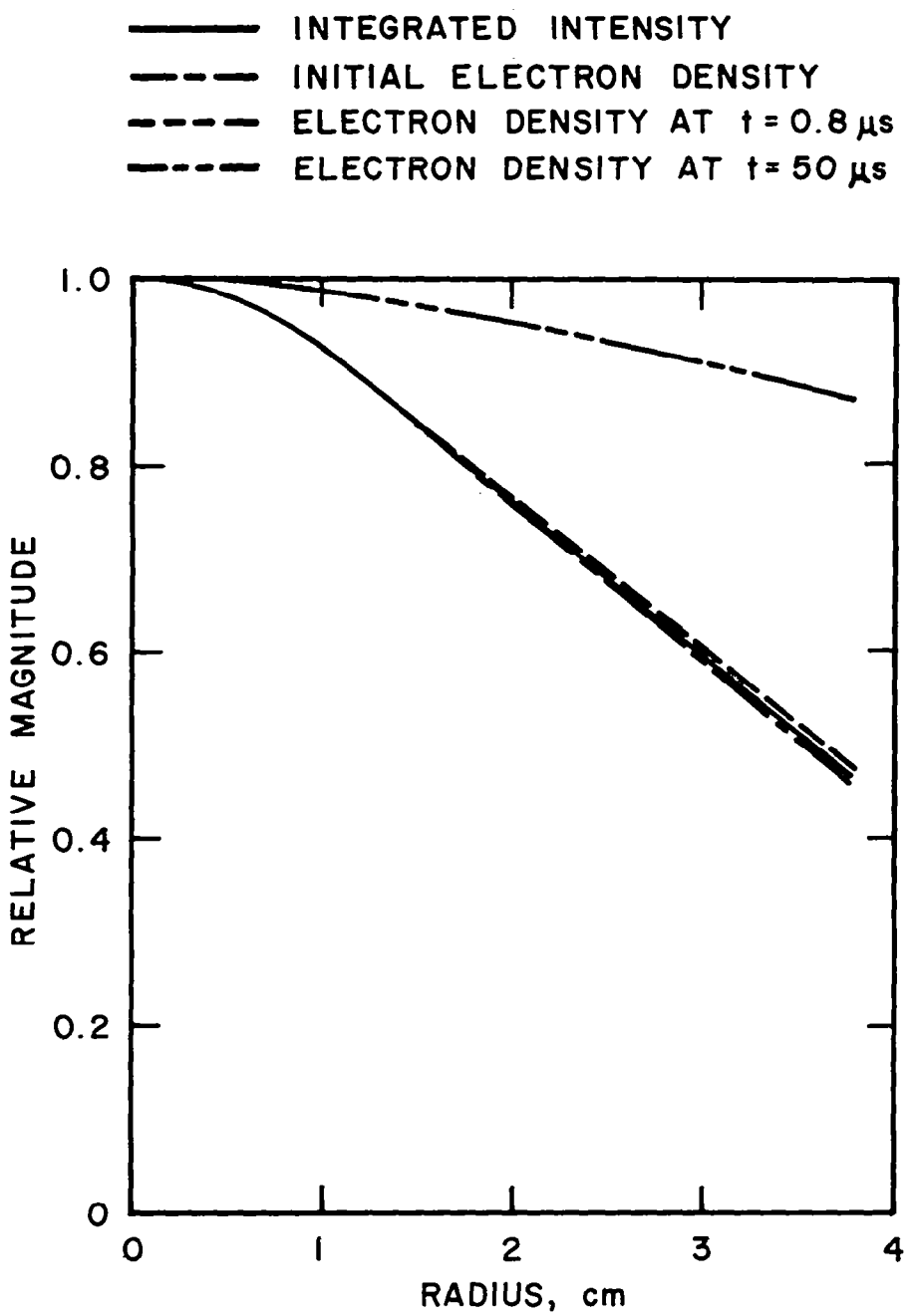

FIG. 33. COMPUTED INTEGRATED INTENSITY AND ELECTRON-DENSITY PROFILES FOR SPARK IN UNIFORM ELECTRIC FIELD.

FIG. 34. PHOTOGRAPH OF SPARKS ACROSS A 10-CM ELECTRODE GAP IN A HYPERSONIC STREAM

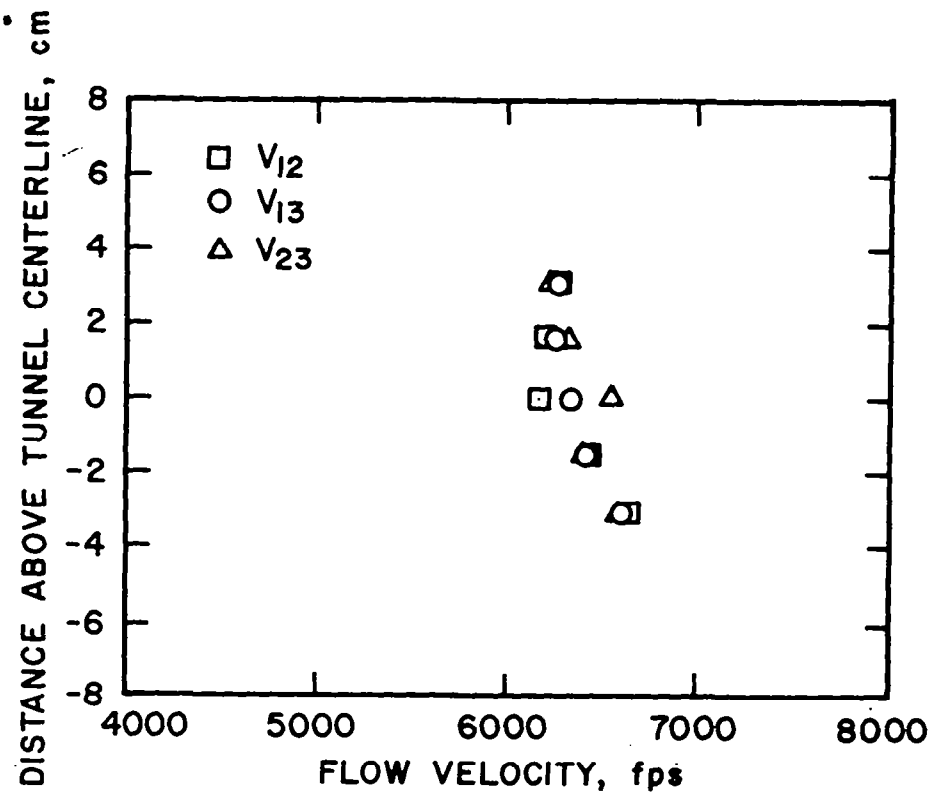

FIG. 35. FLOW-VELOCITY PROFILE COMPUTED FROM FIG. 34.

FIG. 36. PHOTOGRAPH OF SPARKS WITH MAGNETIC FIELD IN A HYPERSONIC STREAM

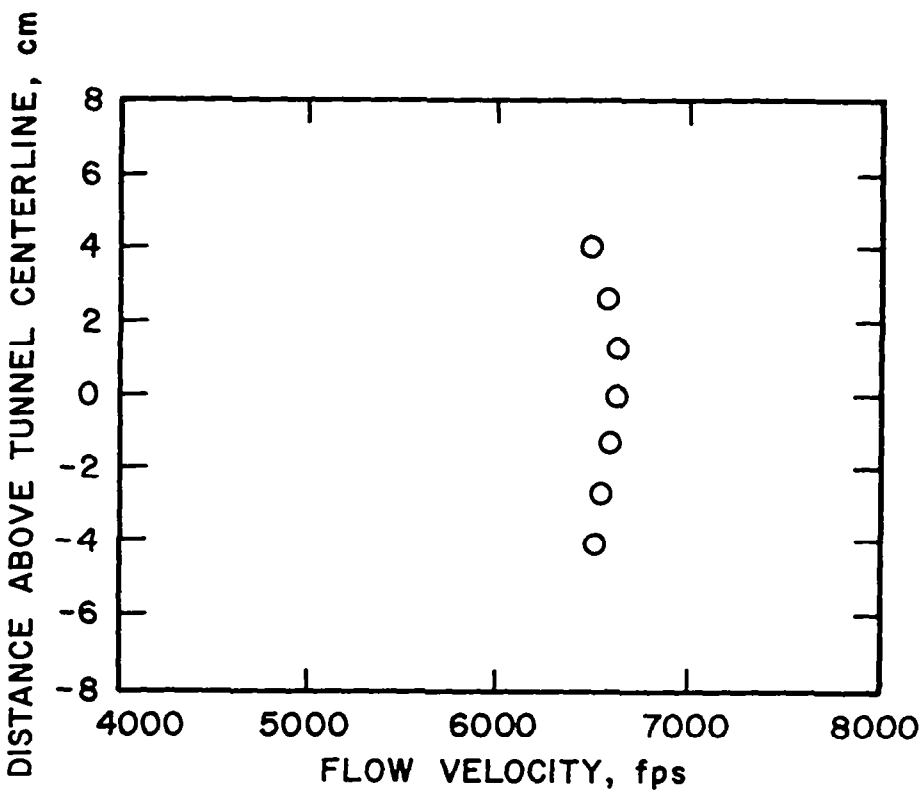

FIG. 37. FLOW-VELOCITY PROFILE COMPUTED FROM FIGURE 36.

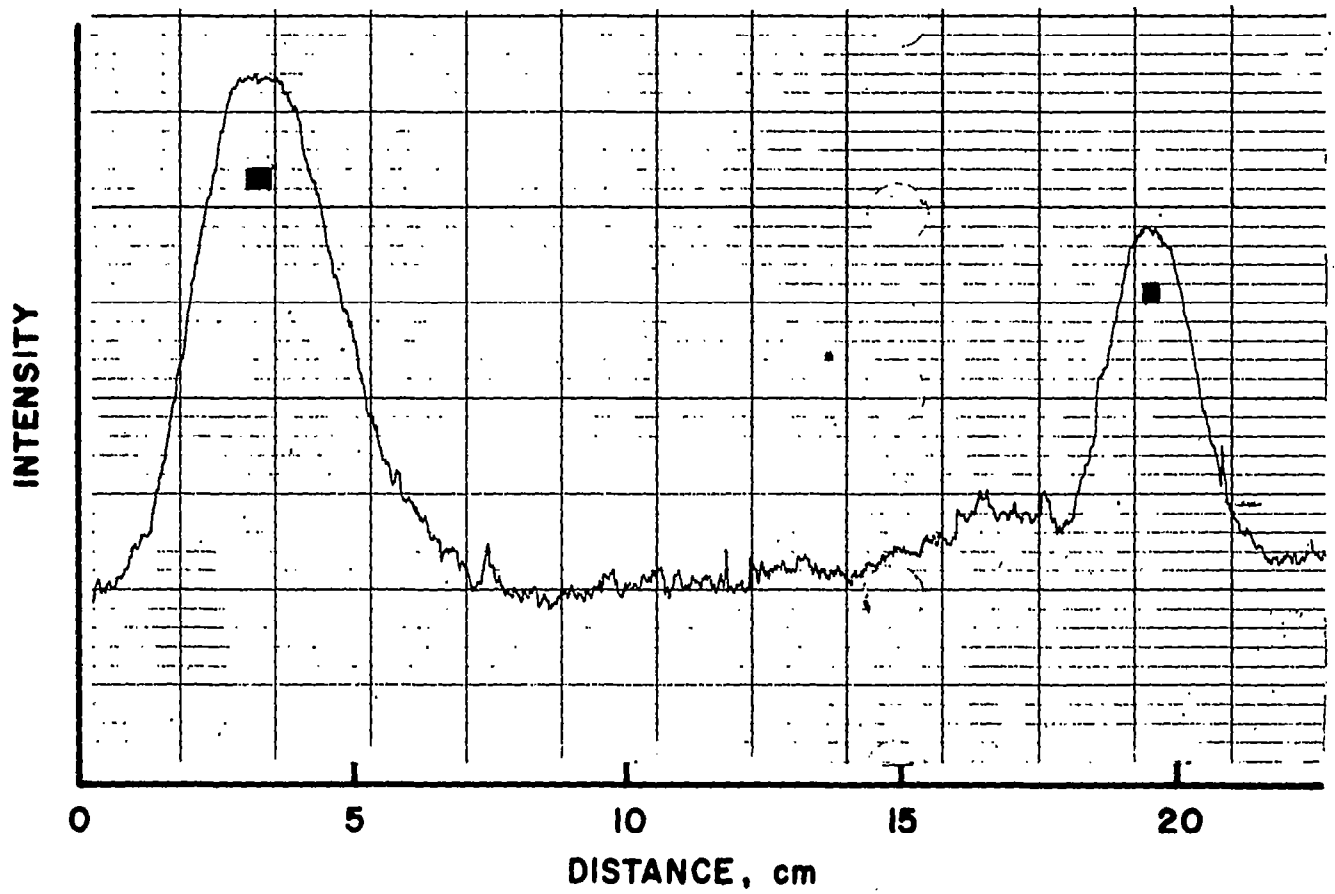

FIG. 38. MICROPHOTOMETER TRACE OF PHOTOGRAPH OF SPARKS IN A HYPERSONIC STREAM.

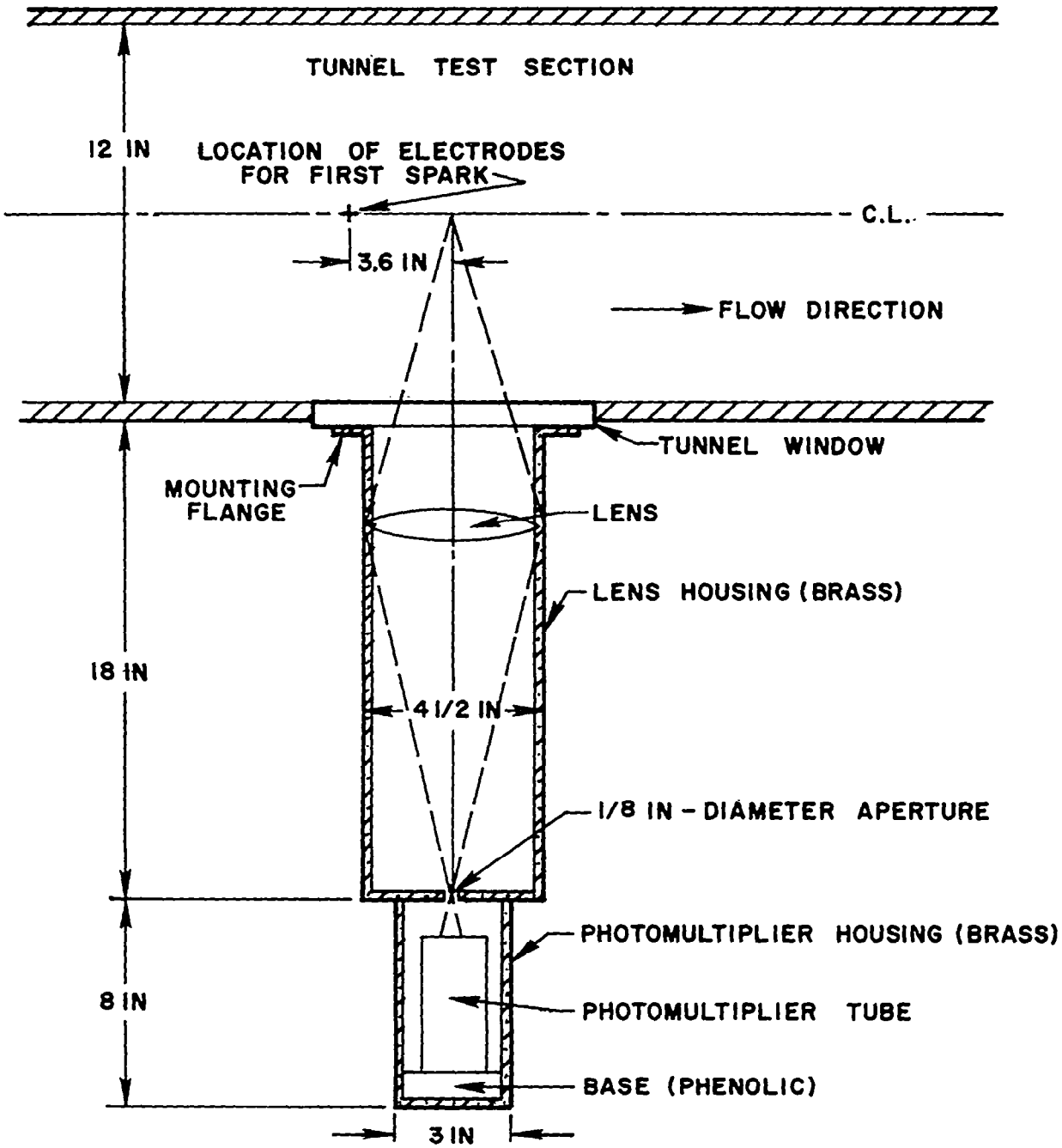

FIG. 39. SECTIONAL VIEW OF PHOTOMULTIPLIER ASSEMBLY.

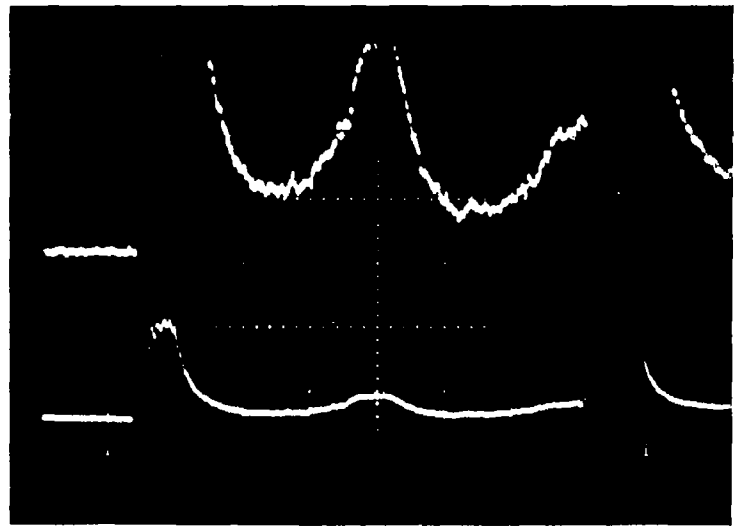

FIG. 40. SPARK-INTENSITY PROFILE OBTAINED WITH PHOTOMULTIPLIER ASSEMBLY.

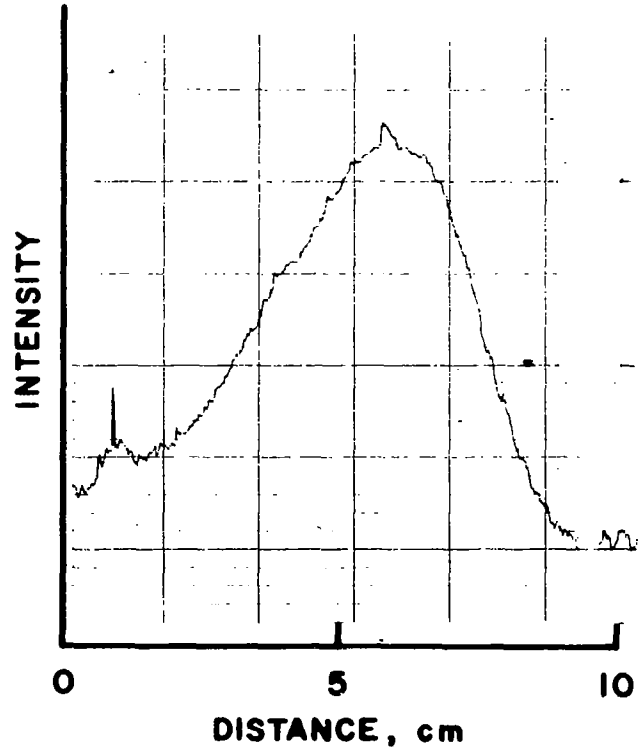

FIG. 41. SPARK-INTENSITY PROFILE OBTAINED FROM PHOTOGRAPH.